INTERNATIONAL IBERIAN
NANOTECHNOLOGY
LABORATORY

44

Development of a microfluidic device for the isolation of tumour-derived extracellular vesicles

José Luís de Faria e Silva Matos Paiva

UMinho | 2022

Universidade do Minho
Escola de Ciências

José Luís de Faria e Silva Matos Paiva

Development of a microfluidic device for the isolation of tumour-derived extracellular vesicles

October 2022

Universidade do Minho
Escola de Ciências

José Luís de Faria e Silva Matos Paiva

Development of a microfluidic device for the isolation of tumour-derived extracellular vesicles

Master Thesis
Master in Biophysics and Bionanosystems

Work developed under the supervision of
Dr. Carlos Honrado and
Prof. Dr. Andreia Ferreira Castro Gomes

October 2022

DIREITOS DE AUTOR E CONDIÇÕES DE UTILIZAÇÃO DO TRABALHO POR TERCEIROS

Acknowledgments

Firstly, I am very thankful to Dr. Sara Abalde-Cela, from the International Iberian Nanotechnology Laboratory, for accepting me to do this innovative project. Secondly, I would like to thank Dr. Lorena Diéguez for introducing me to the INL, as well as the Medical Devices team, and supervising my work, while Dr. Sara Abalde-Cela was not physically present during the first months. Even though Dr. Lorena was not part of my supervisors, she played an important role during my stay at INL. I am as well grateful to have Dr. Carlos Honrado as my new supervisor since Dr. Sara was absent from INL. I learned a lot from him at every step throughout my time doing my thesis and always had his back in every experiment.

I am also thankful to have a team that promotes a healthy environment and helped me when I struggled during my laboratory work. Each member had a remarkable role in my life at INL. In emphasis, the Ph.D. student Cláudia Lopes helped me the most, teaching me every big and small detail and orientating me to do my work, which I appreciate a lot. My colleague Rodrigo Marinho, who did his thesis alongside me, was also helpful, and that made me realize how important teamwork is. Another co-worker I'm happy to have met is Patrícia Rodrigues for helping me with some work I made some mistakes and for giving me alternative guidance for some protocols.

I would like to express my gratitude to my other supervisor, Dr. Andreia Gomes who was also my teacher during the first year of my master's degree and in my bachelor's degree, for every guidance. I gained important knowledge and tools to work in this field.

I would like to express that it was also a blessing for having family and friends supporting my thesis work. Thank you Mário Fernandes for helping me understand and overcome some obstacles I had in my thesis. Thank you. Thank you Inês Araújo and Isabel Ferreira for cheering me up in times I most needed it.

This work happened thanks to the collaboration between INL and UMinho. Both institutions gave me the experience I admire to pursue a scientific professional life.

Statement of Integrity

I hereby declare having conducted this academic work with integrity. I confirm that I have not used plagiarism or any form of undue use of information or falsification of results along the process leading to its elaboration.

I further declare that I have fully acknowledged the Code of Ethical Conduct of the University of Minho.

Desenvolvimento de um dispositivo microfluídico para o isolamento de vesículas extracelulares derivadas de tumores

Resumo

Cancro da mama tem sido uma condição recorrente que afecta, sobretudo, a saúde das mulheres globalmente. Mesmo que tecnologia moderna seja capaz de vigiar estes pacientes e tratá-los, reduzindo a taxa de mortalidade, há ainda um atraso no diagnóstico precoce, resultando num aumento da mortalidade geral induzida por metástases. Compreender esta patofisiologia a nível molecular tem sido útil para obter conhecimento sobre a proliferação do cancro, incluindo reincidências. Vesículas extracelulares (VEs) têm sido utilizadas para novas estratégias de deteção de biomarcadores. VEs são secretadas por células e estão presentes no sangue. Estas possuem bicamadas lipídicas contendo no seu interior proteínas, ADNs, ARNs e lípidos bioativos. VEs formam uma grande variedade de mensageiros intracelulares para a comunicação entre vários tipos de células, transportando indicadores de saúde e doença. Entender a diversa composição de VEs tumorais requer ainda investigação de forma a encontrar potenciais biomarcadores clinicamente relevantes. Um dos maiores obstáculos no estudo de VEs é o seu isolamento. Técnicas comuns dependem, em geral, de estratégias de ultra-centrifugação, que costumam consumir muito tempo e inerentemente obtêm baixos rendimentos. Recentemente, o reagente ExoGAG foi introduzido como um método alternativo para executar o enriquecimento de VEs, permitindo o seu isolamento de biópsias líquidas e obtendo uma população pura de VEs. Para além disto, dispositivos microfluídicos, que manipulam fluídos a altos rácios de fluxo, têm mostrado resultados promissores no isolamento de VEs com poucas contaminações. Especificamente, micromisturadores poderão ser usados para ampliar a produção de complexos VE-ExoGAG, num microssistema, aumentando a eficácia da coleção de VEs. Este projecto pretende desenvolver um sistema microfluídico capaz de misturar VEs com ExoGAG, com o âmbito em obter uma amostra pura para o diagnóstico do cancro da mama. O micromisturador “espinha de peixe escalonada” obteve os melhores resultados de misturação. Técnicas de caracterização mostraram níveis significativos da conjugação, porém a obtenção de populações monodispersas coesas mostrou-se uma tarefa difícil.

Palavras-chaves: Diagnóstico clínico, Cancro da mama, Vesículas extracelulares, Microfluídica, ExoGAG

Development of a microfluidic device for the isolation of tumour-derived extracellular vesicles

Abstract

Breast Cancer has been a recurring condition that affects, especially, the health of many women worldwide. Even though modern technology has been able to monitor these patients and apply treatment, reducing the mortality rate, early diagnosis still lags, resulting in an overall cause of morbidity induced by cancer metastasis. Understanding this pathophysiology, at a molecular level, has been promising to grant knowledge about breast cancer proliferation, including relapses. Extracellular vesicles (EVs) have been used for new biomarker detection strategies. EVs are secreted from cells and can be found in blood circulation. They possess lipid bilayers containing in their interior proteins, DNAs, RNAs, and bioactive lipids. EVs form a vast array of intracellular messengers that are used for communication between a variety of cell types, carrying signals of both health and disease. Understanding the diversity of the composition of tumour EVs requires further investigation to unveil their potential as clinically relevant biomarkers. One of the biggest challenges for the study of EVs has been their isolation. Current techniques mostly rely on ultracentrifugation strategies, which are generally time-consuming and also inherently provide a low yield. Recently, the ExoGAG reagent has been introduced as an alternative method to streamline EV enrichment allowing their isolation from liquid biopsies, and obtaining a purified EV population. Moreover, microfluidic devices, which manipulate fluids at high flow rates, have recently shown promising EV isolation results with low contaminations. Specifically, micromixers can be used to enhance the generation of EV-ExoGAG complexes, in a microsystem, increasing the efficiency of EV collection. This project aims to develop a microfluidic device capable of mixing EVs with ExoGAG to obtain a purified sample for breast cancer diagnosis. A staggered herringbone mixer has shown to be the most optimal for mixing efficiency. Characterization analysis showed a significant conjugation of ExoGAG with EVs, although cohesive monodispersed populations were difficult to obtain

Keywords: Clinical Diagnosis, Breast Cancer, ExoGAG, Extracellular Vesicles, Microfluidics

Index of Contents

Acronyms and Abbreviations

AB – Apoptotic Body

ANXA2 – Annexin A2

AMI – Absolute Mixing Index

BC – Breast Cancer

CAD – Computer-aided design

CD9 – Protein coding gene 9

CD63 – Protein coding gene 63

CD81 – Protein coding gene 81

Dh – Hydraulic diameter

DLS – Dynamic Light Scattering

DLW – Direct Laser Writing

DMB – Dimethylmethylene blue

DUC – Differential ultracentrifugation

EC – Endothelial cell

ELISA – Enzyme-Linked Immunosorbent Assay

ESCRT – Endosomal Sorting Complex Required for Transport

EtOH – Ethanol

EU – European Union

EV – Extracellular vesicle

FBS – Fetal bovine serum

GAG – Glycosaminoglycan

ILV – Intraluminal vesicle

INL – International Iberian Nanotechnology Laboratory

L1CAM – L1 cell adhesion molecule

LOC – Lab-on-a-chip

MD – Microfluidic device

mRNA – RNA messenger

MV – Microvesicle

NTA – Nanoparticle Tracking Analysis

P/S – Penicillin streptomycin

PBS – Phosphate-buffered saline

PDA – Polydopamine

PDMS – Polydimethylsiloxane

Re – Reynolds' Number

RIE – Reactive Ion Etching

RMI – Relative Mixing Index

SAR – Split-and-recombination

SEM – Scanning Electron Microscopy

SHM – Staggered Herringbone micromixer

Si – Silicon

Si-OH – Silanol group

SMAD – Suppressor of Mothers Against Decapentaplegic

TEM – Transmission Electron Microscopy

TEV – Tumour-derived vesicle

TRPC-5 – Intercellular transfer of transient receptor potential channel 5

µL/min – Microlitter per minute

List of Tables

List of Images

Table of equations

1 - Introduction

1.1 – Breast Cancer

Breast cancer (BC) is one of the most well-known malignant conditions, and one of the most notorious cancers worldwide [1–4]. In recent years, statistical data from the European Union (EU) shows BC as the most common type of cancer diagnosed, as well as the leading cause of death from cancer in female patients. Despite the mortality rate decreasing over time, due to effective treatment and tools for detecting the disease at early stages, the incidence rate has been higher than before[1,5].

BC is a heterogeneous disease that originates from the presence or absence of the estrogen receptor (ER) and progesterone receptor (PR), and the expression and amplification of the human epidermal growth factor receptor type two (HER2), giving a wide range of different malignant phenotypes. Not only that, BC is defined by a wide window of relapse, that can span between months and decades after surgery, which might be due to the molecular heterogeneity [6,7]. Metastatic relapse is induced by the outgrowth of cancer cells that have escaped from the primary tumour and migrated into the blood and lymphatic vessels. Then, cancer cells migrate to distant sites and proliferate, developing a systemic disease. While patients diagnosed with BC have options for treatment, for example, surgery, chemotherapy, and radiation, patients that suffer from metastatic relapses, unfortunately, have no curative therapy, meaning that the recurrence of BC is the cause of most mortality cases, which can be related to the lack of data for detecting relapses[6,7].

In 2020, the incidence of BC diagnosed in the EU (**Figure 1.1**) was estimated to be 13.3%, making it the most frequent type of cancer. One out of seven women has a lifetime risk of developing breast cancer [1]. It has been estimated that BC can occur in three-quarters of individuals aged over 50 years, with an incidence of less than 5% in people below 35 years old[5]. In Portugal, the mortality rate has shown a heterogeneous result, noting an increase in the southern part of the country and a decrease in the northern region. Despite having, in general, a decreased mortality rate, it is still impactful on the Portuguese population yearly, especially in patients who are over 65 years old[2].

Some risk factors for BC proliferation are unhealthy diet, alcohol consumption, sedentary behavior, age at first pregnancy, breastfeeding practice, and exposure to exogenous hormones including long-term hormone replacement therapy. Possible distinctions in genetic predisposition, age distribution, and actual availability and access to cancer treatment could also be risk-inducing[4,5].

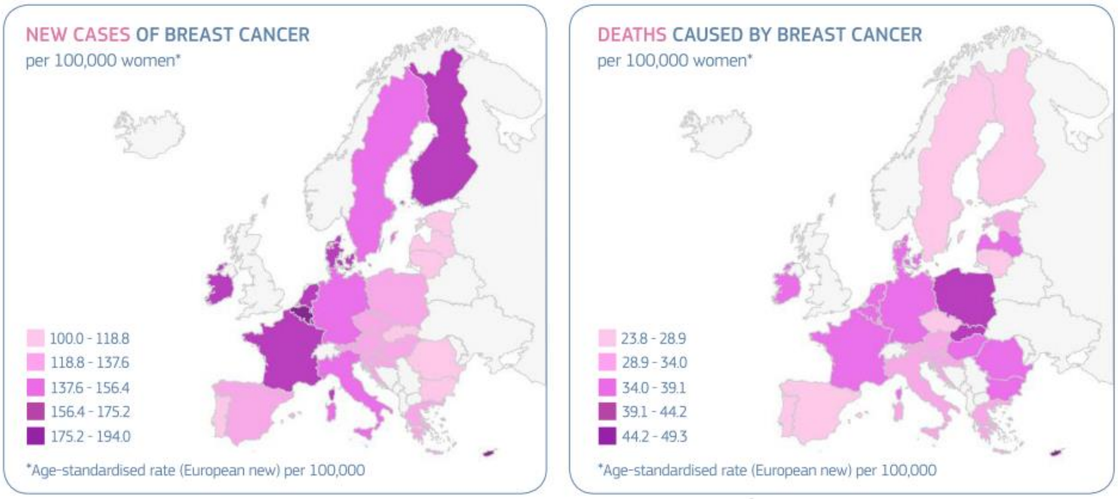

***Figure 1.1** – New cases and death numbers per 100.000 women in the EU in 2020[1].*

In male patients, BC is rare, occurring between 0.5% and 1% of all diagnosed cases worldwide. This can be related to the fact that the male body has less breast tissue and different quantities of hormones, decreasing the chance of cancer proliferation. However, the risk factors already mentioned still stand for male patients. BC in male patients has also the consequence to be confounded with a benign tumor since its detection is delayed and it is only noticed when it reaches an advanced stage[8].

Anatomically, the breasts sit atop the pectoralis muscle, which is above the ribcage (**Figure 1.2**). The breast tissue extends horizontally from the edge of the bone sternum out to the underarm. A tail of breast tissue called the "axillary tail of Spence" extends into the underarm area. This is important because breast cancer can develop in this axillary tail, even though it might not seem to be located within the actual breast. Most cancers of the breast arise from the cells which form the lobules and terminal ducts. These lobules and ducts are spread throughout the background fibrous tissue and adipose tissue that make up the majority of the breast[9,10]. The breast tissue is encircled by a thin layer of connective tissue called fascia. In this tissue, the blood flows giving nutrients, oxygen, and more fat tissue. The lymphatic system also flows in the fascia through lymphatic nodes. It is through these lymphatic vessels that breast cancers metastasize or spread to the lymphatic system[3,9,10].

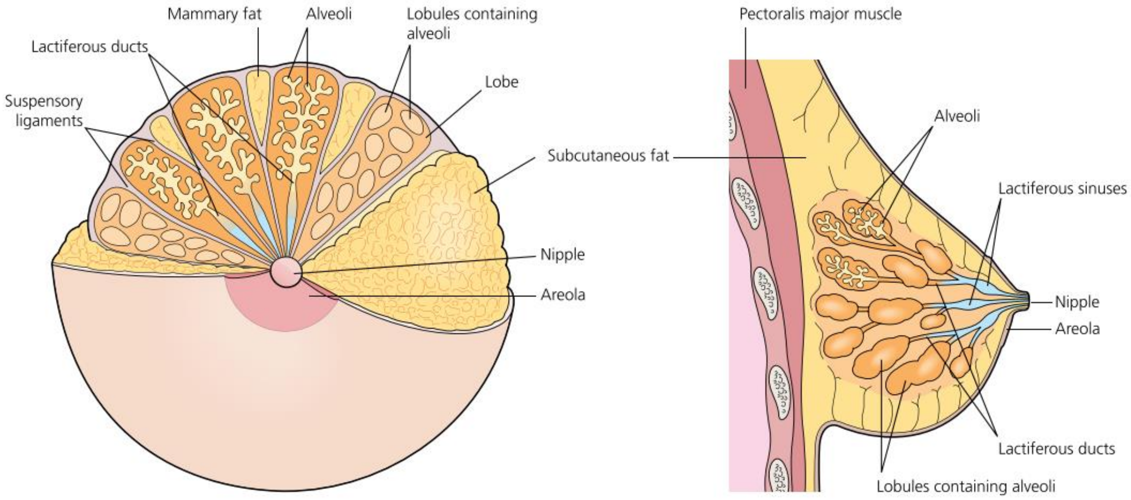

Figure 1.2 *– Frontal and peripheral view of a healthy breast region showing its structures and connections with circulatory and lymphatic systems*[9]

For therapy, early detection and monitoring of patients have been key factors, with bioimaging techniques and symptoms, such as pain or palpable mass, being some examples. Mammography has been the most important diagnostic tool for BC detection by discovering tiny, non-palpable lesions[3,11]. This technique is effective in breast tissue that is not dense, due to its high sensitivity and specificity, is inexpensive, and well-tolerated, and has helped reduce breast cancer mortality. However, limitations while using this technique must also be considered, such as are relatively high rate of false positives, wrong results due to pain and anxiety, false alarms, and associated radiation risks[3,4,11]. Ultrasounds are required for the management and diagnosis of breast pathology. This technique has been used as a supportive tool alongside mammography for certain high-risk groups, in particular women with dense breasts, does not use ionizing radiation, and is defined with high sensitivity [4,11]. However, ultrasounds also have a significant amount of false-positives results. Magnetic resonance imaging (MRI) is another tool used for screening higher-risk individuals due to its higher sensitivity but holds a lower specificity and higher cost compared to mammography. This technique provides important information regarding the stage of breast cancer, evaluation of microcalcifications, premalignant lesions, and residual tumours inside operated patients, making it also suitable during the treatment of a patient with BC[3,4,11]. Since MRI is a very expensive technique, there is a limit to its availability in all hospitals and clinics, especially in developing countries. Moreover, the diagnostic tools can also have a hard time distinguishing metastatic nodes from regular lumps. Thus, understanding the tumor's molecular heterogeneity is crucial in creating a new pathway for treatments that can show more concrete results, since a delayed diagnosis after recall may cause the tumour to be discovered in a more advanced stage[7,12,13].

Diagnosis through the usage of biomarkers for signaling vital processes can be promising. Biomarkers can provide a better understanding of cellular and molecular pathways involved in BC pathogenesis[4,11]. An example of biomarkers is carcinogens, which are any organic substances that are chemically toxic to the breast's functionality and structure [4,10,14]. Biomarkers are biological molecules produced by the body or tumors in a person with cancer that signal pathophysiological alterations[14]. Proteins (e.g. Her2, ER, and Ki67), mRNAs (e.g. ERα, ERβ, and ERRγ), enzymes (e.g. CEA and TSGF), and microRNAs (e.g. miR-21, miR-10b, miR-155, and miR-145) are potential biomarkers for BC diagnosis in patients. These biomarkers can also be found in extracellular vesicles, such as exosomes[9,10,12].

1.2 – Extracellular Vesicles

Extracellular vesicles (EVs) vary between 30 nm up to 5 micrometers and are lipid bilayer-enclosed biomolecular particles that are secreted from cells, being genetic information carriers for cell-to-cell communication and inducing cellular responses towards their microenvironment (**Figure 1.3**). They can be found in every corner of the human body, mainly in biofluid environments, such as blood, urine, amniotic fluid, cerebrospinal fluid, saliva, breastmilk, and even nasal secretions[15–24]. EVs generally carry a slightly negative surface charge as demonstrated by zeta-potential estimations[23]. EVs are identified biochemically due to the presence of specific proteins within their membrane, namely CD9, CD63, and CD81. Nucleic acids have also been found in extracellular vesicles, mainly mRNAs, miRNAs, and ribosomal RNA[17,18,23].

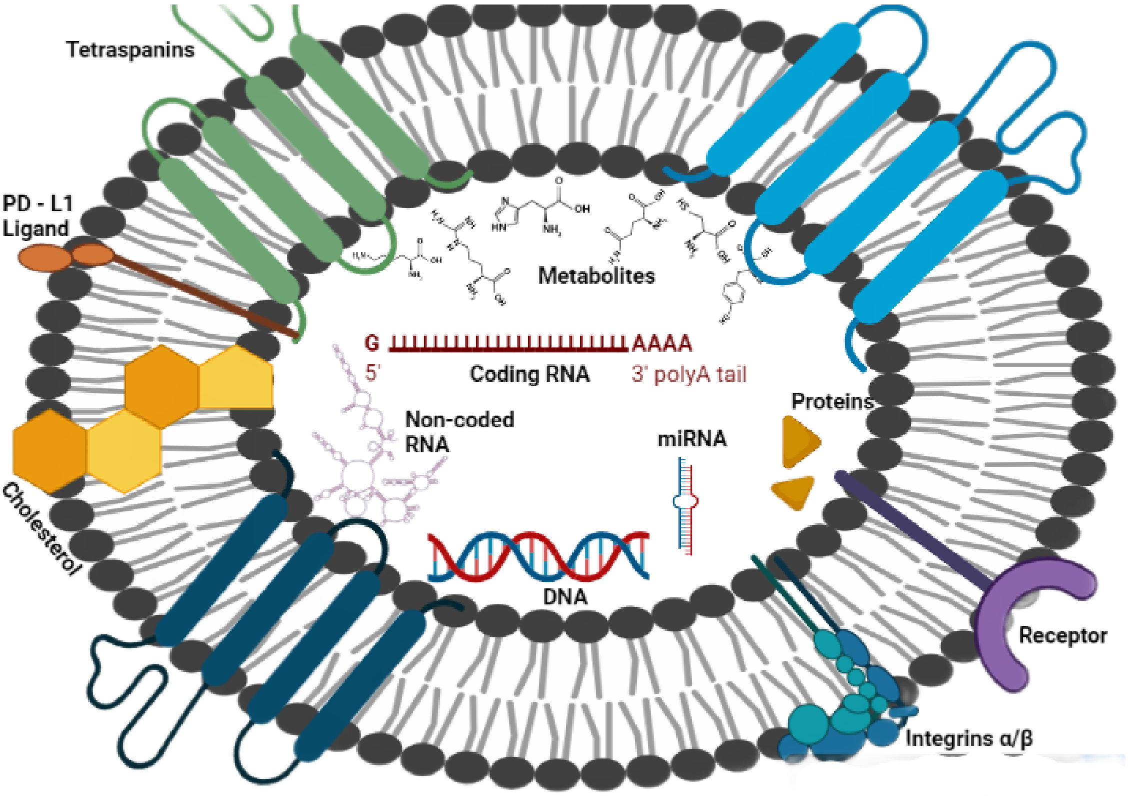

Figure 1.3 – *Common composition of EVs*[23,25]

1.2.1 – Types of EVs

EVs have been subclassified based on their biogenesis and characterestics such as structural form, chemical composition, size, genetic information, and function, being broadly categorized as exosomes, ectosomes, microvesicles, and apoptotic bodies (**Table 1.1**)[18,22,23].

Exosomes, also known as intraluminal vesicles (ILVs), are enclosed within one single outer membrane and are secreted by cells located in any type of biofluid. They are formed at the end of the endosomal course through the membrane of endocytic cisternae by inward budding of microdomains and measure between 30–150 nm in diameter. The accumulation of ILVs ends up forming multivesicular vesicles (MVVs) and later are moved to the membrane. Their protein content is made of ESCRT proteins alongside Alix, TSG101, HSC70, flotillin, and HSP90β, transmembrane proteins such as CD63, CD9, and CD81, and a high content of glycoproteins. ESCRT mechanism is responsible for the enriched lipidic content in exosomes[22,26] Due to their complex structure and potential diverse functions from different cell types, they demonstrate a smaller version of their parental cells, which are responsible for bioactivities that induce biological processes in neighboring cells[26].

Microvesicles (MVs) are heterogeneous populations of membrane vesicles that form by direct outward budding of the cell's membrane. MVs vary from 100 nm up to 1 µm in diameter with variable shapes. Their biogenesis requires cytoskeleton components, such as actin, microtubules, kinesin, myosin, and fusion machinery (SNAREs and tethering factors). They are usually products of platelets, endothelial cells (ECs), and red blood cells[22,26]. The contraction caused by actin-myosin machinery and the phosphatidylserine (PA) translocation, from the inner to the outer leaflet, induce the redistribution of phospholipids and fission of the cell membrane. These MVs are specifically loaded with ARF6, MHC-I, b1-integrin, VAMP3, and MT1MMP. External factors can also release MVs from the cells, such as the influx of calcium, and hypoxia[27].

Ectosomes are generated at the plasma membrane at a faster pace compared to exosomes. The assembly of its cargoes, composed of proteins and nucleic acids, starts at the cytosolic face. Next, differentiated membrane microdomains are induced by outward budding and instantly released by a fission mechanism, to the extracellular space. This release might be due to asymmetric membrane phospholipid layers induced by calcium-dependent enzymes, flippases, floppase, or ESCRT complexes. Their diameter is between 100–500 nm. Ectosome membranes have high levels of cholesterol, sphingomyelin, and ceramide[28].

Apoptotic bodies (ABs) are hallmarks of apoptosis, originating from dying cells. They can be 50 nm up to 5 µm in diameter. These bodies are due to the separation between the plasma of the cell's membrane and cytoskeleton, alongside an increased hydrostatic pressure during the contraction of the cell. The larger apoptotic bodies are known to contain intact organelles, chromatin, and glycosylated proteins. Lipids, RNA, and DNA molecules are also components of these ABs[22,24].

__Table 1.1__ – Characteristics of four types of extracellular vesicles[18,22–24,26–29]

EVs features	Exosomes	Ectosomes	Microvesicles	Apoptotic Bodies
Size	30-150nm	100–500nm	100nm-1µm	50nm-5µm
Origin	ILVs accumulated into MVBs	Plasma membrane with cellular content	Plasma membrane with cellular content	Plasma membrane with cellular content
Mechanism of formation	MVBs fused with the cell membrane	Membrane Fission	Outward budding	Cell fragmentation
Release	Cellular activation	Cellular activation or external factors	Cellular activation or external factors	Apoptosis
Time of release	Minutes or more	Few seconds	Few seconds	Seconds, minutes, and more
Pathways	ESCRT dependent Ceramide dependent	Ca2+ dependent flippases, and floppase; ESCRT complexes	Ca2+ dependent Stimuli and cell-dependent	Apoptosis process
Content	Proteins, mRNA, miRNA, lipids	Proteins, mRNA, miRNA, lipids	Proteins, mRNA, miRNA, lipids	Cell organelles, proteins, nuclear fractions, DNA, coding, and non-coding RNA, lipids

1.2.2 – Cell-to-cell communication role of EVs

Previously, EVs were thought to be simple vesicles of unwanted components from cells. However, increasing studies on their biogenesis pathways have shown that, in fact, EVs have an important role as a vector for communication between cells[16,17,22,24,26–28]. The proteomic profiles, lipidic content, and genetic material inside EVs have the potential to deliver combinatorial information to multiple cells in their tissue microenvironment[27]. For example, EVs have played a key role in immunoregulatory functions, such as the exchange of antigen information between immune cells and the activation or inactivation of immune cells, as well as, regulating gene expression in various organs due to their mechanism of signaling proteins and reducing signaling activity[21].

Neighboring cells intercept EVs by membrane fusion or via endocytosis. The pathway for EVs to enter a cell determines their functional effects[27]. ABs are usually phagocytosed by macrophages, parenchymal cells, or neoplastic cells and degraded within phagolysosomes. The phosphatidylserine present in the outer leaflet induces a signal that facilitates the recognition and uptake of apoptotic cells by phagocytes[24]. Exosomes and ectosomes can enter other cells by membrane fusion and/or endocytosis because of their tetraspanins, integrins, proteoglycans, and lectins content, depending on the type of cell that originated them. The tetraspanin CD9 was found to be responsible for membrane fusion[28]. Exosomes can also be phagocytized and co-localized with lysosomal biomarkers, such as LAMP-1. Furthermore, the end of the EV uptake makes the beginning of the endocytic pathway where EVs start the fusion with an endocytic membrane[28]. EVs, specifically exosomes and microvesicles, have been shown to transfer horizontally mRNA and miRNA into targeted cells, changing their phenotypes, and blocking their current translation of RNA content[29,30].

1.2.3 – Pathophysiological behaviour of tumour-derived EVs

EVs also provide important intercellular communication signals in pathological behavior (**Figure 1.4**) such as cancer, in other words, EVs are novel mediators of tumorigenesis [19,29–31]. For example, tumour-derived EVs (TEVs) contain molecules associated with angiogenesis, metastasis, and immune escape. Some proteins and RNA sequences can be used as biomarkers to evaluate the status of the cells and tumour progression.

Moreover, the miRNA of TEVs has been studied for being responsible for cancer progression[19]. For example, miR-105 is detected in EVs during BC proliferation, which is associated with metastasis formation while destroying endothelial monolayers. Other miRNAs highly expressed in BC patients in comparison to healthy organisms are miR-21, miR-222, and miR-155. The intercellular transfer of transient receptor potential channel 5 (TRPC5), which contributes to multi-drug chemoresistance efflux transporter p-glycoprotein production, has been highly expressed as well[32].

In addition, TEVs derived from BC can transform the microenvironment by promoting tumorigenesis of normal cells, while inhibiting autophagy in response to DNA damage repair (DDR), through the induction of reactive oxygen species (ROS) in normal breast epithelial cells[15,30,31]. To avoid immune responses, TEVs can control tumour proliferation, by decreasing the expression and release of IL-2, diminishing the synthesis of natural killer cells (NKs). TEVs, in form of microvesicles, have been shown to increase cancer cell invasion and migration through extracellular matrix metalloproteinase-9 activity (MMP-9), which is dependent on phosphorylation of p38 and type 4-chemokine receptor (CXCR4) expression, respectively. This has also changed the metabolic state and cellular signaling of the degraded extracellular environment, in response to normal cells, and induces high levels of stemness-related markers and metastatic-related mRNA[30,33].

Oncogenic proteins and microRNAs have been conditioning apoptosis, cytoskeleton remodeling, cell mobility, cell cycle, tumor invasion, and metastasis[30,33]. Communication between cancer cells has also been studied by using GFP (green fluorescent protein) in CD63 expressed in TEVs. This protein conjugated with CD63 was important as a tracking mechanism to study cell adhesion induced by TEVs. Cell adhesion has crucial consequences based on tumor growth and metastasis through the interaction of tumor endothelial cells[32,33].

TEVs can also induce tumor-associated myofibroblastic phenotype of adipose tissue-derived from mesenchymal stem cells that cause an increased expression of α-Smooth muscle actin (α-SMA). As consequence, stromal cell-derived factor 1 (SDF1) is activated, transforming growth factor β (TGF-β), vascular endothelial growth factor (VEGF), and C-C motif chemokine ligand 5 (CCL5) through SMAD-mediated signaling pathway. Tumoral stromal cells induce Wnt-planar cell polarity that promotes BC invasiveness[30,33,34].

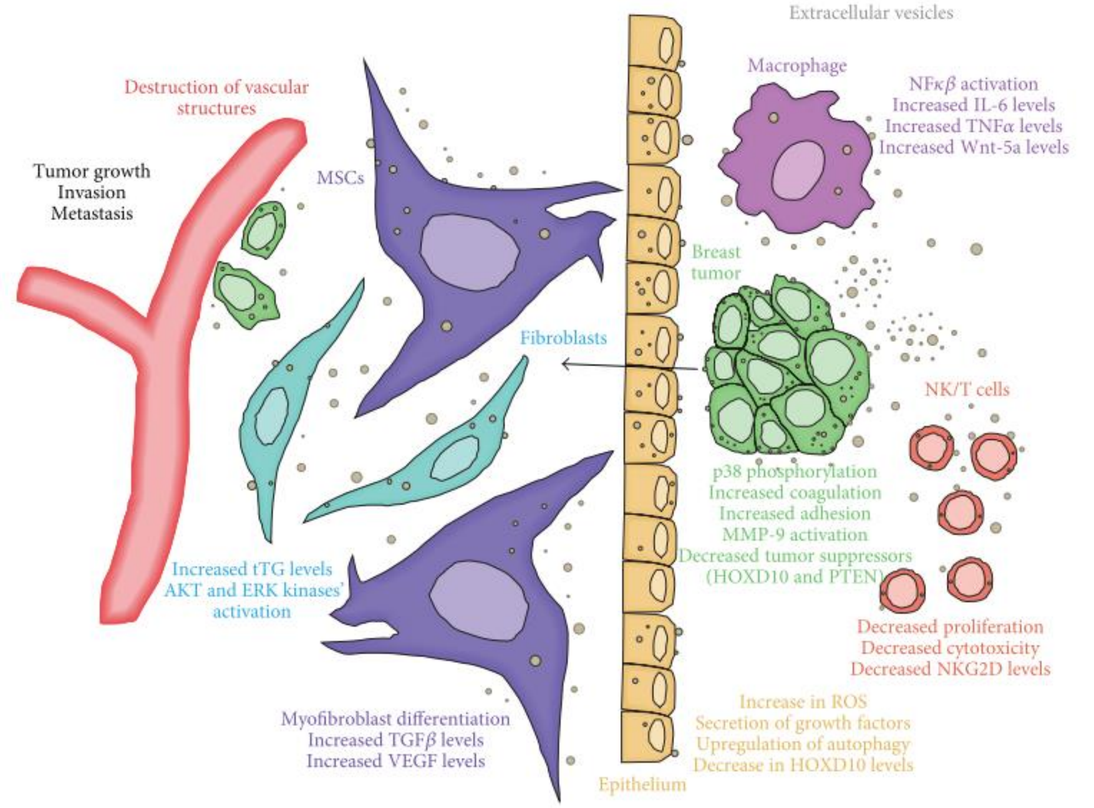

Figure 1.4 – *Interactions between TEVs and stromal, epithelial, and immune cells within the tumor niche in the breast, resulting in changes that enhance cancer growth and metastasis[30].*

1.2.4 – Isolation methods for EVs

EVs have shown intrinsic therapeutic activity when isolated from one specific tissue and transported to another tissue. They can, for example, have cardio-protective and pro-inflammatory properties, and also trigger systemic immune responses[18]. Therefore, not only are EVs potential vectors for clinical usage, but the increase or decrease of TEV biomarkers can provide information about patient status, indicating prognostic potential[28]. However, there are limitations concerning TEV analysis because of technical challenges for the isolation, purification, and quantification of these small vesicles. Moreover, their complex biochemical contents depend on the purity of the sample, especially for techniques with high sensitivity[18,32].

The most well-known isolation methods of EVs for detection and quantification are differential ultracentrifugation, PEG-based precipitation, size exclusion chromatography, immunoaffinity capture, flow cytometry.

Differential ultracentrifugation (DUC) is the most common isolation method for EVs. This technique uses a sequential separation of particles by sedimentation based on size and density and is determined using centrifugal movements with time. This separation can lead to pure populations of exosomes. The extraction capacity to obtain this purity depends on the acceleration of the centrifuge, the rotor factor that represents the relative pelleting efficiency of a rotor at maximum speed, viscosity of the sample, and time[16,22,26,30,35]. The lower the rotor factor gets, the better the pelleting efficiency, and the shorter the centrifugation time. Reduced viscosity helps the efficiency of the sample isolation[35]. Sequential centrifuge steps are performed to remove cells, cellular debris, apoptotic bodies, and other microvesicles at increasing speeds. Next, a supernatant with a high concentration of exosomes is obtained, but there are still contaminated with microvesicles, lipoprotein moieties, and other protein aggregates. The next step is spinning again the sample but at a faster pace and an increased duration of the procedure. After this procedure, the pellet can be resuspended in a phosphate-buffered saline (PBS) and again ultracentrifuged to increase the purity of the sample. DUC has been making homologous populations of exosomes that range between 20–250 nm. Due to technological advancements, this technique has been declining in popularity, since DUC is time-consuming (>10h) and labor-intensive[35,36]. Other limitations are the contamination of the final product with particles that have similar sizes and the price of the equipment. To counter these limitations, an approach to density gradient ultracentrifugation is useful to segregate exosomes based on size, mass, and density[35].

PEG-based precipitation is a technique where the aqueous medium has polyethylene glycol that wraps around exosomes and induces exosomal aggregation. Then, it is possible to precipitate the sample through centrifugation at a low speed. The range of these EVs is similar to those obtained from DUC, although the purity of the sample does not follow the same way because proteins, immunoglobulins, viral particles, immune complexes, and other contaminants are also precipitated into the final pellet. Precipitating exosomes based on biomarkers, such as tetraspanins or miRNA could help to obtain a purer sample, however, this technique doesn’t reach the levels of purity DUC can have but can create higher yield samples. Combining this technique with another is a valid strategy to remove these drawbacks. On the bright side, PEG-based precipitation can easily process many samples simultaneously, faster, and with lower costs without damaging exosomes[16,22,35,37,38].

The immunoaffinity capture method depends on the separation of specific exosomes based on the expression of surface proteins. This technique uses antibodies against biomarkers present in EVs, such as tetraspanins. The isolation is made by incubating the sample with magnetic beads or gold-loaded ferric oxide nanocubes, filled with antibodies. Other biomarkers that can be used are chondroitin sulfate peptidoglycan 4 and exosome-binding molecules such as heat shock protein or heparin. This technique is usually used as a support mechanism for DUC to obtain higher purity in the sample. The downside of Immunoaffinity capture is the selection of antibodies available, as exosomal content and markers vary with exosome origin and status. Antibodies may also not reach certain biomarkers due to not being on the surface of the exosomes. The antibodies can also damage the integrity of exosomes. This technique is more effective with a low yield sample[16,22,32,35].

Flow cytometry plays a promising role in obtaining a good analysis of clinical samples based on their physical and chemical characteristics. However, this technique is limited in the detectable size, as particles with less than 300 nm in diameter present weak light scattering[31,39]. In other words, this technique excels with other characterization methods, such as dynamic light scattering (DLS) and nanoparticle tracking analysis (NTA) to ensure more accurate particle counts, although molecular information inside EVs is still limited, which means, that previous knowledge of proteomic composition is required[22,31,39]. Despite being difficult to target a very specific sub-population of EVs based on internal molecular content, these vesicles have a wide variety of biomarkers on the surface. Fortunately, this technique can be useful for example, by using CD63-tagged magnetic beads to quantify a purified homologous population of exosomes, enhancing the specificity of EVs[36]. Obtaining a single particle suspension can be challenging when the exosomal concentration is high, or when aggregation of vesicles happens at the same time as the isolation process. Thus, the immobilization of exosomes on the surface of beads to be observed and analyzed is often required[23]. However, detecting microvesicles have an easier outcome due to their bigger sizes. Modern flow cytometers can have many lasers and fluorescence detectors, granting an optimal way to put multiple conjugated antibodies in the same sample to label these microvesicles[29].

1.2.5 – Analysis and characterization methods of EVs

Characterization methods used to optimize EVs the same way to optimize TEVs are Nanoparticle tracking analysis (NTA), Dynamic Light Scattering (DLS), Electron Microscopy, and Enzyme-Linked Immunosorbent Assay (ELISA).

Nanoparticle tracking analysis allows the determination of the size distribution and particle concentration of EVs based on the Brownian motion of these nano-sized particles, using the Stokes-Einstein equation to estimate their sizes. The laser is scattered as light interacts with the sample, and then collected by a microscope with a camera on top capturing the movement of particles in a video[16,22,37,40]. An NTA software will use that video to estimate the sizes of EVs. This method can determine particle size between 10 and 1000 nm in diameter which is suitable to analyze exosomes. The main challenge is that NTA requires sample volumes of, approximately, 0.5 mL and optimization of data collection and analysis parameters. Using the highest camera settings will impede the analysis of scattered light from EVs due to increased noise, meaning this measurement is highly sensitive[22,40].

Similar to NTA, dynamic light scattering also uses the same method by analyzing the Brownian motion of EVs obtaining the diffusion coefficient to apply the Stokes-Einstein equation. However, DLS uses fluctuations in the intensity of the scattered light to estimate the particle’s size [22,41]. This technique requires very little sample volume and is much easier to utilize. On the other hand, DLS has a harder time analyzing heterogeneous populations. The fluctuations in the intensity are also weaker to determine EVs with smaller sizes making them hard to be detected. DLS also provides no biochemical information resulting in no knowledge about the type of cells that originated the EVs of a determined sample[22,29,34,41].

Electron Microscopy, mainly transmission electron microscopy (TEM) and scanning electron microscopy (SEM), is used to evaluate the surface (morphology and topography) of the extracellular vesicles. Both SEM and TEM produce high-resolution images using a beam of electrons. TEM has been the most prevalent technique to confirm the presence of EVs because the electrons emitted can make images with possibly subnanometer resolution. Since EVs are negatively charged on the surface, soluble proteins and/or salts are needed to be removed. The sample is fixed with paraformaldehyde because TEM is performed in a vacuum[22,42]. A droplet of contrast agents is used under a grid after the fixation of the sample. A filter paper is used to remove the excess contrast agent, while the grid gets dried. Then, the grid is placed in a vacuum chamber and exposed to an electron beam while images are being made. TEM may damage EVs if these vesicles have water as their cargo. The contrast of TEM images is often inefficient to distinguish EVs from non-EV particles with identical sizes. Moreover, TEM is highly influenced by any operator bias during particle identification, which means that TEM is less relevant as a technique for the identification of TEVs [42]. In SEM, a focused beam of electrons scans the surface of a sample interacting with all the atoms available. Detection of the secondary electrons, that came from the outer layers, enables the visualization of the topography. Backscattered electrons, originating from the deeper layers, are associated with the atomic number of the atoms in the sample. SEM can be used to visualize the topography of TEVs with sizes of 50nm. However, SEM also has a hard time segregating EVs from non-EV particles with similar morphology[42].

Enzyme-Linked Immunosorbent Assay (ELISA) is a detection method based on an antibody against an antigen of interest on the surface of a microplate. The immobilized antibodies will interact with the antigens of EVs, immobilizing them, and a calibration curve can then be created to quantify EV capture. Preferentially, this method works better with exosomes and can provide information that can distinguish EVs from TEVs in a sample. However, ELISA requires samples with high purity and creates biased results due to contaminating biomolecules present co-isolated with exosomes[16,38,39].

1.3 – Microfluidic devices and EVs

Microfluidic devices (MDs) (**Figure 1.5**) have emerged as low-cost and promising tools for biological studies, gaining interest in the scientific community in recent years. These devices aim to isolate exosomes based on several parameters including immunoaffinity, size, and density[35,43]. MDs revolve around the flow of liquids, for example, serum or plasma, within small, micro-sized channels that can segregate and purify samples, capturing and then separating EVs by different methods[41]. MDs tend to be efficient and fast in processing, with a high level of purity in the exosomal pellet, although are highly complex and expensive machinery (**Table 1.2**). MDs can handle smaller sample volumes, such as 10 µL, to isolate exosomes, therefore, the cost, processing time, and consumption of reagents are reduced. However, MDs share the same limitations as the immunoaffinity method. MDs give a promising new pathway to analyze EVs and TEVs, even though they still need to be standardized as a common method[35]. EVs isolated using microfluidic devices can maintain their morphology although there are traces they can be damaged due to shear stress[44].

Through the immuno-microfluidic technique, exosomes are separated by the specific binding of antibodies immobilized on the microfluidic devices. These can be defined as chips that function as exosomal biomarkers. Using, for example, the herringbone groove to create anisotropic flow as the fluid travels through the device, it is possible to establish interactions between EVs and the antibody-coated surface of the MDs, inducing the binding of TEVs into the chip. A staggered herringbone mixer(SHM) is an examplthat uses a polydimethylsiloxane (PDMS) and comprises two different layers that are thermally bonded[43–45]. Another example is the ExoChip, which uses CD63 antibody, gold electrodes that use CD9 antibody, graphene oxide/polydopamine (Go/PDA) nanointerface with CD81 antibody, and SHM groove with CD9 antibody[35]. With thorough knowledge of the molecular and genetic content of TEVs, it is possible to identify tumor-specific antigens present on the EV surface, enabling antigen-specific capture of these tumor vesicles in MDs[44].

MDs can also filter and trap EVs with porous structures, removing cells and cell debris and allowing the passage of EVs or TEVs for isolation and diagnosis[45]. Pressure-driven filtration uses a syringe pump with filter membranes containing 500 nm pores to avoid agglomerations. Another example is electrophoresis-driven filtration, which induces negatively-charged phospholipid membranes of EVs to pass the filter membrane, avoiding proteins and other molecules due to having different charges[43–45].

Microfluidics devices with ciliated micropillars have also been used to purify EVs without contamination. EVs are trapped in nanowires whereas other components with larger sizes continue in the flow. Quantum dots (QD) are used directly to visualize the trapped EVs on micropillars, while PBS is used to release the EVs, dissolving them[44].

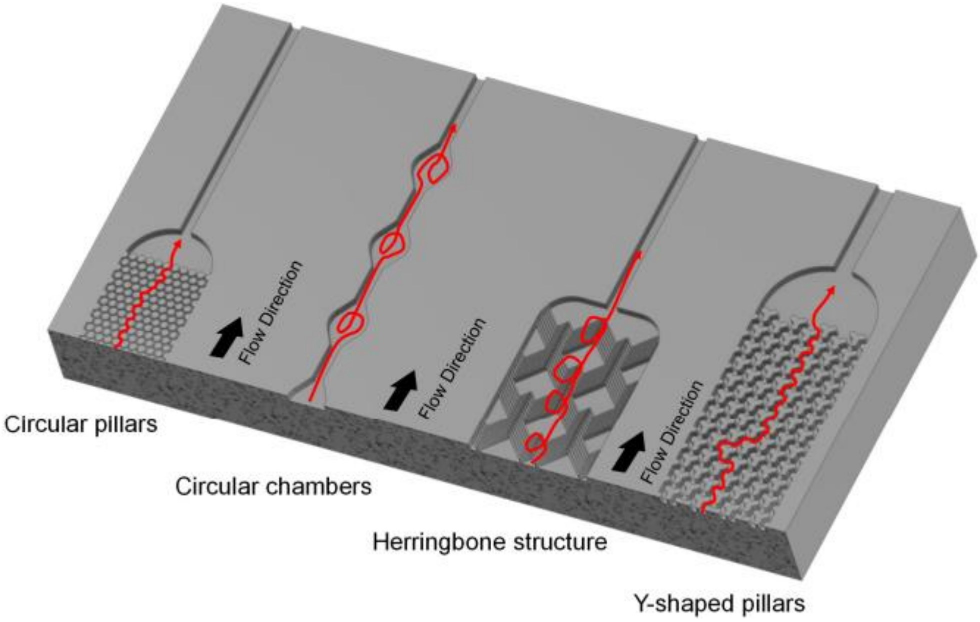

Figure 1.5 – Comparison of four different design concepts to enhance the performance of microfluidic affinity separation. Designs were made through Autodesk Inventor Professional The red arrows indicate the flow direction. Each structure induces different hydrodynamic mixing patterns[46]

Table 1.2 *– Features of microfluidic devices when compared with conventional methods (such as DUC)*[43,47]

	Advantages	Limitations
Microfluidic methods	Small device footprint Low risk of contamination Small samples are useful Easy integration for multiple protocols Easily disposable Rapid and easy fluid manipulation Real-time process monitoring Flexible in changing the methods according to the protocol needs Low chance of shear force on EVs	Complex machinery to manufacture Requires multiple components such as pump, valve, tubing, and connectors for operation Standardization and industrialization Sensitive to operational conditions Difficult for mass production

1.4 – ExoGAG reagent

ExoGAG is a prominent candidate for the clinical analysis of breast cancer. This technology is a patented extracellular vesicle purification method[48] and is based on the ability of a cationic organic dye (dimethylmethylene blue) to bond with glycosaminoglycans (GAGs), which have negative charges in linear polysaccharides, that are present in EV membranes. The neutralization of the cationic agent when bonded with the GAGs thus induces the formation of aggregations in a complex. This complex can then be purified by standard centrifugation[49]. ExoGAG can be used in three simple steps. The first step is mixing the sample and ExoGAG precipitation reagent and then incubating for 5 min at 4°C. Secondly, centrifuging the sample at 16000g, 15 min, and 4°C. Lastly, removing the supernatant and resuspending the EVs in the appropriate buffer depends on the next specific method[49].

ExoGAG has shown good and reproducible results in the purification of EVs, enhancing studies on the biomarkers present in a sample. Some of these biomarkers of interest are L1CAM and ANXA2, which have significant clinical importance, providing breast cancer diagnostic and prognostic value[49,50]. ExoGAG technology can thus separate EVs from conditioned culture media of representative endothelial cancer cells and the more complex plasma samples. High-purity EVs with minimal protein contaminants are obtained with simple protocols. Compared with differential ultracentrifugation and other precipitation methods, ExoGAG has managed to meet the requirements of specificity and sensibility in EVs purification, which is essential for further characterization methods mentioned earlier.

1.5 – Liquid biopsy

As ExoGAG enhances and facilitates the analysis of biomarkers in TEVs, it is expected for this technology to be translated into liquid biopsies for clinical analysis. Liquid biopsies (LB) are minimally invasive diagnostic techniques that allow the detection of tumor material from a body fluid sample, enhancing the comprehension of TEVs biogenesis and the histological proliferation of tumours in BC[49,50]. This procedure is based on using only samples of body fluids, instead of cell tissues. The outcomes of using LB are improved results in cancer analysis compared to other procedures due to its enhanced sensitivity in diagnosis and ease of repeated sampling throughout treatment in a much more convenient and non-invasive way.[51,52]

Selecting L1CAM and ANXA2 for prognostic of endometrial cancer and predictive value, the ExoGAG protocol managed to obtain purified samples of EVs with significant concentrations, presenting that L1CAM expression did not differ between cancer and normal patients. However, ANXA2 has been highly expressed in cancer patients, which correlates that the EV-based biomarker strategy can improve the specificity and sensibility of this biomarker in the prediction. Not only that, ANXA2 has played a role in angiogenesis and metastasis in breast cancer and can be a therapeutic target[49,53].

Apart from membrane biomarkers, exosomal cargo like DNA and RNA can be useful for therapy monitoring in the early stages of cancer. Molecular characterization of RNA present in TEVs has shown solid information to be associated with decreased survival time in metastatic BC[52]. Understanding the genomics of nucleic acid present in EVs and TEVs can enhance therapeutic clinical trials with more precise results, and are more reliable and stable than cfDNA due to protection by the lipid bilayer of EVs/TEVs[54,55]

2 – Road to microfluidics: An overview in engineering and health fields

2.1 – Fabrication of microfluidic systems to process complex samples

The fabrication mechanism for microfluidic devices started in the early 90s with the concept of developing microchannels that allowed precise control of fluid flow at the microscale. This advancement required knowledge in the fields of chemistry, physics, biology, mechanic, and electronic engineering[56,57]. With this idea, it is possible to recreate processes and assays, such as reactions, separations, or the detection of various compounds[56], while requiring only small amounts of samples and reagents, which is cost-saving and reduces the amount of waste produced[57]. Depending on their purposes for specific research, these instruments are adaptable to be microreactors, lab-on-a-chip (LOC), and organ-on-a-ship[56,58,59]. Unique phenomena emerge in capillary microfluidics because of shorter retention times, laminar flows enhanced heat and mass transfer, and large surface-to-volume ratios. The wetting and contact angles are also significant in an aqueous solution. Other requirements are durability, ease of fabrication, transparency, biocompatibility, chemical compatibility for the right chain reaction of reagents, ideal temperature, and pressure conditions, and surface functionalization[56,57].

Common substrates used are glass, silicon, metals, polymers, and ceramics, each one with advantages and disadvantages, depending on its purposes[56–61]. Metals are cheap, widely accessible, easy to machine; and can withstand high heat loads, high pressure, and toxic chemicals. Not only that but metals are also practical for cleaning processes. The most used metals are aluminum, copper, and iron. Metal-based microfluidic devices are optimized for nanomaterial synthesis. However, these substrates are mainly used for nanomaterials synthesis[56]. Silicon is also used due to its ready availability, chemical compatibility, semiconducting properties, and thermostability, although its opacity is difficult for optical analysis making it incompatible with bioimaging procedures. It is also complicated to create a silicon-based device due to its fragility and high elastic modulus[56,57,60]. Glass can be biologically compatible because it is chemically inert, thermostable, electrically insulating, optically transparent, and easy to be cleaned. However, glass can be expensive, and is time-consuming to manufacture microfluidic devices[56,60]. Ceramics are also great due to their unique surface chemistry, good resistance to corrosive environments, and good stability at high temperatures, but they also show limitations in dimensional stability, porosity, and brittleness for micro-manufacturing[56,60]. Alternatively, polymers present low costs and are less time-consuming to create microfluidic devices. These polymers are favorable for optical microscopy due to their transparency and have the same advantages as glass and silicon. One of these polymers is PDMS[56,60,62]. Polymers are a chain of monomers that can be divided into sub-groups, such as thermosets, thermoplastic, and elastomers, depending on their shape molded when exposed to heat. Using a cross-linker, as a curing agent for the polymer, the material becomes a thermoset meaning the polymers can’t melt at high temperatures[60].

These microfluidic devices can be fabricated using chemical (ex: lithography, powder 3D printing, and inkjet 3D printing), mechanical (ex: injection molding and hot embossing), laser-based (ex: stereolithography and two-photon polymerization), or hybrid processes (ex: soft lithography and layer-on-layer manufacturing)[56,57,60]. Due to the high interest in microfluidic devices, scientists have been performing the design and fabrication of cost-effective biomedical analysis chips. One way to develop these devices is by fabricating a master using 3D printing and then putting it in a polymeric platform by using soft lithography[57].

2.1.1 – AutoCAD software

AutoCAD Software (**Figure 2.1**) is one of the available CAD software used to design microfluidic devices [63]. "CAD" stands for "Computer-Aided Design", with AutoCAD being capable of creating a variety of dimensions and shapes for a microfluidic device, depending on its context for biomedical purposes[64,65]. This software can create two-dimensional (2D) and three-dimensional (3D) models and then convert them into numerical data, which is used for the manufacturing of microfluidic equipment, such as building geometrical shapes, or copying objects, aligning and joining them together, and organize objects into defined layers according to "x", "y", and "z" axis[66–68].

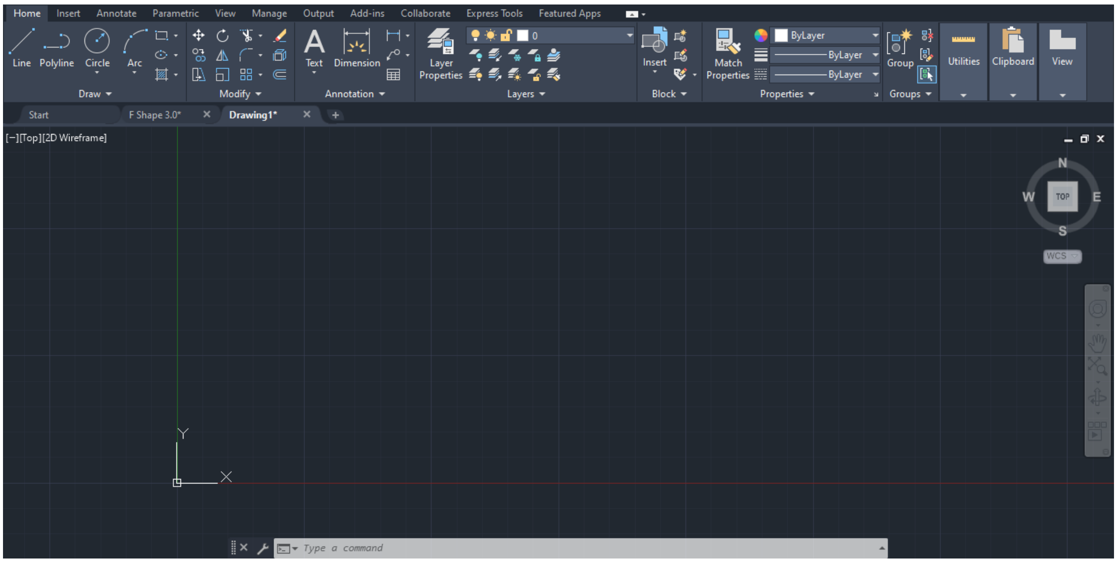

Figure 2.1 – AutoCAD template

2.1.2 – Lithography

Lithography is a method of transferring a two-dimensional pattern to a flat substrate. This method can be done by directly writing the pattern, or transferring the pattern through a mask/stamp. The pattern designed in CAD software will determine the features present in the substrate. These features can be made with the use of a photoresist, electron-beam resist, or physical stamping. Later, the features are transferred into another layer through etching, electroplating, or lift-off[69].

Soft Lithography, also known as “casting”, is the most used method for fabricating biomedical microfluidic devices, especially with PDMS material. It allows the processing of elastomeric polymers and the patterning of surfaces on devices. This technique requires a master where PDMS is used to create a replica of the mold, followed by heat-curing, and peeling off the polymer, forming a Replica [56,70]. This master can be used repeatedly in many types of designs with the main advantage of this technique being the fabrication of high-resolution replicas at a fast pace with lower costs[56,63,71].

Direct Laser Writing (DLW; also known as Direct Write Laser – DWL) is a photolithographic technique that creates permanent micro and nano-patterns with different microstructures exhibiting high spatial resolution on photosensitive substrates (**Figure 2.2**). Based on photochemical processes, is a simple, low-cost, mask-free, and path-directed method that can provide large-area structures with micrometer resolution[72]. It can be modulate the laser's intensity until a chemical reaction is initiated in the photoresist. This process can be performed on a surface with a small focal volume[73,74]. The laser's solubility changes in the exposed regions as it passes through the photoresist surface. This process can then be followed by the development of the film, which can lead to high-quality surface relief patterns. To achieve better surface relief, controlling the angle between the laser beams and the shape of the surface can be performed[72–74]. The spot size, the photoresist material, and the acceptable writing speed, exposure time, laser power, and dose, are also important requirements for creating a high-fidelity and desired pattern[74].

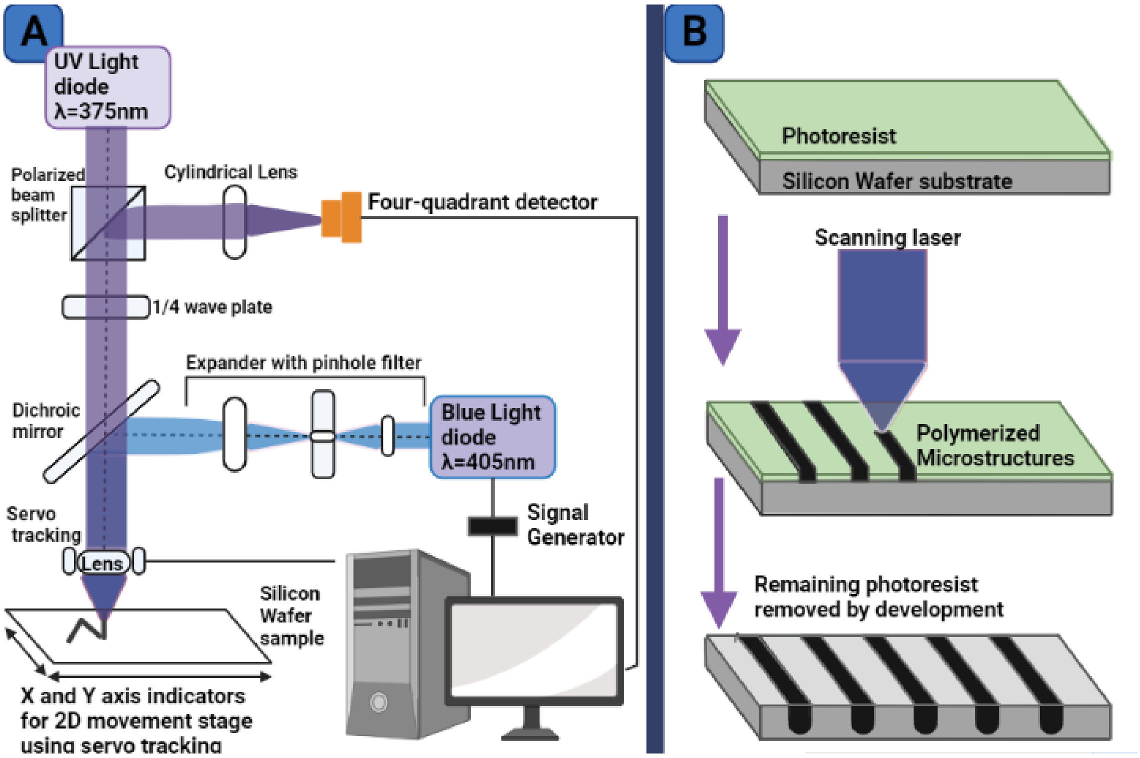

Figure 2.2 *– Direct Laser Writing representation.* ***A*** *– DLW schematics.* ***B*** *– DLW mechanism setup*[73,74]

2.1.3 – Photoresist

A photoresist is a photoactive polymer suspended in a solvent used in lithography processing and can be categorized as a positive or negative resist[75]. Epoxy-based, negative photoresists are frequently used for microfluidics fabrication (e.g. SU-8)[59,62]. Using a mask defining the desired design, the master is exposed to UV light and the exposed areas are hardened, while the non-exposed parts of the master stay soluble and can be etched away[60,63,76]. With a positive photoresist, the exposure of UV light changes its chemical structure, becoming more soluble in the photoresist developer[77,78]. These exposed areas are then washed away with the photoresist developer solvent, leaving the non-exposed underlying areas of the photoresist to define the desired features[77]. An example of a positive photoresist is AZ 4110 (**Figure 2.3**) (1-Methoxy-2-propyl acetate - CH3CH(OCOCH3)CH2OCH3)

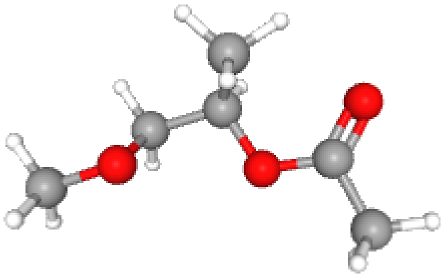

Figure 2.3 **–** *Chemical Structure Model of AZ 4110 photoresist*[78]**.**

2.1.4 – Silicon wafers

A silicon wafer is a thin semiconductor material slice used in the fabrication methods (e.g. photolithography) of integrated circuits and other microdevices. These wafers are obtained from natural "Si" crystalline structures with different orientations, for example {100} and {111} according to Miller's index (**Figure 2.4**)[79,80]. These mathematical descriptions are obtained through the silicon crystal planes and their angles, allowing the specification, investigation, and discussion of specific planes and directions of a crystal, defining the direction of vectors that induce the surface of a particular plane or facet. Obtaining these geometrical {hkl} axial values can form a stereographic projection of crystalline orientations that can differentiate crystals from the same element to infer which crystal plane is exposed on the wafer surface[79–81].

The silicon crystals are regular, well-ordered atomic lattice structures. A lattice consists of stacked planes of atoms. Because the atoms of the crystal fit together repeatedly and are held together by strong electrical attractions between each other, a crystal is typically very strong[80]. Moreover, a Si atom has four valence electrons that are shared with four other atoms to form four covalent bonds when forming a crystal, meaning that every valence shell of an atom is complete which gives a solid wafer that is electrically stable and a poor conductor of heat[79–81].

The science of crystallography is essential for micro and nanotechnologies since it provides information for the design and development of micro and nano-sized components. The orientation of Si crystals determines the properties of the wafer, the number of atoms on the wafer surface, and the conductivity and reaction potential. By choosing a specific wafer crystal orientation and etchant, one can create a variety of differently shaped microchannel structures[80–82].

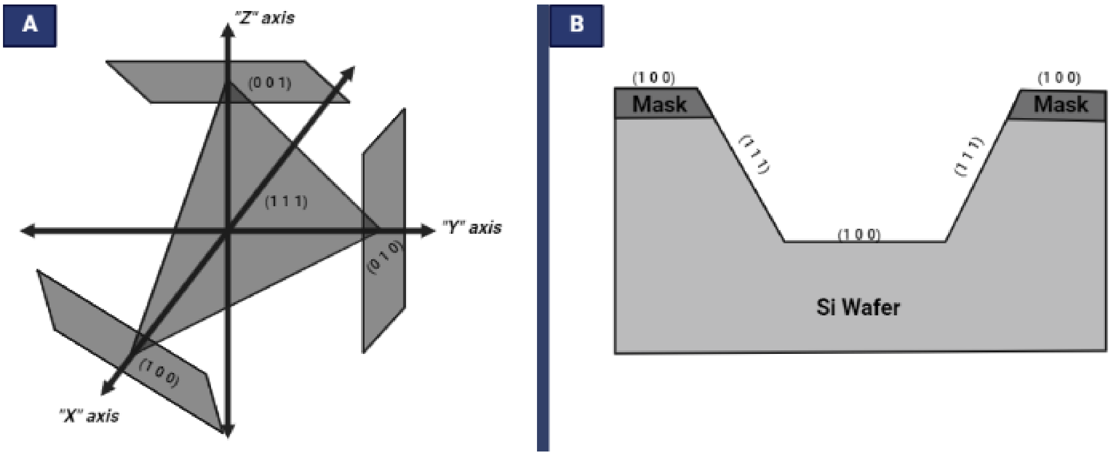

Figure 2.4 – *Silicon wafer crystallography. A – Crystal orientation of silicon. B – Representation of microstructures formed, using a mask on a silicon wafer to preserve after etching*[79–81].

2.1.5 – Production of PDMS-based devices

PDMS (Polydimethylsiloxane; $CH_3[Si(CH_3)2O]nSi(CH_3)3$) is a low-cost and easily molded elastomer. Elastomers are weakly crosslinked polymers - rubber-like materials that can change their form and return to their original shape using external pressure and removing it respectively, making them ideal for applications involving pumps, microvalves, and micromixers [60,62,83]. The crosslinker concentration can induce physicomechanical characteristics to a great extent, providing more stable PDMS molecular structures[71].

PDMS is also good for prototyping, granting optical transparency, gas permeability, biocompatibility, low autofluorescence, natural hydrophobicity, and high elasticity and chemical inertia[56,60,62,71]. This material is excellent for long-term cell culture, cell screening, and biochemical assays to determine, for example, proteins and DNA for biomedical applications[56,57,84]. A thin membrane of PDMS can also be used to, for example, create systems of valves and pumps[85]. However, optimization of these devices is needed to obtain the desired properties and to determine their final application. PDMS-based devices tend to be irreversibly bonded with a glass substrate, using an oxygen plasma, inducing changes in the PDMS chemical properties, in which silanol groups (Si-OH) are integrated into the PDMS chemical formula[62,71]. Another major disadvantage is the fact that PDMS is an adsorptive material that many molecules, for example, hydrocarbon-based solvents, can easily diffuse into the channel walls, inducing swelling of the microchannels[71]. Also, liquid evaporation occurs inside the channels over time, which can lead to changes in the concentration of a determined solution in longitudinal studies and low zeta potential[56,71]. Not only that, but this material is often soft, therefore prone to deformations if there are no precautions. Finally, PDMS also requires cleaning procedures to avoid quality reduction[56,86].

2.1.5.1 – Master

To start the fabrication of a microfluidic device, firstly the master needs to be developed. Silicon-based masters contain the designs of micro or nanostructures previously developed on the surface that are usable for replication procedures of microfluidic devices. The master should have positive and negative (or inverted) features to form the desired micro or nanostructures. The fabrication of a master can be costly and time-consuming, thus it should be optimized to include as many device designs as possible and handled with extreme care.

Post fabrication, a silanization process is required for the functionalization of the silicon wafers. The silane compound creates a monolayer of adsorption on the surface of the wafer in order to hydrophobize it, which enhances silica-elastomer interactions, reduces filler-filler interactions, and lowers the compound viscosity[87]. This way multiple replicas can be fabricated and demoulded without damaging or destroying the master.

2.1.5.2 – Replicas

Replicas (**Figure 2.5**) are flexible materials obtained from printing, molding, and embossing micro and nanostructures [88]. The PDMS liquid polymer is mixed with a cross-linker and then poured onto the mold. A desiccator used for degassing is required to remove bubbles induced by the mixing in the molded structure. An oven is used to cure the PDMS at 65° C for at least 2 hours[60,63]. The moulded design present in a replica maintains its integrity after being exposed to a plasma treatment that binds the replica to a glass substrate [56,60,76,83].

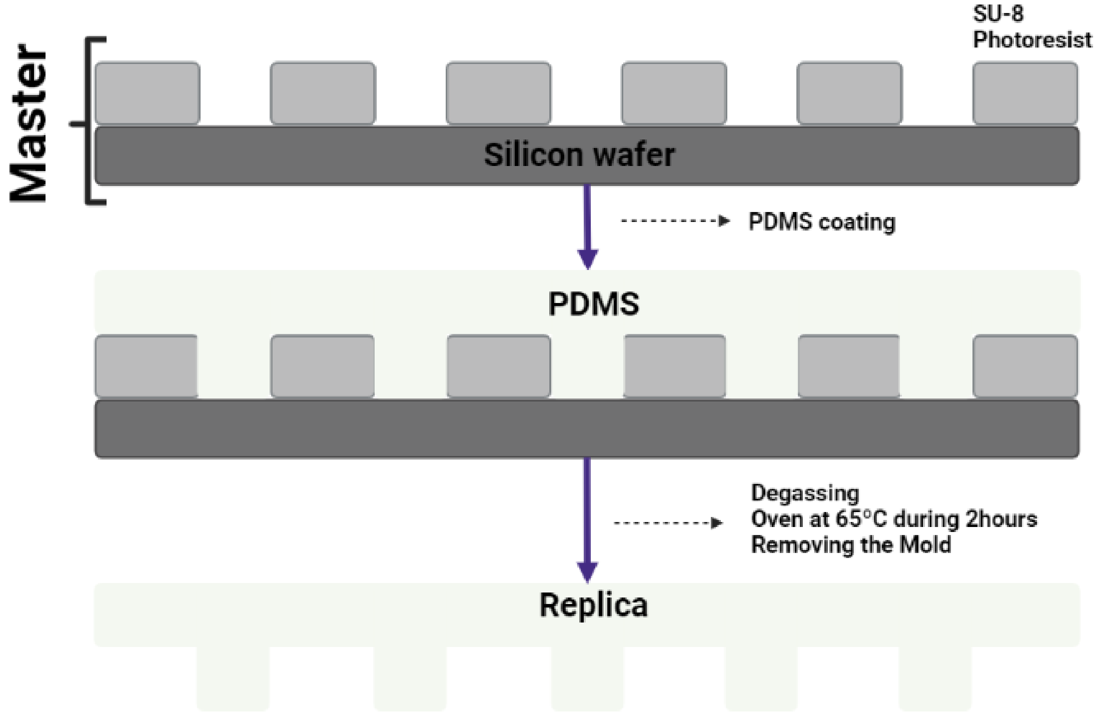

Figure 2.5 ***–*** *Fabrication of replicas using soft lithography*[75,89]

2.1.5.3 – Plasma cleaner

With this machinery, the surfaces properties of PDMS and the glass substrate are changed by increasing the exposure of silanol groups (-OH) at the surface of the PDMS layers so that they form strong covalent bonds (Si– O–Si) when connected with glass, forming an inseparable seal between the layers (**Figure 2.6**). The quality of this procedure is determined by the bonding area and strength of the material[62]. The surface of PDMS becomes more hydrophilic due to the silanol groups formed after plasma treatment. A combination of polyethylene oxide (PEO) with PDMS is used to prolong the hydrophilicity[71].

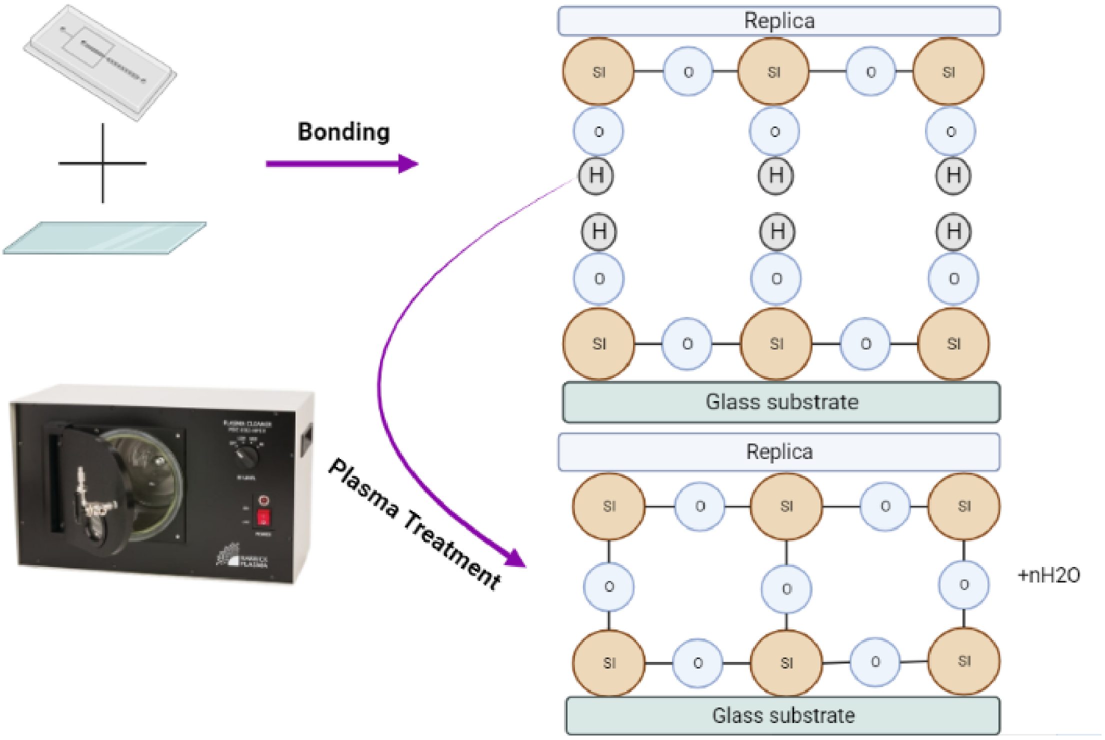

***Figure 2.6** – Molecular interactions during the bonding procedure before and after plasma treatment respectively.*

2.2 – Microfluidic mixers

Micromixers are a sub-type of microfluidic systems with the purpose of mixing two different solutions. These mixers need an appropriate design for enhanced fluid mixing capability[90,91]. Mixing at a microscale is a hard task since the system works with a laminar flow, where mixing mostly occurs due to diffusion. Alternatively, designs with structures that induce chaotic advection can induce mixing at much faster and more efficient rates[92]. Mixing is essential in LOC devices for micro-analysis in biology, chemistry, and health branches[91,93], with efficient mixing inducing a better detection sensitivity and providing a less time-consuming analysis[90]. Therefore, for the capture and detection of components in a fluid, for example, cancer biomarkers in blood samples, it is essential to have a mixing enhancement method using specific surface geometries and shapes to induce a homogenized mixed sample. The efficiency and reproducibility of capturing and detecting low-concentration targets depend on these microfluidic structures[94].

Micromixers are divided into two types: active and passive[90,91,95]. For active micromixers, the flow pattern is affected by external energy sources, such as magnetic fields, electric fields, and ultrasonic vibration, and requires a control mechanism creating a system more complex and causing difficulties in fabrication and operation. Active mixers also might damage or modify biological samples. For passive micromixers, fluids are pumped into specifically designed microchannels, and the mixing is performed by molecular diffusion and chaotic advection. Passive micromixers are economical, convenient, and can easily be integrated into LOC microsystems[90,93]. Not only that, passive micromixers are generated in multiple geometrical shapes in two-dimensional (2D) structures, three-dimensional (3D) serpentine structures, patterned groove structures, and 2D and 3D split-and-recombination (SAR) structures, and two-layer crossing channels[90,91]. While 2D structures are simpler in terms of fabrication compared to complex 3D designs, 3D printing has been emerging for the creation of more complex designs. In turn, these can enhance diagnostic devices for the detection of various clinically important analytes, such as tumour and non-tumour biomarkers present in EVs. The material PDMS allows versatile designs with different shapes in 3D without deforming the device[96,97].

2.3 – Hydrodynamic processes for the mixing of two solutions

At the microscale, the flow pattern is usually laminar and only depends on molecular interactions to induce mixing[93,95]. The design of a micromixer should be optimized to increase the contact surface area and the duration of contact between two fluidic layers such that mixing is achieved through molecular diffusion. Molecular diffusion naturally occurs across laminar flows of layers with different concentration gradients. In order to increase the contact surface area, the diffusion path should be minimized between them by, for example, creating microchannels that induce folding processes alongside the flow[94]. In addition, chaotic advection can be created through physical barriers in the microchannels to force interactions at random directions for particles of each fluid[98]. By conditioning the fluidic path with such modifications to the geometry of the microchannel, mixing can be achieved with this enhanced interfacial area and reduced diffusion length [90,93]. Chaotic advection can be generated with, for example, multidirectional vortices splits, stretching, folding, and recombinations of the flows [98].

2.3.1 – Navier-Stokes equation

Microfluidic flows are described by the Navier-Stokes equation whose formula is based on Newton's second law:

$$\sum\vec{f} = \overrightarrow{fgravity} + \overrightarrow{fpressure} + \overrightarrow{fviscous} = \rho.\frac{d\vec{u}}{d\vec{t}} \qquad \textbf{Eq. 1}$$

Equation 1 – *Newton's second law. Where these $\vec{f}$ are gravity, pressure, and viscous forces per unit of volume, respectively, $\vec{u}$ is the fluid velocity, alongside "t" that represents time, making the acceleration formula, and "ρ" is the density*[98,99].

These forces and the acceleration term can be simplified into:

$$\rho\vec{g} - \nabla\vec{\rho} + \eta.\nabla^2\vec{u} = \rho.(\vec{u}.\nabla\vec{u} + \frac{\partial\vec{u}}{\partial t}) \qquad \textbf{Eq. 2}$$

Equation 2 – *Simplified Navier-Stokes formula. Where "g" is gravity, "∇" is the volume fluid, and "η" is the fluid dynamic viscosity. This simplification can only be applied if the density remains constant.*

However, these flows are used at a microscale level, meaning the gravity can be discarded, the convective term with advection operator is nullified because of unidirectional fluid property and the fluid is steady[100], therefore the optimized equation for microfluidic systems is:

$$\nabla\vec{p} = \eta.\nabla^2\vec{u} \qquad \textbf{Eq. 3}$$

Equation 3 – *Navier-Stokes for microfluidics formula. Where pressure forces balance viscous forces*[98,99].

2.3.2 – Reynolds' number

Reynolds' number (Re) formula is used as a dimensionless quantity to analyze the Newtonian movement of a fluid based on the ratio between inertial and viscous forces[94,101]. The formula can be written as:

$$Re = \frac{\rho.u.Dh}{\mu} \qquad \textbf{Eq. 4}$$

Equation 4 – *Reynold's Number formula. Where ρ is the density of the fluid, "u" is the velocity of the fluid, "Dh" is the hydraulic diameter, and "μ" is the viscosity of the fluid. Dh is often calculated as the area of the cross-section divided by its wetted perimeter, while the flow speed can be measured with the area divided by the flow rate*[94,101].

2.3.3 – Microchannels geometry

Microchannel geometry tends to be cylindrical or rectangular. To measure Dh, it is possible to measure the ratio between the area of a cross-section (A) and the wetted perimeter (P_{wet}):

$$Dh = \frac{4A}{P_{wet}} \qquad \textbf{Eq. 5}$$

Equation 5 – *Hydraulic diameter formula. Since A=πr*^{2} *and P=2πr, Dh ends up being "2r", in other words, the diameter of the cross-section. For rectangular microchannels, Dh= the width*[93,102]*.*

2.3.4 – Flow rate

Flow rates (Q), i.e., the volume of fluid being moved per unit of time, are easily controlled through syringe pumps designated for microfluidics[69]. The main advantage of syringe pumps is their capability to control the flow rate across microchannels independently of the fluidic resistance since the pressure gets adapted to preserve the flow rate[99,102–104]. The flow velocity (u) is then obtained through the ratio between a cross-section area and the flow rate:

$$u = \frac{Q}{A} \qquad \textbf{Eq. 6}$$

Equation 6 – *Flow rate "Q" formula, where "A" is the area of a certain cross-section, and "u" is the flow velocity.*

2.3.5 – Diffusion coefficient

The diffusion coefficient (D) is the amount of a particular substance that diffuses across a unit area in 1s under the influence of a gradient of one unit, which means the mixing process combined with velocity values will determine the diffusivity of each particle. It is usually expressed in the units $cm^2.s^{-1}$. Quantitative analysis of diffusion is a crucial step in understanding and modeling transport phenomena that take place in the chosen system. At the microscale, diffusion is a rapid separation mechanism for the extraction of small samples from the stream of the mixed solution[105]. The equation applied for measurable quantities of a determined sample is:

$$D = \frac{k_B T}{6\pi r \mu}$$ **Eq. 7**

Equation 7 – *Thermodynamic diffusion coefficient formula. Where "k_B" is Boltzmann's constant, "T" is temperature, "μ" is the solvent viscosity and "r" is the radius of the microchannel*[106]*.*

An alternative way is through the measurements of the width of the microchannel (x) and the time required for the fluid to be mixed (t) [106,107]:

$$x^2 = 2Dt$$ **Eq. 8**

Equation 8 – *Hydrodynamic diffusion coefficient formula. Where "x" represents two referential distances forming the width, and "t" is time.*

2.3.6 – Peclet number

Peclet number (Pe) represents the ratio between the mass transport due to convection and diffusion[107,108]. The equation can be expressed as the following:

$$Pe = \frac{uL}{D}$$ **Eq. 9**

Equation 9 – *Peclet number formula. Where "u" is the fluid velocity, "D" is the diffusion coefficient and "L" is the characteristic length of the channel*[100,106,109]*.*

2.4 – Mono and multi-layered microchannel shapes

Multiple structures (**Figure 2.7**) can be found in literature, such as "T", "Y", "L", "F", "X", "D", "Ω", and "O", shapes (**Figure 2.8**) for serpentines, split and recombination, spiral, curved helical, patterned grooves, square-wave, zigzag, and SHMs in 2D and 3D[90,91,110].

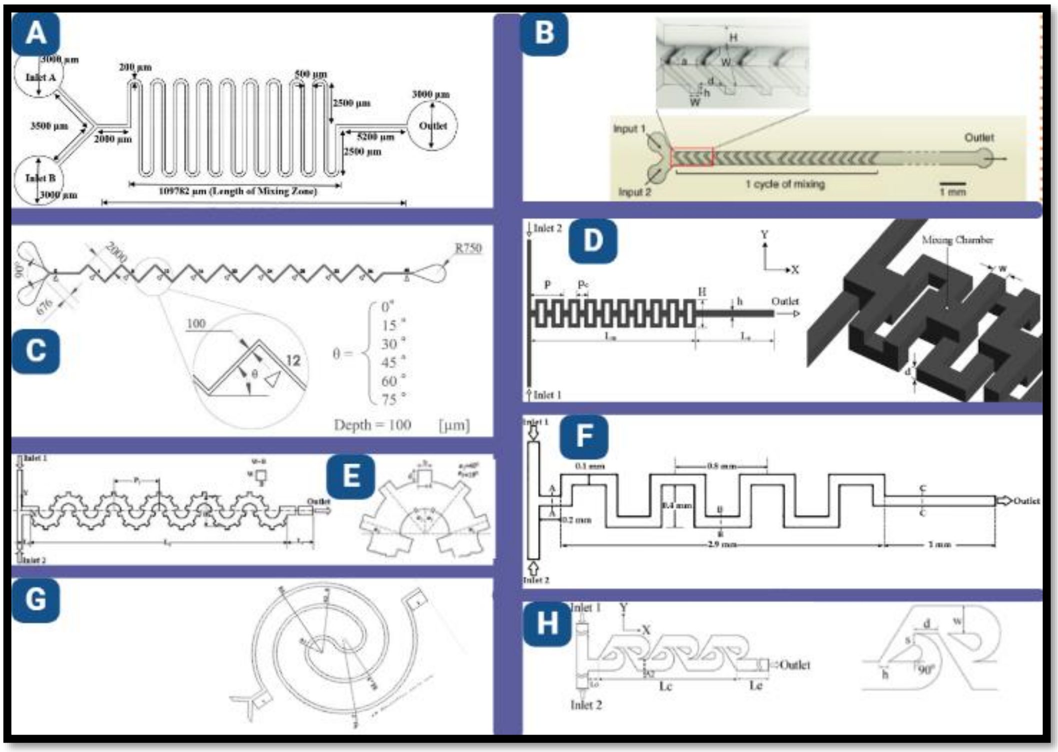

__Figure 2.7__ – Common structures present in micromixers. __A__ – Serpentine Mixer[107]. __B__ – Staggered Herringbone Mixer[93]. __C__ – Zigzag Mixer[101]. __D__ - Split and Recombination Mixer[90]. __E__ – Patterned Grooves Mixer[90]. __F__ – Squared-wave Mixer[90]. __G__ – Spiral Mixer[103]. __H__ – Modified Tesla Mixer[90].

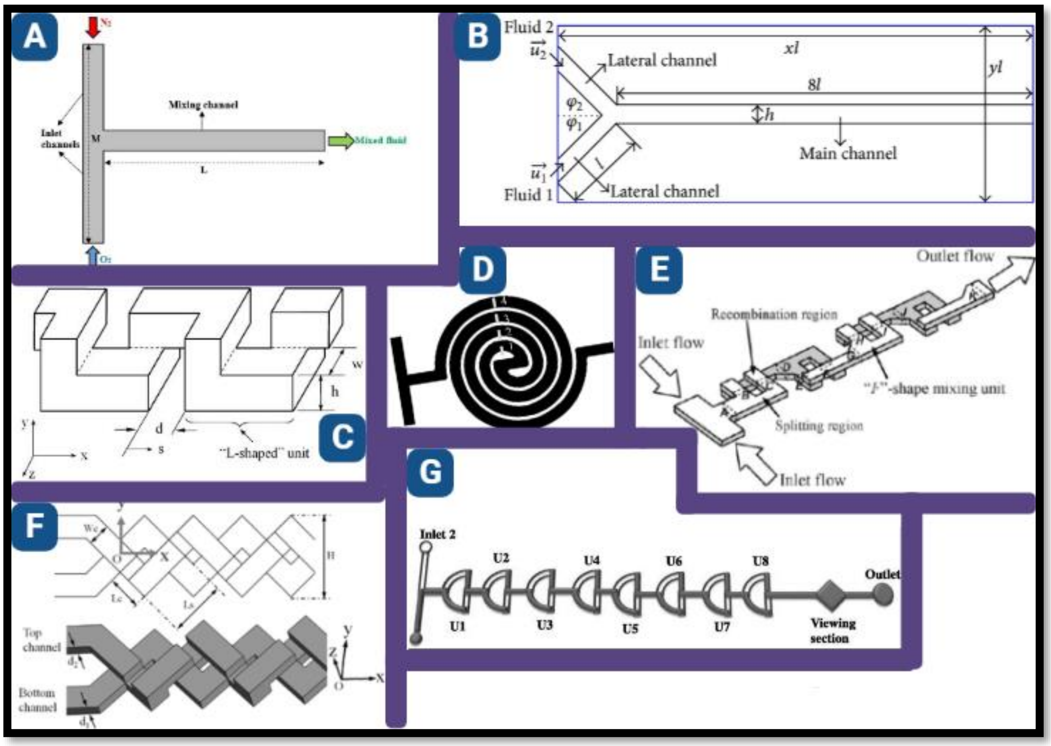

Figure 2.8 – Types of 2D and 3D structural shapes in microfluidics. **A –** "T" shape[108]. **B –** "Y" shape[111]. **C –** "L" shape[90]. **D –** "O" shape[90]. **E –** "F" shape[90]. **F –** "X" shape[90]. **G –** "D" shape[99].

2D serpentine, spiral, and curved helical channel mixers depend on the advection caused by the secondary flow or Dean vortices induced by the inertia force. Dean vortices induced by “S”-shaped serpentines can increase the mixing efficiency. These are fluid motions that recirculate the flow perpendicular to the main flow direction due to centrifugal effects experienced along a curved path[103]. The more these hydrodynamic phenomena are expanded, the higher Reynolds’ number becomes. The SAR micromixers cause multi-laminating flow patterns successively conditioned by flow mechanisms of splitting, recombination, and rearrangement, while Dean and expansion vortices are conditioned in curved channels and expansion-contraction at high Reynolds numbers[90,91].

3D serpentine path induces a stirring flow at each bending site and generates a secondary flow to enhance mixing. SAR structures enhance lamination that decreases the diffusion path and induces mixing even with low Reynolds numbers. The secondary flow, combined with a z-axial direction of the flow, creates chaotic mixing by stretching and folding the fluid interface[90,91].

SHMs take advantage of chaotic advection to achieve mixing because the grooves inserted in the walls of microchannels create whirls and transverse flows that enhance the diffusion among fluids. The most efficient design is composed of asymmetric grooves orientated to the center axis, while the long arm of the herringbone structure is 45 degrees and is orientated to the direction of the channel[93].

The zigzag channel is a type of passive mixing with a planar structure and is particularly convenient for microfluidic mixing, where chaotic advection is formed in the curves, regardless of the angle of the curvature[101].

3 – Context and Objective

The Medical Devices research group (MD) at INL (International Iberian Nanotechnology Laboratory) is mainly devoted to Translational Medical Research in close collaboration with Hospitals and focuses on the development of diagnostics tools and solutions toward an early and unequivocal diagnosis of diseases. The MD group focuses its research activities on four research lines: development of microfluidic systems for the isolation of disease biomarkers from body fluids, integration of sensitive nanobiosensors for multiplex detection of disease biomarkers from body fluids, development of organ-on-a-chip 3D models, and engineering of new optical instrumentation to undercover sub-cellular processes of disease. In relation to the topic of this Master's project, the MD group has experience in the development of microfluidic systems for the isolation of biological entities from body fluids, including cancer biomarkers, and the application of biomarkers to understand cancer progression.

Thus, the aim of this project is to develop a microfluidic system for the isolation of tumor-derived extracellular vesicles from plasma, and can be divided into the following objectives:

i. Fabrication of a microfluidic system to process complex samples
ii. Decoration of the channel surface with molecules for affinity binding of EVs, while minimizing protein extraction.
iii. Demonstrate the efficiency of the system in the supernatant of cancer cell lines.
iv. Demonstrate the validity of the system with a small number of plasma samples from breast cancer patients.

4 – Materials and Methods

4.1 – Master preparation

The master (**Figure 4.1**) is the main tool to create microfluidic devices every day, though many complex procedures are required to create the master.

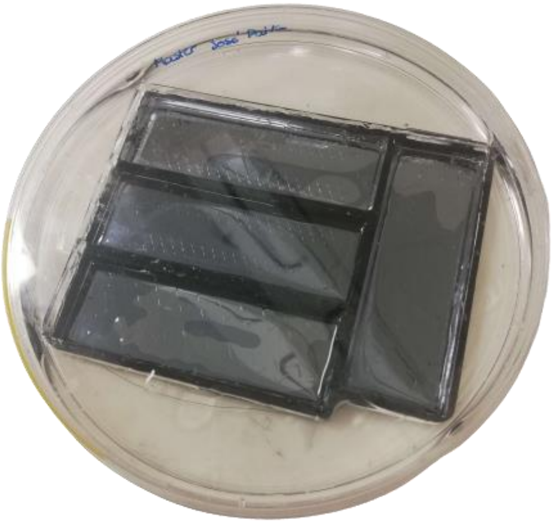

***Figure 4.1 –** Holder with four silicon masters. Black frames were made with a laser cutter and introduced between the masters so that well-shaped replicas can be collected*

4.1.1 – Elaborating a design and a master mold

The designs were made through AutoCAD software and then transferred into a silicon wafer in a cleanroom.

Fabrication of the silicon master mold is performed using a SiO2 hard mask for the silicon dry etching process. For this step, a 1 um thick plasma enhanced chemical vapor deposition (PECVD) SiO2 layer is firstly deposited on a single-side polished (1 0 0) 200mm Si wafer using a CVD system (MPX from SPTS). The wafer is then exposed to hexamethyldisilazane (HDMS, Sigma Aldrich, USA) vapour prime to improve the adhesion of the photoresist to the sample, obtained by spin coating of 1.2 µm of AZP4110 (Microchemicals GmbH, Germany) on a SÜSS MicroTec optical track (SÜSS MicroTec AG, Germany).

The DWL Lithography was used (model DWL2000; Heidelberg Instruments), for the exposure of designs on silicon wafers, known for high-resolution, laser-based maskless optical lithography systems. DWL has the capability of exposing at two different wavelengths: 405nm and 375nm, with digital design information on a 25nm writeable address grid. It writes directly on photoresist-coated quartz or sodalime mask blanks as well as on wafers as large as 200mm. The maximum speed is 105 mm^2 per minute, with a 700nm minimum structure size. It has the autofocus option either pneumatically or optically, with programmable scripts for automatic measurements of critical dimensions.

DWL 2000 was used to pattern the photoresist for the top geometry microfluidic channels. Following the post-bake, the exposed photoresist was developed with AZ400K (Microchemicals GmbH, Germany), and the wafer was rinsed with deionized water and dried. Etching of SiO2 has been completed on a reactive ion etching (RIE) tool (APS from SPTS) with C4F8 etching chemistry followed by removal of the photoresist, striped with an oxygen plasma (PVA GIGAbatch 360 M from Tepla). The silicon wafer was then etched by a dry etching process performed on an inductively coupled plasma (ICP) - DRIE tool (Pegasus from SPTS), using an SF6/C4F8 plasma, to transfer the SiO2 mask features to the bulk silicon. The top remaining SiO2 mask was removed on APS from SPTS. Trench depth was measured using a surface profilometer (KLA - Tencor P-16 Surface Profiler) until the desired depth of 100µm was reached.

Five different microfluidic device designs were explored during this project:

- ”F” shape (**Figure 4.2A**) is a 3D micromixer with 2 inlets and 2 layers, both with 250 µm width, and 100 µm altitude. Mixing starting with fluids from both inlets merging at a “T” junction and then being forced to split between the bottom and top layers. The chaotic nature of fluids constantly splitting and traveling upward or downwards between layers forces mixing to occur.
- “Serpentine 1” (**Figure 4.2B**) is a 2D mixer with 3 inlets, 200µm width in the microchannels from the start of the mixing until the end. The serpentine shape has an “S” curvy form, which causes inertial forces that induce mixing between the two fluids driven in the device.
- “X” shape (**Figure 4.2C**) is another 3D micromixer with 2 inlets. The mixing starts in a “V” junction and explores the same mixing mechanisms as the “F” shape.

- "Serpentine 2" (**Figure 4.2D**) is another 2D mixer, similar to "Serpentine 1" but having only 2 inlets.
- SHM (**Figure 4.2E**) is a mixer with 2 inlets, however, fluid enters through the first inlet and then encounters the fluid coming vertically and in the same channel from the second inlet. Two long herringbone channels, which are 200µm in width and 80µm high, then explore chaotic motion to achieve mixing. This motion is generated by the presence of 20 and 50µm grooves with 45° angles, with grooves being spaced 100µm between them.

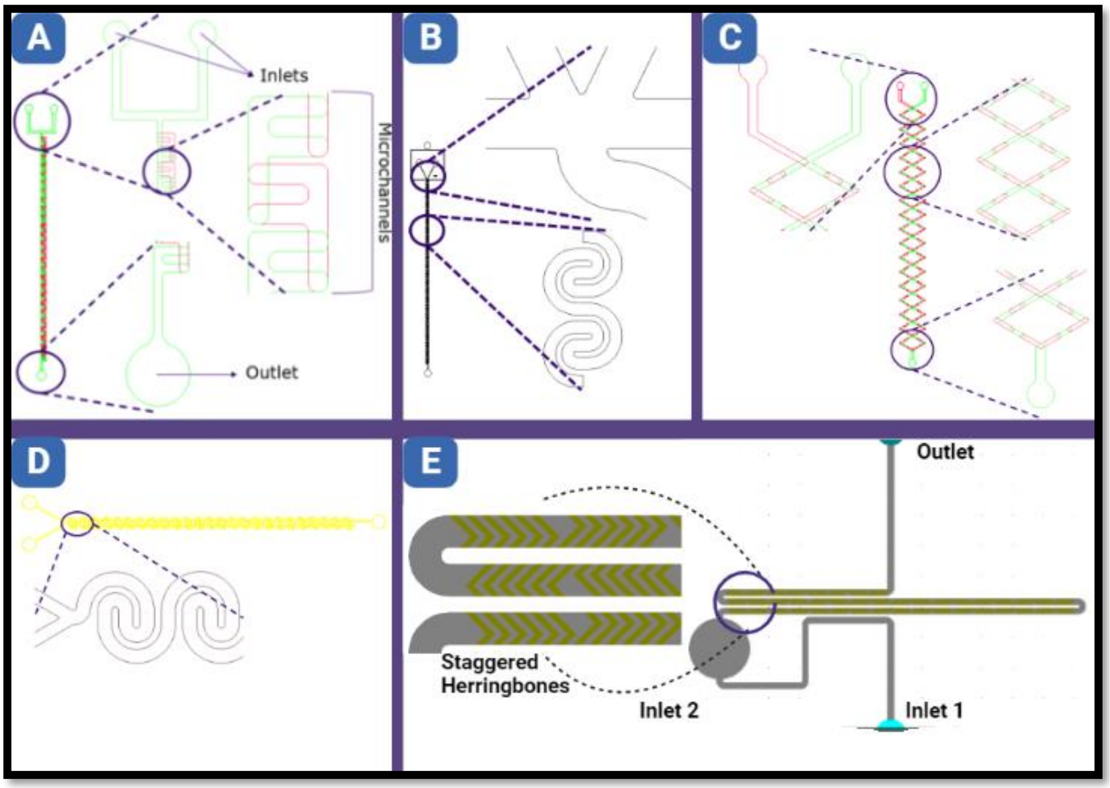

Figure 4.2 *– Designs for the development of micromixers elaborated with AutoCAD software.* ***A*** *– "F" shape micromixer.* ***B*** *– Serpentine 1 micromixer.* ***C*** *– "X" shape micromixer.* ***D*** *– Serpentine 2 micromixer.* ***E*** *– Staggered Herringbone micromixer.*

4.1.2 – Silanization - Hydrophobizing the master

In this process (**Figure 4.3**), a glass coverslip is put inside a vacuum desiccator, adding one drop of the hydrophobizing silane (trichloro 1,1,2,2-perfluorooctyl-silane) on top of it. With some tweezers, the wafer is placed inside a desiccator and then closed. A hose is attached to connect with the vacuum port in order to remove the air when the vacuum valve is opened. Once the vacuum is formed, the valve is closed and disconnected from the vacuum line. After that, the master is placed inside the oven for over 2h at 65°C or stays overnight inside the fume hood. Finally, after removing it from the oven, the contaminated glass coverslip is removed and the wafers are washed with ethanol (EtOH) and dried with a nitrogen (N_2) stream.

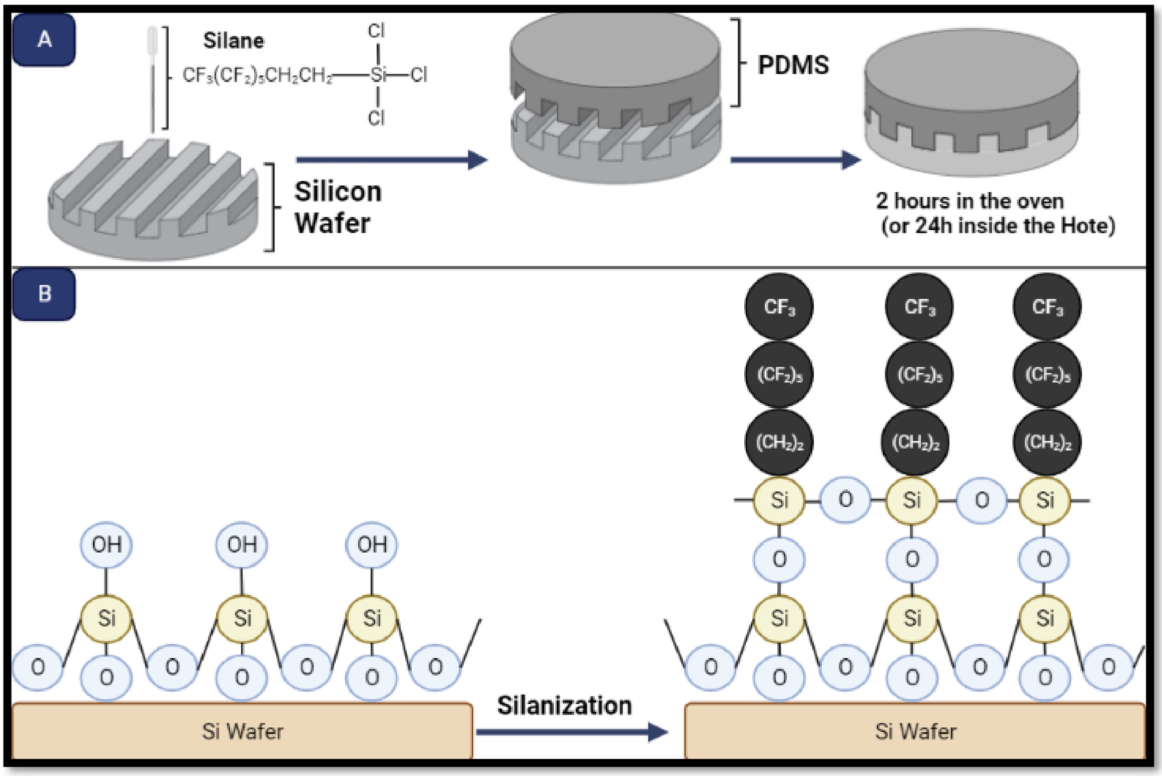

***Figure 4.3** – Silanization process for silicon wafers to create a Master **A** – Schematic scenario of the experiment inside a fume hood **B** – Molecular interactions illustration between the silane and silicon.*

4.2 – PDMS preparation

PDMS pre-polymer components (**Figure 4.4**) are weighed with a ratio of 10:1 (elastomer : crosslinker) in 50 mL cups. PDMS and the crosslinker have similar densities, meaning, for example, 40g of elastomer and 4g of crosslinker result in 40 mL of PDMS. To remove the elastomer into a cup, a 40 mL syringe is used, while the crosslinker is removed with a Pasteur pipette.

The transparent polymer inside a 50 mL cup is then mixed with a spatula until it gets filled with bubbles and a white opaque color. After that, the cups are inserted into a desiccator to remove air bubbles. This last procedure can be made repeatedly, or wait about 15 minutes to remove all the bubbles. Lastly, they can be used at the very next moment or stored inside a freezer at -20°C for further use.

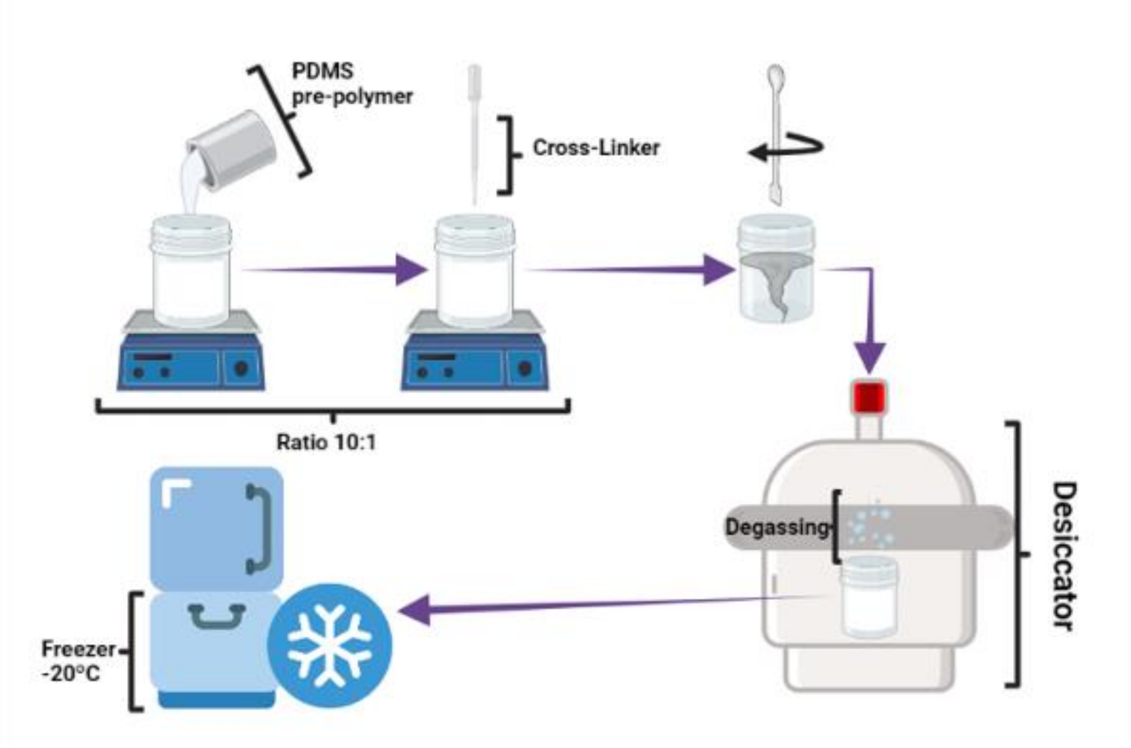

Figure 4.4 – *Schematic representation of PDMS preparation.*

4.3 – PDMS-based microfluidic device fabrication

4.3.1 – Replica formation

PDMS is poured carefully in the center of the wafer located in a petri dish to minimize air bubbles formation. The petri dish is then placed inside a desiccator under a vacuum repeatedly until no more air bubbles can be seen. The vacuum valve should be closed every time the wafer is full of air bubbles on the surface and opened again to continue the vacuum.

The petri dish filled with PDMS is cured inside an oven at 65°C for over 2h. After curing, replicas are formed and can be stored. A scalpel is used to remove replicas. The cutting is made around the edges of the silicon wafer so that the replicas can contain the designs intact.

With tweezers, replicas are removed carefully from the wafer. A puncher with a 1 mm diameter, is used to create holes in the inlets and outlets of the replicas.

The wafer is then washed with isopropanol to clean and remove small debris of PDMS and dried with an N_2 stream so that the wafer has the design ready for another procedure of pouring PDMS.

4.3.2 – Cleaning glass slides

Glass slides are previously coated with Hellmanex 1%, which is an alkaline liquid concentrate that must be mixed with milliQ water to yield an effective cleaning solution. Then the glass slides are rinsed with water and lastly, they are blown under an N_2 stream. Hellmanex 1% is prepared by adding 1% (V/V) of hellmanex III onto a 500 mL glass filled with milliQ water.

4.3.3 – Oxidizing the surface

The chamber of the plasma cleaner is cleaned with ethanol 70% and precision wipes. After ensuring that previously fabricated replicas are clean, both the replica and a glass slide are inserted inside a plasma cleaner. After closing the door, the vacuum pump is turned on with a 3-way valve ensuring the air is being pumped out of the chamber. The pressure will start decreasing and when a value close to 300 mTorr is reached, the oxygen cylinder is opened, with the 3-way valve opened to allow for oxygen to flow into the chamber. Then, the pressure will start increasing up to 900-1000 mTorr, eventually stabilizing. This procedure is usually done two times to assure the chamber is well-oxygenized for the next step.The radio-frequency (RF) is turned on, with the power level high. When the plasma is ignited, a faded white/pink shade appears. Two minutes after the ignition, RF is turned off, and the oxygen flow and the 3-way valve are also closed. The vacuum pump is then turned off, the ventilation valve opens and, after ventilating, the chamber is opened and both the replica and glass slide are removed.

4.3.4 – Bonding and tubing

When bonding, the active surface of the replica makes contact with the glass slide with the help of some tweezers. The pressure is carefully applied to the corners to avoid ruptures in the microchannels. The devices are then visualized under an optical microscope to assure the channels are intact.

For the tubing insertion, approx.. 20 centimeters of polyethylene tubing were introduced in the inlets and outlets of the devices, penetrating half of the PDMS thickness. The tubings connected to the inlets are plugged, on the other side, into needles from orange needle connectors (0.5x25mm) which, in turn, are attached to 4.7mm in diameter, 1 mL syringes.

4.3.5 – Modified procedure for multi-layered devices

For the “F” and “X” shapes, some alterations were needed to obtain full-functioning mixers. The main obstacles are the thickness of each layer, the alignment, and the plasma treatment. For microscopic visualization, each layer replica needs to have a thickness that allows for focusing and visualization of both layers at the same time. Furthermore, it is required to use the plasma cleaner in two different runs. The first run is to ensure the bonding of a glass slide with the backside of a replica that holds the lower layer of the design. The next bonding procedure is to bond both replicas whose designs are already aligned with each other. Since both replicas have their surfaces in contact with one another, instead of having their surfaces exposed to the plasma, this treatment is required to be performed three or four times to assure both layers are well bonded. Not only that, but after using the plasma cleaner, the device tends to have all edges well bonded but with some small chambers of air in the gap between the replicas that can compromise the molecular bonds. Therefore, if there are air chambers visible, pressuring them manually until the air reaches the inlets and outlets is important, and then put the device again inside the plasma cleaner. The alignment is made with the help of a custom microscopic tool (**Figure 4.5**) where it is possible to visualize a more amplified area of the microchannels in order to adjust manually the top design with the bottom one.

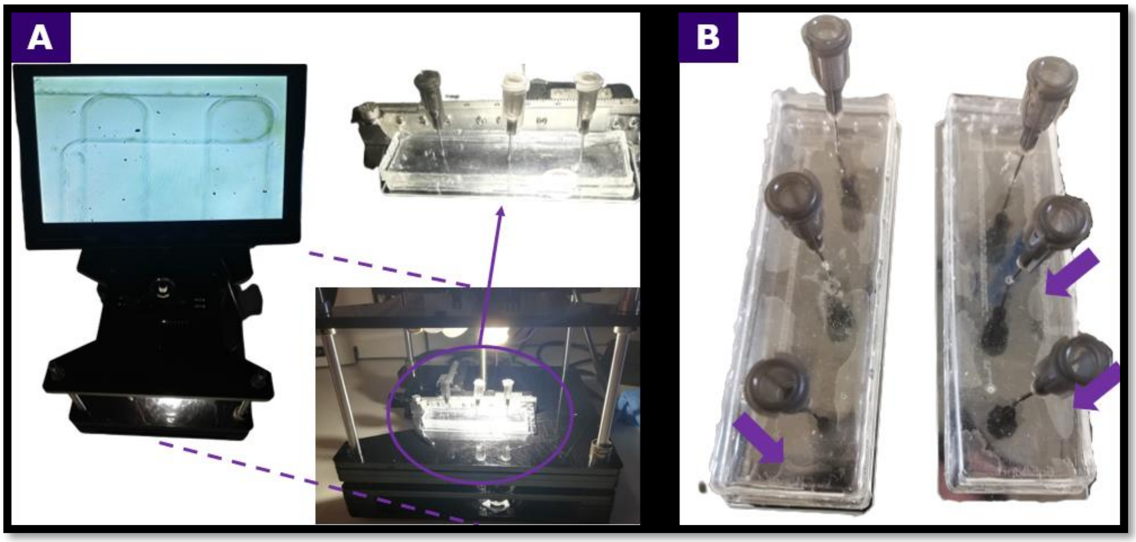

***Figure 4.5 –** Fabrication of multi-layered microfluidic devices. A – Alignment procedure. The pins, inserted in the middle of the replica, are used to maintain the design aligned while being inside the plasma cleaner. B – Arrows indicating air entrapped after the first bonding that needs to be pushed towards the inlets and outlets.*

4.3.6 – Polyurethane moulds

In order to enhance and streamline replica fabrication, an alternative type of mold, without the need to prepare another silicon wafer in the cleanroom, can be created using polyurethane. This would reduce time-consuming procedures to prepare more replicas. One component necessary is SmoothCast310, which generates liquid plastics with ultra-low viscosity that yield castings that are virtually bubble free. Another component is a silicone baking tray where a replica is inserted to create a counter-mould. Using double-sided tape, the replica adheres to the bottom layer. Then the adhered replica with the silicon recipient is degassed.

Components A [4,4'-methylene bis(phenyl isocyanate) (MDI); Benzene, 1,1'-methylene bis(4-isocyanate) diisocyanate] and B (Polyurethane polyols) agents of the SmoothCast310 are shaken for ten minutes. Inside a fume hood, A and B are combined using equal volumes (the value of the volumes depends on each type of silicone mould and device) and then are inverted and shaken for two minutes. Finally, this mixture is poured over the structures of the replica and degassed for over ten minutes. This recipient stays overnight in a well-ventilated area, in the next day, it stays in the oven at

65°C for over four hours. After removing the recipient from the oven, the holding block is discarded. The final polyurethane mould (**Figure 4.6**) with the desired design is then ready for PDMS fabrication.

***Figure 4.6 –** Polyurethane mould for the staggered herringbone micromixer*

4.4 – Device optimization

The optimization of the devices was performed by using a syringe pump and visualizing through microscopes, mainly Nikon MA200 Microfluidics Microscope and Nikon Ti-E Microfluidics Fluorescence Microscope. After that, the images obtained through the microscopes were analyzed through software, such as ImageJ and Microsoft Excel.

The syringes (1mL total volume; 4.7 mm diameter) are run using a syringe pump, which is programmed with different flow rates (from 60 to 200 µL/min). Ethanol is the first sample run through the device. A Nikon ECLIPSE MA200 Microscope is then used to visualize the flow mixing (see **Figure S.6**), and to determine optically if the device presents leakage issues or air trapping for example.

4.4.1 – Food dye assay

To assert well-functionalized devices, red, and blue food dye solutions are prepared to observe microscopically and with the naked eye the formation of the colour purple post mixing. For each food dye, three 2.0 mL Eppendorfs are filled with 1.5 mL of milliQ water and 0.5 mL of food dye and mixed by handshake. The syringes are then filled with food dye and the procedure using the pump is the same as during optimization steps, with the mixing being observed as the flow of the sample within the different devices.

4.4.2 – Fluorescence assay

To enhance mixing assessment, one syringe is filled with phosphate-buffered saline (PBS) mixed with 1mM fluorescein, while the other syringe is simply filled with PBS. Using the Nikon Ti-E Microfluidics Fluorescence Microscope, it is possible to visualize the fluorescence spreading into a multi-layered mixed solution until it reaches a homogenized pattern if total mixing is achieved (see **Figure S.1; S.2)**. A quantitative method can then be created by assessing levels of fluorescence long the duration of the devices.

PBS was prepared using 1 tablet per 200mL of milliQ water to obtain a 137 mM NaCl, 2.7 mM KCl, and 10 mM phosphate buffer solution (pH 7.4 at 25 °C). Then the solution was mixed centrifugally using a magnet and a metallic base inside a fume hood. Finally, the mixed PBS is filtrated using a filtration tool onto a 50mL falcon tube. Fluorescein (3′,6′-dihydroxyspiro[isobenzofuran-1(3H),9′-[9H]xanthen]-3-one) (**Figure 4.7**)is a synthetic organic photoactive dye compound, which has as good water solubility and absorption, emission, and maximum brightness at physiological pH[112].

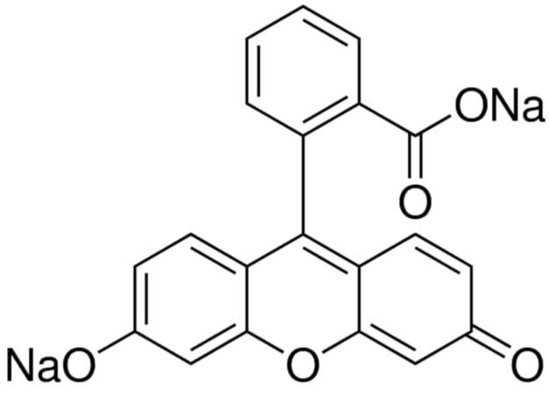

Figure 4.7 – *Chemical formula of fluorescein sodium salt*

Fluorescein, in the form of powder with a molecular weight of 376,27 g/mol, is mixed with milliQ water to have a 50-milliliter falcon tube full of fluorescein at 10 mM in liquid form. PBS is then conjugated with fluorescein using another falcon tube at a ratio of 10:1, reaching a final concentration of 1 mM (**Figure 4.8**).

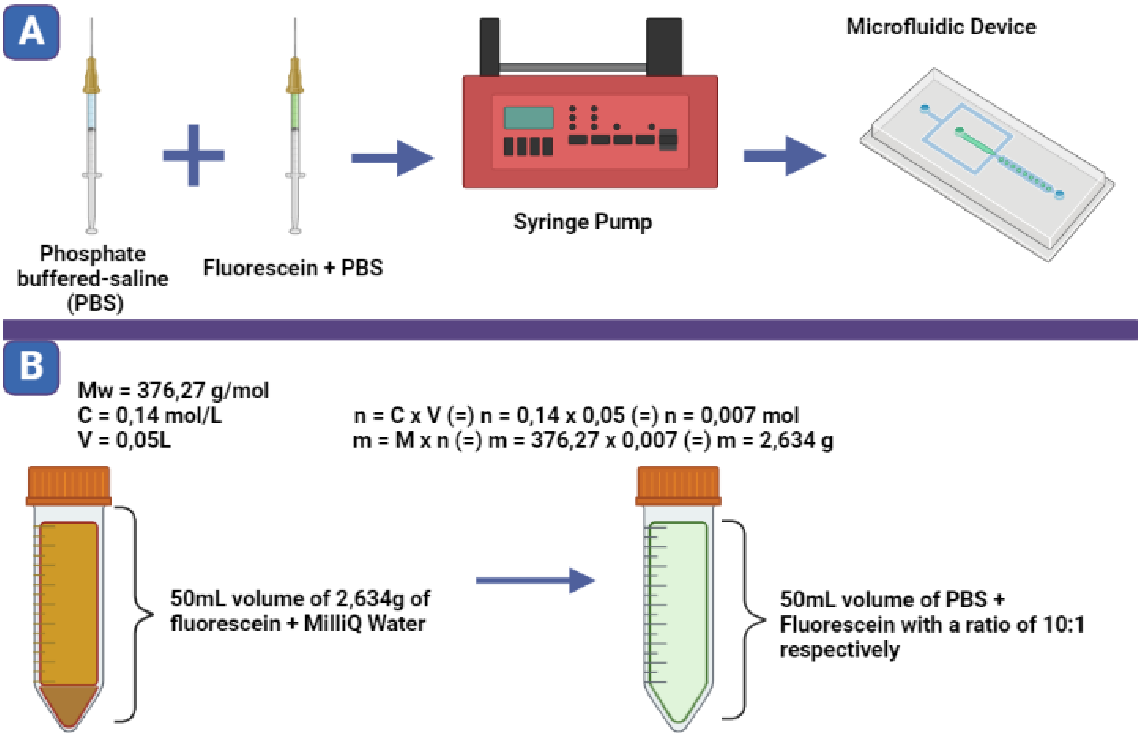

Figure 4.8 *– Initial steps for the device optimization.* ***A*** *– Pumping setup using the fluorescence assay for device analysis.* ***B*** *– Calculations and dilution procedures for the optimal fluorescence intensity for image acquisition with the Ti-E fluorescence microscope.*

4.4.3 – Fluorescent magnetic beads assay

Magnetic beads with fluorescence properties have been used for fast and reliable diagnostics. They grant target detection by capturing the analyte inside fluid samples. Not only that, in micromixers, these beads can enhance binding reactions[113].

The fluorescent beads used were 100nm in size with a concentration of 3.8×10^{12} particles/mL and possess a greenish color inside the spectrum between 540 and 560nm. A dilution with PBS was made to have a falcon tube of 10 mL of fluorescent beads mixed with PBS. A volume of 5.26µL holding fluorescent beads was taken to get a final concentration of 2×10^9 particles/mL.

Fluorescent beads were tested with a SHM to compare the analysis of mixing efficiency between fluorescent liquids and fluorescent particles. 20µL/min, 100µL/min, and 1000µL/min flow rates were implemented to visualize the fluorescence emitted through binding reactions between particles (see **Figure S.5**).

4.5 – Data analysis

After the optimization, several pictures were captured along each device, across four different designs using different flow rates. Usually, mixing is quantified by processing a set of images to calculate a meaningful index that is representative of the extent of mixing. Such images are typically analyzed through image processing software, such as ImageJ, to capture raw data on intensity levels in the cross-section defined in each picture. With Microsoft Excel, this raw data is processed with three analytical formulas to estimate which combination of device and flow rate presents the best mixing efficiency.

ImageJ is a software (**Figure 4.9**) that uses 8-bit greyscale images, meaning that each pixel present in an image has eight bits. Each bit, mathematically, can be a “0” or a “1”, creating a binary system with 256 combinations. The pixel “00000000” holds the color black while “11111111” holds the color white, or, in other words, the intensity scale of every greyscale image is between 0 (“00000000”) and 255 (“11111111”)[114]. To ensure the intensity of each cross-section image of the microfluidic device is correlated with the first image where the initial mixing happens, a normalization step is performed to re-scale the intensity of each cross-section image to be comparable to that of the initial mixing position. This effectively recalculates the pixel values of the image so the range is equal to the maximum range for the data type. For example, if the initial mixing has a minimum intensity of “7” and a maximum intensity of “180”, these two numbers are “stretched” to become the new “0” and “255” respectively[115]. Normalization follows the mathematical formula:

$$I_N = (I - Min)\frac{newMax - newMin}{Max - Min} + newMin \qquad \textbf{Eq. 10}$$

Equation 10 – *ImageJ Normalization formula- Where "I" is the intensity of the original image, "I_N" is the intensity of the normalized image, "Min" and "Max" are minimum and maximum intensity values of the original image respectively, and "newMin" and "newMax" are the new minimum and maximum values for the normalized image*[115].

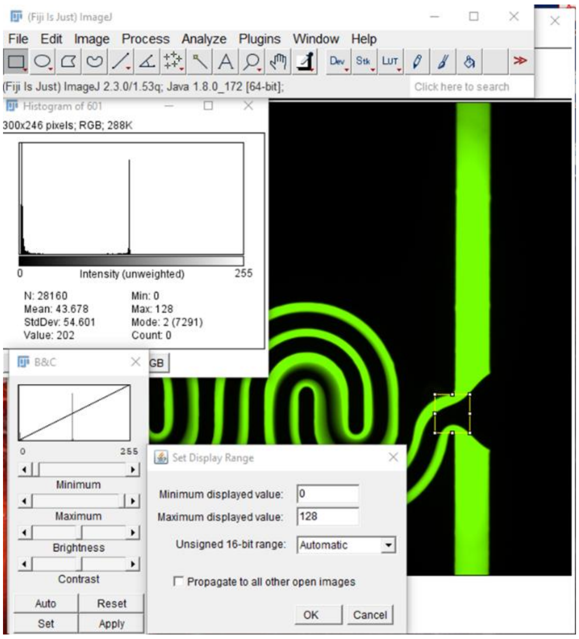

(Fiji Is Just) ImageJ 2.3.0/1.53q; Java 1.8.0_172 [64-bit];

300x246 pixels; RGB; 288K

Intensity (unweighted) 0 – 255

N: 28160
Mean: 43.678
StdDev: 54.601
Value: 202
Min: 0
Max: 128
Mode: 2 (7291)
Count: 0

Minimum displayed value: 0
Maximum displayed value: 128
Unsigned 16-bit range: Automatic
☐ Propagate to all other open images

Figure 4.9 – *Example of normalizing an image. First, select an area in the microchannel; After that, press analyzes to see histograms and then copy the "min" and "max" values into the contrast option. Finally, a new scale is created.*

A mathematical way for normalization is calculating the absolute and relative mixing indices[116]. In the images, different fluids are usually differentiated based on differences in light intensities received by a camera. However, the extent of mixing remains incomparable throughout the wide spectrum of studies on microfluidic mixing due to different solutions that differ in viscosity and fluidity, physical properties of every design, and the random nature of chaotic advection[95,101].

Standard deviation yields information regarding the spread of data about the mean intensity values obtained from ImageJ. These values are essential to analyze mixing indices[116]. The measurement of standard deviation is calculated using intensities of pixels across a cross-section of a grayscale image that delineates a mixing event:

$$\sigma = \sqrt{\frac{1}{N}\sum_{i=1}^{N}(I_L - I_M)^2} \qquad \textbf{Eq. 11}$$

Equation 11 *– Standard deviation formula. The "N" represents the total number of pixels, "I_L" is the local pixel intensity, and "I_M" is the average of the pixel intensities in the cross-section.*

Although a measure of simple standard deviation yields information regarding the spread of data about the mean intensity, it is not a direct measure of the extent of mixing since the index possesses a dimension of intensity. The absolute mixing index (AMI) can be calculated using the formula:

$$AMI = \frac{\sigma}{I_M} = \frac{\sqrt{\frac{1}{N}\sum_{i=1}^{N}(I_L - I_M)^2}}{I_M} \qquad \textbf{Eq. 12}$$

Equation 12 *– Absolute Mixing Index formula to analyze how homogenized the solution is.*

This index induces the highest value of 1 when the fluids are unmixed and 0 if the fluids are homogeneously mixed[117,118]. AMI still cannot be used for comparing mixing in different trials of devices with the same design due to different lighting scenarios of the fluorescence, in other words, it is not a direct measure of the extent of mixing because the index possesses a dimension of intensity. Furthermore, different light scenarios alongside the usage of solutions with dissimilar colors may induce different AMI despite having two hydrodynamically identical mixing events Another formula is used, named relative mixing index (RMI) that bypasses the need for any artificial pre-treatment of the intensity data, such as stretching or rescaling. RMI can be computed by taking the ratio of the standard deviation of pixel intensities across a cross-section to the standard deviation of the pixel intensities in the unmixed case, "σ_0":

$$RMI = 1 - \frac{\sigma}{\sigma_0} = \frac{\sqrt{\frac{1}{N}\sum_{i=1}^{N}(I_L - I_M)^2}}{\sqrt{\frac{1}{N}\sum_{i=1}^{N}(I_0 - I_M)^2}} \qquad \textbf{Eq. 13}$$

Equation 13 *– Relative Mixing Index formula. Where "σ_0" is the standard deviation of the unmixed section, and the "I_0" indicates the initial local pixel intensity in the unmixed flow pattern. The results given with RMI in percentage form are more versatile and allow for better comparisons between different experiments under different light or intensity conditions, thus permitting an optimal mixing efficiency or mixing ratio characterization*[111,118–120].

RMI, at this moment, has shown to be the most accurate to analyze mixing efficiency due to the detail this equation does by comparing the intensity levels from one place concerning the initial mixing.

4.6 – EV sample preparation

A sample of EVs was derived from a colorectal model cell line (HCT116) in DMEM (Dulbecco's Modified Eagle Medium) + 10% FBS + 1% P/S by standard methods of ultracentrifugation. The enriched EVs were then spiked (2µL) into different samples (1 mL) as controls, either standard DMEM or PBS. A sample (1 mL) of conditioned medium from a cell culture of SW480 lung cancer cell line in DMEM + 10% FBS + 1% P/S was also used. The conditioned medium contains all the components secreted by cells, including EVs.

4.7 – ExoGAG protocol

The ExoGAG reagent was initially filtered using a 0.2µm filter to reduce significant aggregates inside the microchannels. Since GAGs have negative electric charges that grant them a high affinity with their environment, removing larger debris reduces the possibility of aggregates being formed.

Standard ExoGAG protocol was used in two procedures for two types of samples. With fresh medium samples (2 mL), EVs were spiked at 2µL and incubated with 1mL of ExoGAG for 5 minutes at 4° C. Then the sample was centrifuged at 3000g for 15 minutes. The resulting precipitate contained EVs, which were then resuspended in PBS. With a conditioned medium (2 mL), were incubated with 1mL of ExoGAG for 5 minutes at 4° C. EVs were then collected by centrifugation (3000xg, 15 minutes), with the resultant precipitate resuspended in PBS.

4.8 – Micromixer procedure for ExoGAG and EV samples

1mL syringe filled with filtered ExoGAG and 1mL syringe of each EV sample were prepared for the pumping setup using SHM and “Serpentine 2” mixer at 100µL/min flow rate.

2.5mL Eppendorfs were filled with the mixed solutions, a solution of ExoGAG mixed with EVs spiked in a conditioned medium, and a solution of ExoGAG mixed with EVs from a cell line with DMEM.

4.9 – Nanoparticle Tracking Analysis for EV characterization

A Malvern Panalytical NanoSight NS300 is used for Nanoparticle Tracking Analysis (NTA). This instrument has a platform for EV characterization, both in terms of size distribution and concentration. It utilizes the properties of both light scattering and Brownian motion to detect and measure all types of nanoparticles from 50 - 300nm in diameter. The tool is equipped with a 488nm laser and the introduction of a motorized filter wheel meaning different fluorescent labels can be analyzed. The software tracks many particles individually and, using the Stokes-Einstein equation, calculates their hydrodynamic diameters. NanoSight NS300 also has a syringe pump system, enabling analysis in constant flow for improved sample statistics and measurement of photo-bleaching fluorescent samples. Each analyzed sample was inserted in a 1mL syringe for pumping into the NTA system. Measurements with the system can be repeated multiple times, using the same sample, ensuring more precise results.

4.10 – Dynamic Light Scattering Analysis for EV characterization

The hardware DLS Litesizer™ 500 (Anton Paar) can make a simple and straightforward measurement of the size (in nanometers), Zeta potential (ZP), molecular weight (MW), second virial coefficient (A2), transmittance, and refractive index using the same experimental setup as the subsequent scattering experiment. The DLS requires samples to be suspended in a liquid medium, usually water, PBS, or ethanol for analysis. The Malvern Nanosight Zetasizer Nano software was used to analyze the data collected with the DLS.

For size measurement, 1 mL samples were placed in cuvettes and then inserted into the instrument. A laser was used to provide a light source to illuminate the sample particles which are suspended in a Brownian motion. Most of the laser beam passes straight through the sample, but some are scattered by the particles within the sample. Finally, a detector received all the light scattered and analyzed its intensity. The intensity of the scattered light must be within a certain range for the detector to measure it without flaws. If too much light is detected then the detector will become overloaded. An attenuator is placed to avoid overloads, reducing high-intensity values of the scattering. The appropriate attenuator position is automatically determined by the Zetasizer during the measurement sequence. The scattering intensity is transformed into a digital signal through the correlator, so that, it is possible to analyze with the Zetasizer. The correlator compares the scattering intensity at successive time intervals to derive the rate at which the intensity is varying.

The measurement of Zeta potential determines the electric charge on the surface of each particle present within the sample. The liquid layer surrounding the particle exists in two parts; an inner region called the Stern layer, where the ions are strongly bound, and an outer, diffuse, region where they are less firmly attached. Between the diffuse layer and the Stern layer, there is a hydrodynamic boundary where the ions and particles form a stable entity known as the slipping plane. The slipping plane is where ZP is determined using the movement of ions that travel with particles and ions that do not. The potential stability of the colloidal system is then inferred to determine if the particles repel each other or if they tend to form aggregates To measure the zeta potential, electrophoretic mobility is needed. This value is granted by putting 1mL of the sample in a micro-electrophoresis system with electrodes (anodes and cathodes). The particles tend to move toward the electrodes with opposite charges and their movement is measured with a laser Doppler velocimetry, which then a fluctuating intensity signal is created and modulated into a digital signal. The digital signal is processed with the Zetasizer giving the respective zeta potential value.

5 – Results & Discussion

The initial experimental plan involved the testing and optimization of the 5 device designs presented in **section 4.1.1**. However, initial fabrication tests performed with the "X" shape device and innumerous issues encountered while running this specific device rendered its inclusion in the final results and discussion impossible. Thus, the following sections are concerned only with the "Serpentine 1", "Serpentine 2", SHM, and "F" shape designs.

5.1 – Microfluidics numerical properties

The various key numerical properties associated with microfluidic devices were calculated for the designs (assuming a standard, theoretical flow-rate of 100 µL/min). The resulting values (**Table 5.1**) show that all devices present values within the expected range for microfluidic devices, specifically the Reynolds numbers demonstrate that the flow patterns are laminar. Also, the coefficient diffusion values were lower than 1, meaning the mixing is not significantly induced by diffusion, and high values of the Peclet number indicate that there is more convection than diffusion, implying particles of each solution are transported and mixed by bulk motion and that diffusion is not the only mechanism happening in the system.

***Table 5.1** – Hydrodynamic values of each micromixer available for the first optimization step assuming 100µm/min*

	Serpentine 1	Serpentine 2	SHM	"F" shape	"X" shape
Flow Velocity (mm/s)	53.05	53.05	104.17	33.95	23.58
Re	14.74	14.74	16.53	11.79	9.82
D (m^2/s)	$2x10^{-8}$	$2x10^{-8}$	$2x10^{-8}$	$3.1x10^{-8}$	$4.5x10^{-8}$
Pe	265.5	265.5	1041.7	273.8	157.2

5.2 – Food Dye analysis

Preliminary tests were performed using samples of food dye with the intent of observing mixing with the naked eye. However, this qualitative approach cannot fully infer whether optimal mixing was achieved, as it becomes challenging to discern the different colors, even under the microscope (**Figures 5.1; 5.2**). Mixing blue dye with yellow dye granted a light blue sample at the end of the mixing instead of green, while blue and red gave a mixed light red instead of purple. This is due to the intensity these colours possess which one overlaps the other. This can mean the mixing might have happened, but it is unlikely to visualize. Not only that, but these results could also indicate that the chaotic advection present in the designs are not optimal. It is recommended to dilute the food dye colour which is overlapping, in order to fulfill the ideal mixing.

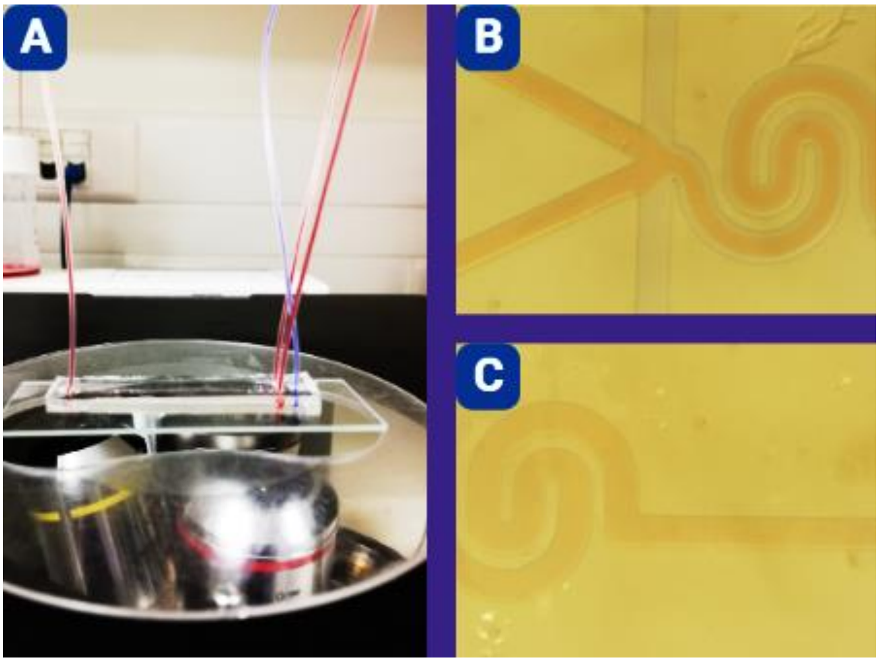

Figure 5.1 – *Food Dye assay using red and blue dyes in the "Serpentine 1" micromixer. The colour red is overlapping blue, instead of giving the colour purple. Macroscopic (**A**) and microscopic view in the inlet (**B**) and outlet (**C**) areas.*

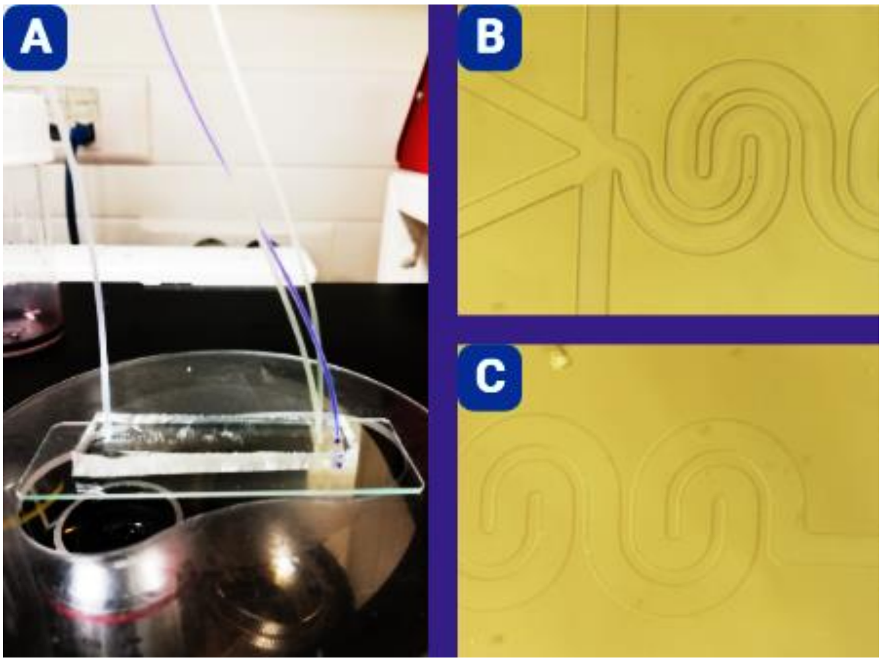

Figure 5.2 – *Food Dye assay using blue and yellow dyes in the "Serpentine 1" micromixer. The colour blue is overlapping yellow instead of giving the colour green. Macroscopic (**A**) and microscopic view in the inlet (**B**) and outlet (**C**) areas.*

5.3 – Micromixers mixing efficiency

Micromixers were tested using their passive physical elements to mix two different solutions with the help of syringe pumps to achieve a homogenized solution coming from the outlet of the device. At the molecular scale, the mixed solution should also have a conjugation of particles from each solution.

5.3.1 – Serpentine 1

The first design evaluated was the Serpentine version 1 (see **Figure 4.2**). When performing AMI analysis, images were collected along the device roughly every 1 mm, which corresponds approximately to 5000 pixels (Px) in the image scan, resulting in a total of 6 mm of mixing length. The AMI results (**Figure 5.3**) show a pattern of an almost homogenized mixing with 80 and 100 µL/min, after 5000 Px, with index values around 0.2 (complete mixing is achieved at 0). As for 60 µL/min, mixing is less ideal, with index values closer to 0.4 indicating does not grant a not well-mixed solution.

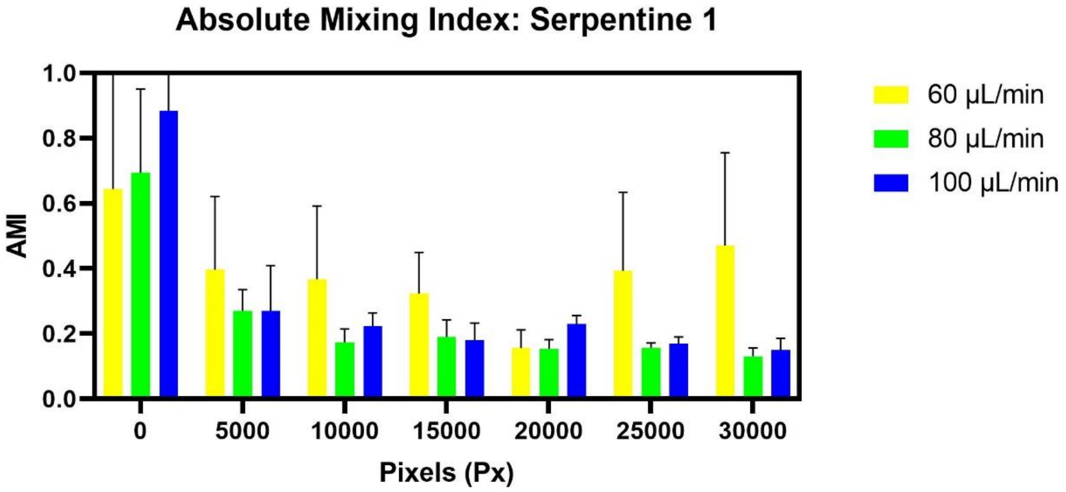

Figure 5.3 – Absolute mixing index of the serpentine 1 micromixer from 0 to 30000 pixels, using 60, 80, and 100 µL/min flow rates. Three replicates (n=3) experiments were done. The graph indicates the median and standard deviation values

In terms of RMI analysis (**Figure 5.4**), however, results show an increasing mixing efficiency throughout the device in every flow rate used. The large overlap in means and standard deviations between the different flow rates tested does not permit the determination of an ideal value. Still, all flow rates reach high index values (up to 70/80 %) by the end of the serpentine channel, mainly 100 µL/min granting the highest RMI value. With this design, flow rates superior to 100 µL/min led to leakages during pumping, therefore, the analysis becomes undetermined with faster flow rates.

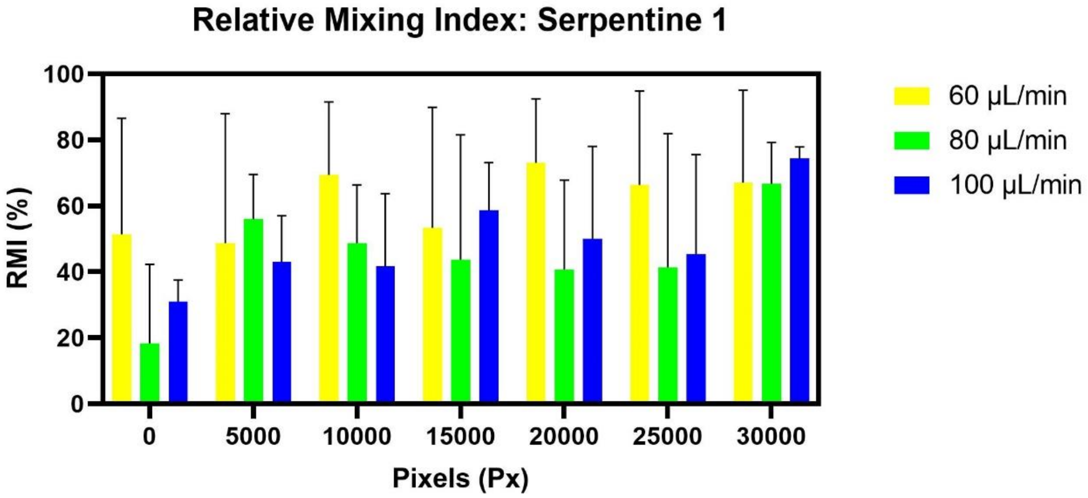

Figure 5.4 – Relative mixing index of the serpentine 1 micromixer from 0 to 30000 pixels, using 60, 80, and 100 µL/min flow rates. Three replicates (n=3) experiments were done. The graph indicates the median and standard deviation values.

5.3.2 – Serpentine 2

In this micromixer (see **Figure 4.2**), the AMI analysis (**Figure 5.5**) indicates that the mixed solution tends to show the same absolute mixing at the end of the system regardless of the flow rate. The RMI analysis (**Figure 5.6**) shows that faster flow rates tend to cause better mixing efficiency in the early stages of the mixing but flow rates with lower values end up inducing better mixing efficiency at the end of the microsystem.

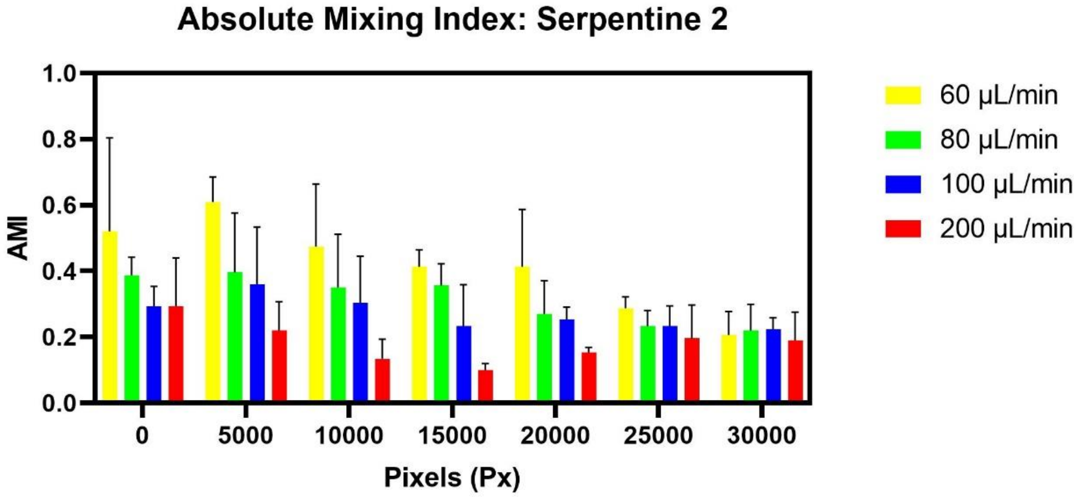

***Figure 5.5** – Absolute mixing index of the serpentine 2 micromixer from 0 to 30000 pixels, using 60, 80,100, and 200 µL/min flow rates. Three replicates (n=3) experiments were done. The graph indicates the median and standard deviation values.*

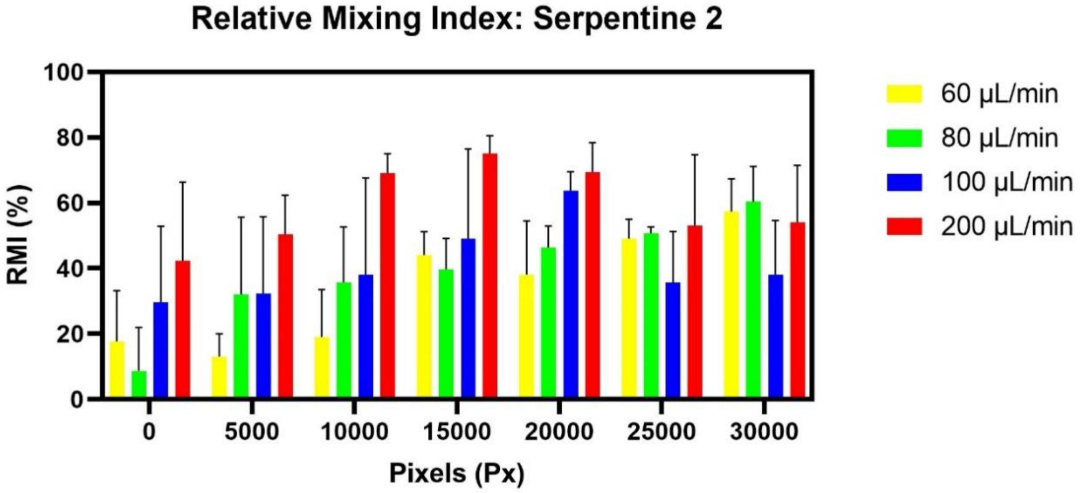

Figure 5.6 – Relative mixing index of the serpentine 2 micromixer from 0 to 30000 pixels, using 60, 80, 100, and 200 µL/min flow rates. Three replicates (n=3) experiments were done. The graph indicates the median and standard deviation values.

5.3.3 – Staggered Herringbone

The SHM design (see **Figure 4.2**) demonstrates solid AMI results (**Figure 5.7**) regardless of the flow rate used for pumping the system, granting better-homogenized samples (AMI values around 0.1) compared to the serpentine mixers. Moreover, RMI analysis (**Figure 5.8**) also shows an increasing trend in mixing efficiency, with all flow rates tested being that the mixing tends to be around 80% effective by the end of the micromixer.

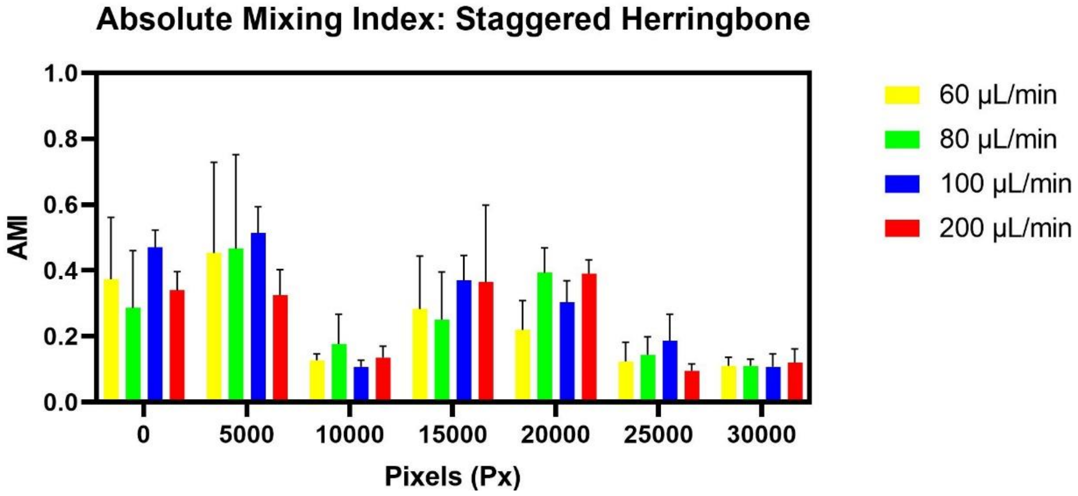

Figure 5.7 – *Absolute mixing index of the Staggered Herringbone micromixer from 0 to 30000 pixels, using 60, 80,100, and 200 µL/min flow rates. Three replicates (n=3) experiments were done. The graph indicates the median and standard deviation values.*

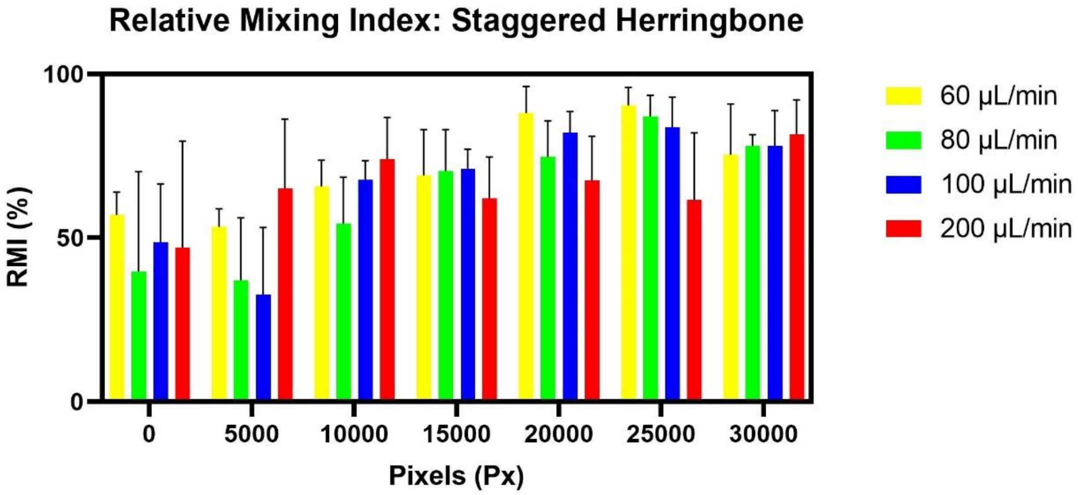

Figure 5.8 – Relative mixing index of the Staggered Herringbone micromixer from 0 to 30000 pixels, using 60, 80, 100, and 200 µL/min flow rates. Three replicates (n=3) experiments were done. The graph indicates the median and standard deviation values.

5.3.4 – “F” shape

Finally, the most complex micromixer, F-shape, with a total of 10 µm of mixing length (see **Figure 4.2**) also showed promising results with AMI analysis (**Figure 5.9**). Due to its three-dimensional chaotic microchannels, index values around 0.2 are obtained immediately at 10000 Px, for all the flow rates tested, with index values closer to 0.1 being achieved by the end of the channel. However, according to the RMI analysis (**Figure 5.10**), there is more variability in mixing efficiency along the microchannel and between different flow rates. Although there are major overlaps between the means and standard deviations between the different flow rates tested, RMI analysis still suggests that mixing efficiencies of up to 80% can be achieved. This is especially true if flow rates around 80 µL/min are used, while faster flow rates (100 and 200µL/min) are not as optimal.

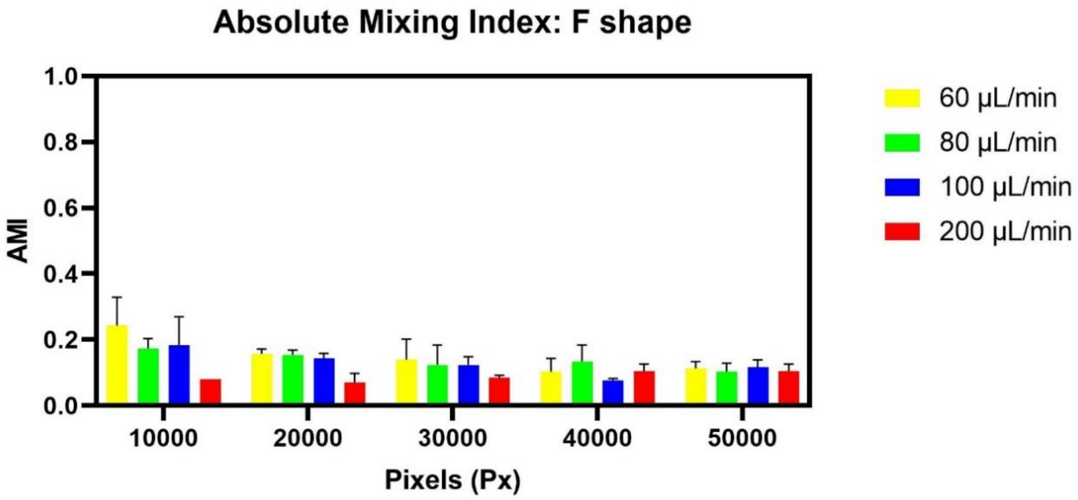

***Figure 5.9 –** Absolute mixing index of the “F” shape micromixer from 10000 to 50000 pixels, using 60, 80,100, and 200 µL/min flow rates. Three replicates (n=3) experiments were done. The graph indicates the median and standard deviation values.*

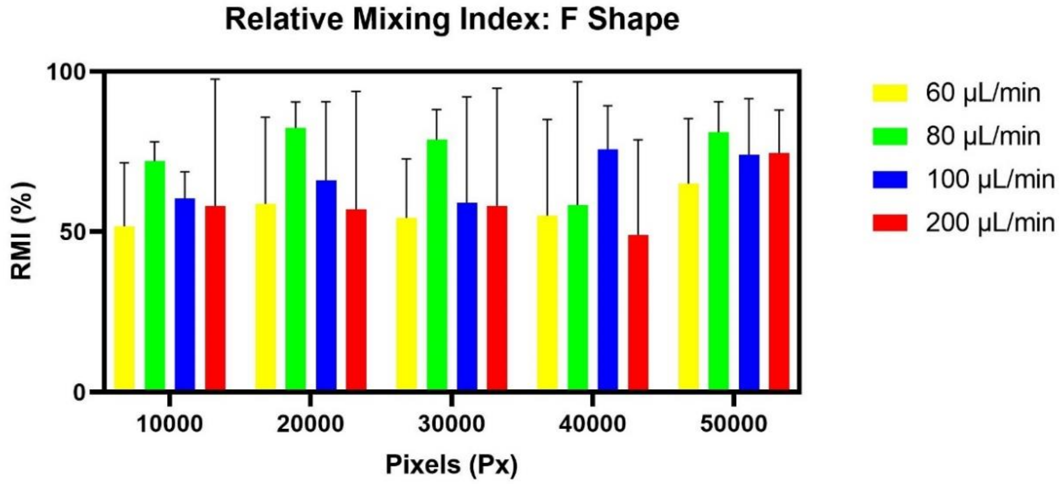

Figure 5.10 – *Relative mixing index of the "F" shape micromixer from 10000 to 50000 pixels, using 60, 80, 100, and 200 µL/min flow rates. Three replicates (n=3) experiments were done. The graph indicates the median and standard deviation values.*

5.3.5 – Comparative analysis

With the optimal flow conditions determined for each design tested, a comparison across each device type was performed. First, the mixing efficiency was compared at the end of each device by calculating the mean efficiency across all the flow rates tested. Under this metric, both SHM and "F" shape devices showed the best outcome to acquire well-mixed samples, presenting statistically significantly higher mixing efficiencies than the remainder of the devices, while the "Serpentine 2" device presents the lowest mixed sample (**Figure 5.11**). "Serpentine 1" also presents good mixing efficiency when compared with the "Serpentine 2" design (*p*-value of 0.0231), is comparable to that of the "F" shape (*p*-value of 0.2223), but is lacking when compared to the better SHM (*p*-value of 0.0057). "Serpentine 2" was the device with the lowest mean mixing efficiency when comparing the optimal SHM (*p*-value of 0.0024) and "F" shape (*p*-value of 0.0117). These two optimal designs had no significant difference between them (*p*-value of 0.2559).

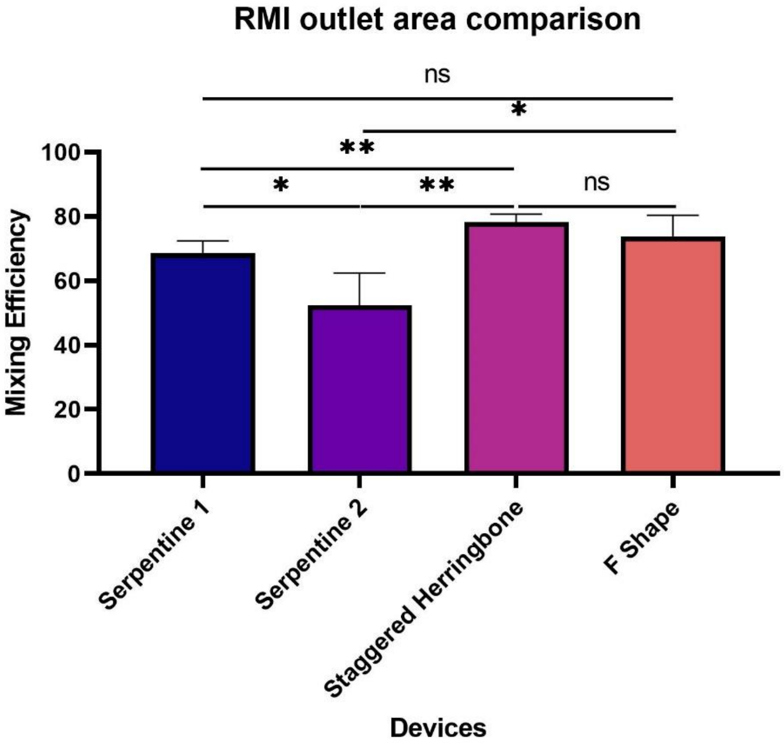

Figure 5.11 – *Comparative analysis of the RMI in each device concerning the final distances of each micromixer. Statistical significance: n.s – not significant, *p ≤ 0.05 and **p ≤ 0.01. The mean values of each flow rate tested (n=4) in the same area were inducted, alongside the standard deviation values.*

When comparing the different devices using an optimal flow rate of 100µL/min also shows that both the SHM and "F" shape designs present better mixing efficiencies, with "Serpentine 2" still presenting the lowest results (**Figure 5.12**). "Serpentine 1", while having lower mixing efficiency, is not statistically significantly different from either "Serpentine 2" (*p*-value of 0.2546) or SHM (*p*-value of 0.0845), with the latter possibly being due to the large standard deviation observed for SHM. Due to this, the "F" shape seems to provide the more reproducible, high mixing efficiency amongst all designs, having a smaller standard deviation than the SHM design, although they are not statistically different (*p*-value of 0.9240). Moreover, the "F" shape provides a higher mixing efficiency than both the "Serpentine 1" (*p*-value of 0.0292) and "Serpentine 2" (*p*-value of 0.0017) designs. While the "F" shape design presented overall the best results, the difficulties associated with its fabrication and running made it a less desirable option. Thus, the following experiments were performed in the equally high-performing SHM design or the "Serpentine 1" design.

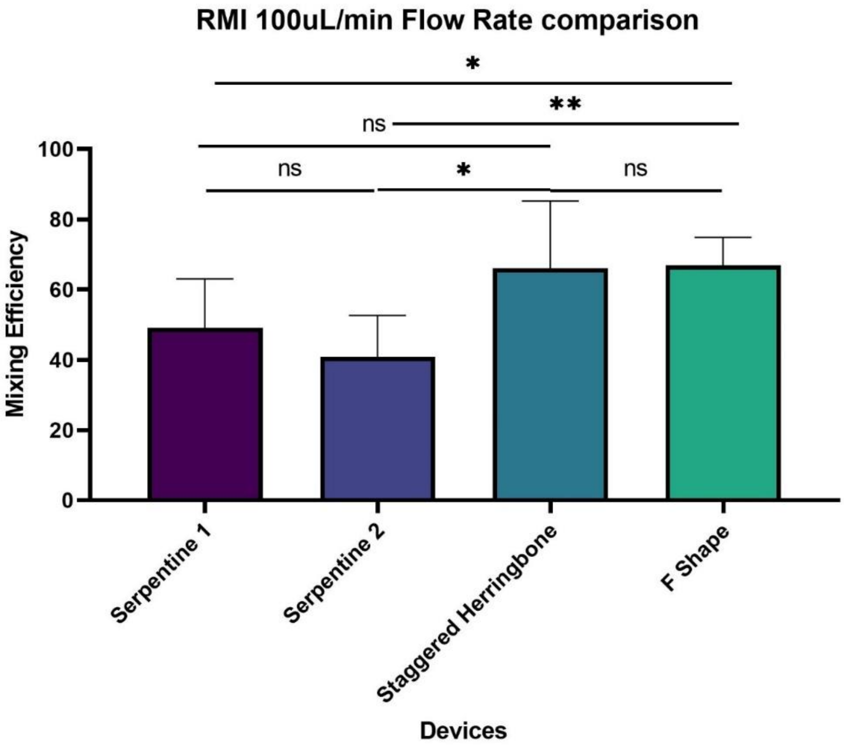

Figure 5.12 *– Comparative analysis of the RMI in each device concerning the flow rate of 100µL/min. Statistical significance: n.s – not significant, *p ≤ 0.05 and **p ≤ 0.01. Each bar represents the mean of each mean value in every point (n=4) in the microsystem analyzed, alongside standard deviations.*

5.3.6 – Fluorescent Magnetic Beads in SHM analysis

With the optimal designs defined, experiments were performed to assess whether the microscopy setup utilized could identify the presence of fluorescent magnetic beads of the same scale of EVs (100 nm in diameter). The goal was to understand how well mixing was occurring when this type of particle was present.

According to AMI and RMI results (see **Figure 5.13; 5.14**), it was observed that using flow rates of 20 and 100 µL/min mixing occurs at earlier points in the device for the lowest flow rate, which presents better AMI and RMI results than the faster one. This was probably due to hydrodynamic properties in some areas of the device that benefit the lower the flow rate gets, with lower flow rates allowing for diffusion processes to occur earlier in the channel, for example. Still, when analyzing the outlet area of the device, a flow rate of 100 µL/min appears to provide the optimal mixing efficiency. Also, to further explore the effect of flow rate, a value of 1000µL/min was used, but it was clear that the particles could not mix well within the solution. This phenomenon might be due to the short time spent by the solution in the channel, minimizing secondary hydrodynamic effects such as diffusion that contribute to optimal mixing.

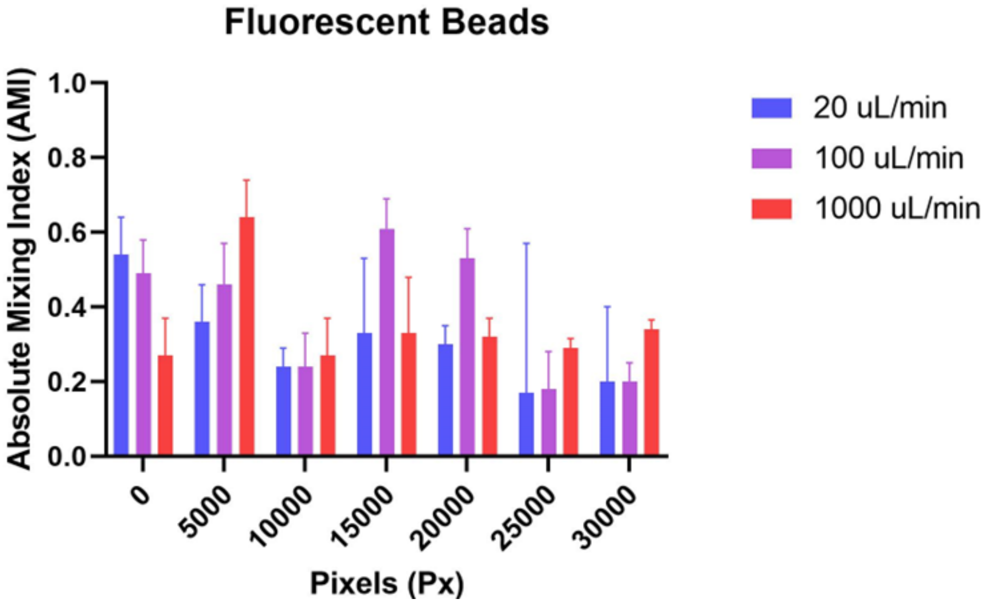

Figure 5.13 – *Absolute Mixing Index of fluorescent beads used in SHM with three different flow rates. Each bar represents the mean value of three replicates (n=3)*

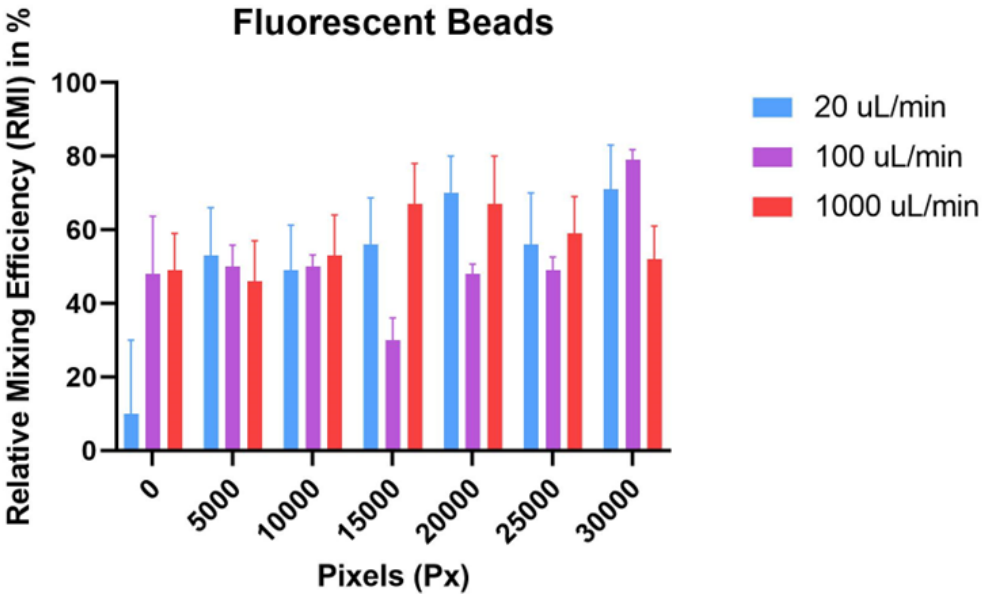

Figure 5.14 – *Relative Mixing Index of fluorescent beads used in SHM with three different flow rates. Each bar represents the mean value of three replicates (n=3).*

5.4 – ExoGAG and micromixers

GAGs are linear and negatively charged polysaccharides, due to their sulfate groups, that are bonded with positive-charged protein cores, and are found connected to cells and EV membranes. The ExoGAG reagent contains dimethylmethylene blue (DMB), which is a cationic dye that forms bonds with GAGs present in EV membranes, forming a complex of DMB-GAG-EV. Since PDMS has a strongly negative surface charge, this polymer typically forms aggregates when in contact with cationic compounds, such as DMB inside microchannels. Thus, it was hypothesized that, since a higher degree of chaotic advection results in more interactions between the PDMS substrate and the DMB-GAG-EV complex, systems such as the SHM would present a higher amount of aggregation within the microchannel despite its optimal mixing efficiency.

Indeed, it was observed that the ExoGAG reagent creates a large number of aggregations inside the microchannels - **Figure 5.15**. Even after repeated filtering of the ExoGAG sample, to remove any pre-existing aggregates, a large degree of aggregation within the device was observed. In comparison, a micromixer such as Serpentine 2, which relies on augmenting the contact surface area and the duration of contact between the two fluidic layers to achieve mixing through molecular diffusion (and not chaotic advection), presented much clearer results - **Figure 5.16**. Thus, the following results and analyses were performed using the micromixer Serpentine 2.

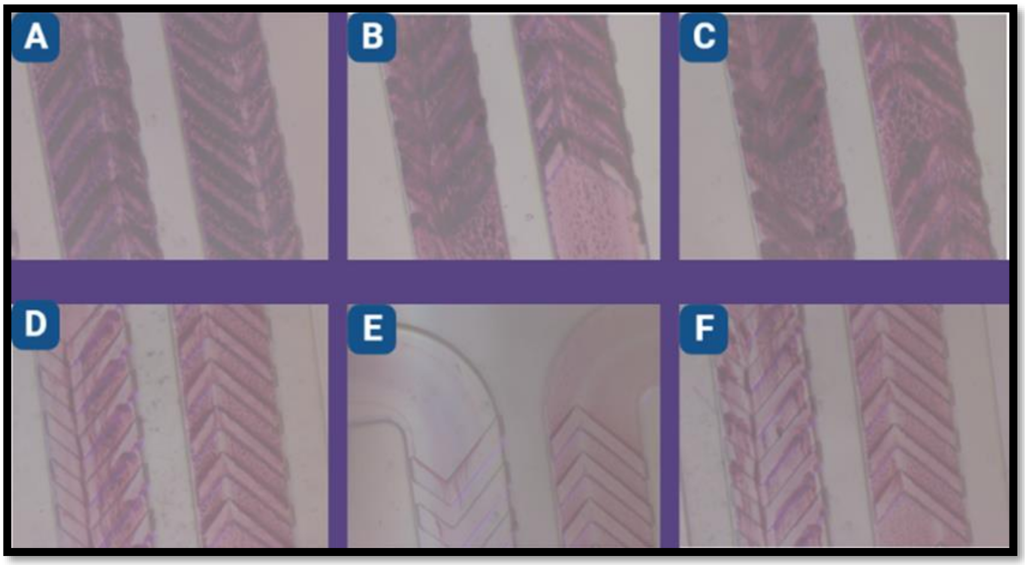

Figure 5.15 – *Mixing analysis between a solution of ExoGAG and a solution of conditioned medium. Many aggregates were formed near the herringbone grooves (****A*** *to* ***F****) due to chaotic advection present in those areas.*

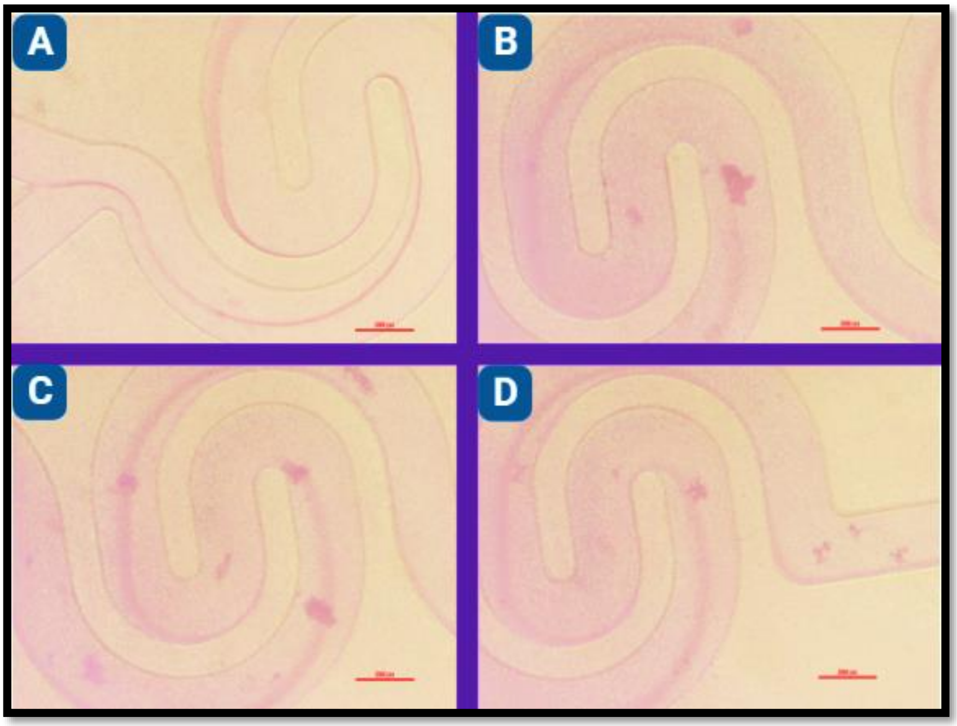

Figure 5.16 – *Mixing analysis between a solution of ExoGAG and a solution of conditioned medium. There are fewer aggregates present in the microsystem (**A** to **D**)*

5.5 – NTA Analysis

Experiments were performed to investigate whether the process of mixing a sample containing EVs with the ExoGAG reagent would provide satisfactory enrichment of EVs. This micromixing stage was performed in place of the 5 min incubation process at 4° C that is performed in the standard protocol. Replacing the incubation period with a micromixing stage would not only simplify the protocol in terms of requiring access to 4° C but would allow, in the future, for a complete microfluidic system to be developed that would then be able to sort the EV-ExoGAG complex from the sample without the need for extra centrifugation steps.

The experiments performed were thus focused on control samples of either PBS or fresh DMEM cell culture media with a known volume of spiked EVs, and on samples of conditioned medium collected from ongoing cell cultures. These samples were either processed with the standard ExoGAG protocol or run in the micromixers, as explained in **sections 4.6, 4.7, and 4.8**. The collected samples were resuspended in 1 mL of PBS, with these final samples being then analyzed with an NTA setup to characterize their EV content.

NTA allows for the size dispersion of particles in samples to be observed (**Figure 5.17**). The sample can then be characterized in terms of the particle concentration (**Figure 5.18a**) and size variation (**Figure 5.18b**). When compared with the control sample of PBS spiked with EVs and without the addition of ExoGAG, both types of samples with added ExoGAG present higher concentrations of particles. For fresh DMEM samples with spiked EVs, this is expected as, while the number of EVs should be the same in the sample, the ExoGAG reagent generates other aggregates that would still be present in the sample and within the size range detectable by the NTA. As for the conditioned medium samples, the original number of EVs in the medium was unknown, however, given that it was obtained from an ongoing cell culture at a high passage number (P = 28), it is expected to find a wide variety of material in these type of samples, including not only EVs but other particles such as apoptotic bodies, proteins, and even cell debris. Thus, the higher concentration of particles could be justified by the presence of more EVs but also other materials found in the conditioned medium.

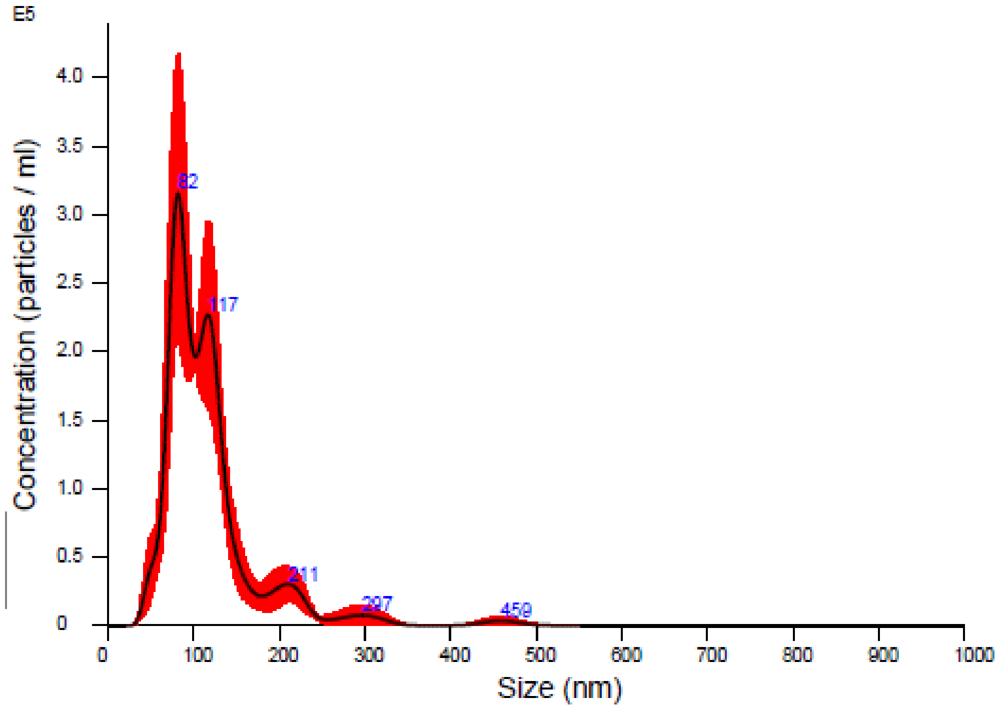

Figure 5.17 *– NTA graph that demonstrates the relation between concentration and size, showing a concentrated population of EVs conjugated with ExoGAG with approximately 100nm in size These EVs were obtained from a conditioned medium and mixed with ExoGAG within a micromixer.*

In terms of size, a rather uniform size distribution was observed for all samples, with all sample types showing EV populations with a mean size between 100 and 150 nm. In all cases, the size estimations and concentrations obtained were likely affected by the presence of a 0.2 µm filter during the pumping of the sample toward NTA. This filtration was added to protect the NTA system from eventual critical clogging, as it was unknown whether these types of ExoGAG processed samples could generate aggregates large enough to damage the system.

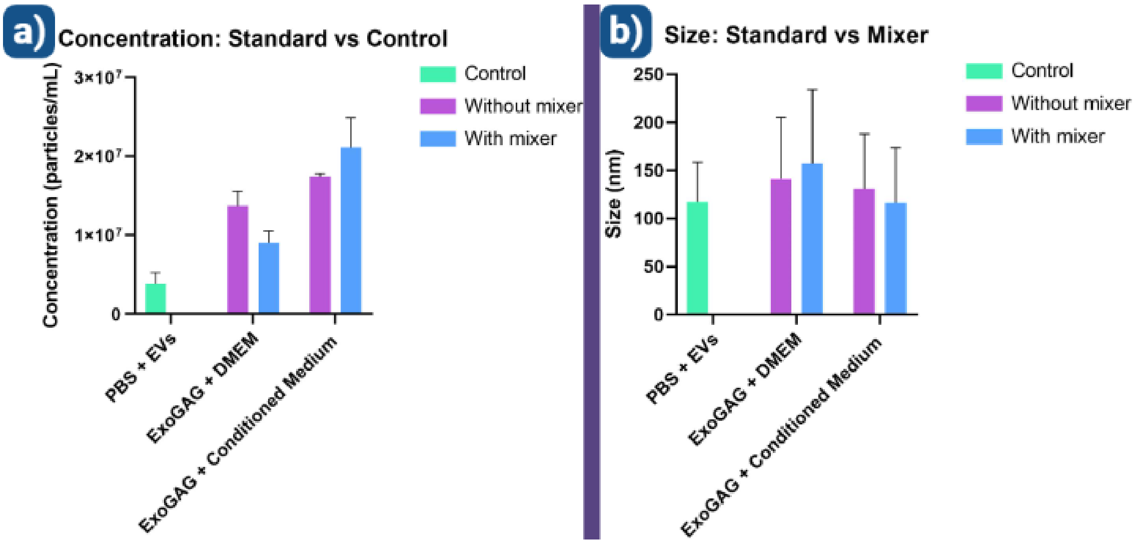

***Figure 5.18** – Comparative analysis between conditioned medium and DMEM samples that were mixed in a microsystem and samples that were just centrifuged, in terms of **a)** concentration, and **b)** size. There is no significant difference between the samples. EVs suspended in PBS is served as a control to measure the original concentration and size.*

5.6 – DLS Analysis

The same set of samples was also analyzed in parallel with DLS. This system showed similar results to NTA in terms of EV sizes, but on a logarithmic scale (see **Figure 5.19**). The samples prepared for DLS were not filtrated the same way as the previous analysis, therefore, the samples have a wider range of sizes. For example, in DMEM, it is possible to observe particles smaller than 1nm, which can be proteins or other smaller debris derived from EVs. Since our control sample shows the main population (possibly split into two sub-populations) with a mean size around 100 nm, it is possible to infer that ExoGAG conjugated with Evs are observable between 1000 and 10000nm. While in the conditioned medium the sample that went through the micromixer shows a smaller mixed population compared with the sample that was not, in DMEM shows the other way around.

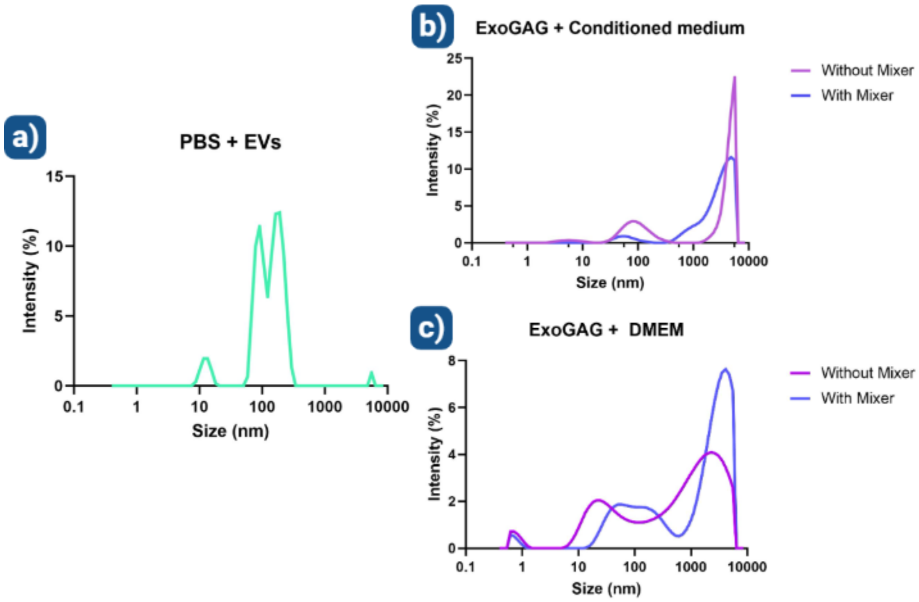

Figure 5.19 – *Comparative analysis between samples of ExoGAG mixed with conditioned medium and DMEM that were mixed in a microsystem and samples that were just centrifuged**. a)** the control sample of Evs suspended in PBS. The distribution of sizes (nm) was in terms of intensity caught by DLS where in **b)** the sample analyzed is ExoGAG with Conditioned medium and **c)** the samples analyzed is ExoGAG with DMEM. Each graph is made with a median of 3 replicate measurements in Zetasizer.*

Every mixed sample demonstrated a polydispersity (PDI) bigger than the control sample. PDI is an important statistic for determining the breadth or dispersion of particle size distribution by calculating the relation of mean size with standard deviation in each slice of the light scattered. Using a mixer reduced the PDI in the sample that has a conditioned medium but increased in the sample with DMEM (**Figure 5.20**). Zeta Potential values in mixed samples were lower than in the control sample (**Figure 5.21**). This shows that EVs mixed with ExoGAG can happen since both particles have negative electric charges on their surfaces, therefore their conjugation implies a more negative charge.

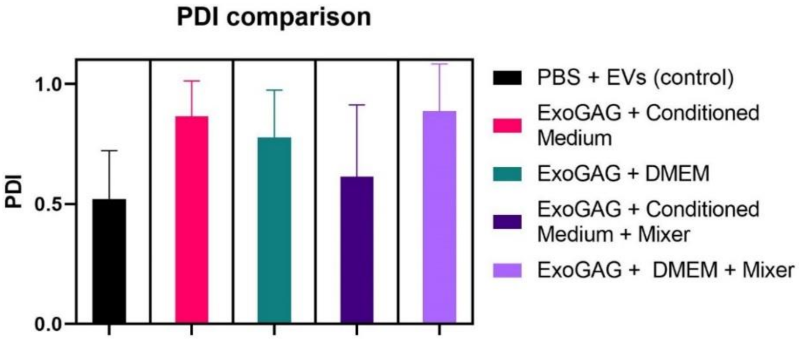

Figure 5.20 – *PDI comparison between samples. Each PDI value is based on a median of three measurements (n=3) with standard deviation as error bars*

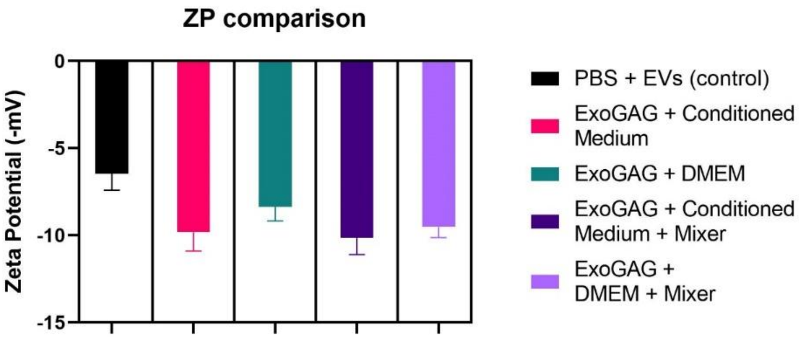

Figure 5.21 – *Zeta potential comparison between samples. Each ZP value is based on a median of three measurements (n=3) with standard deviation as error bars.*

As seen in **Figure 5.22**, different-sized populations can be found in the samples. Each individual population, or "peak", was thus compared and, just like in PDI comparison, the peak sizes of the samples (**Figure 5.20**) have the same behaviour, whereas, in samples with the conditioned medium, there are smaller sizes in the sample tested with a micromixer, while samples in DMEM are the contrary. Compared to the control, the mixing induced fewer particles smaller than 100nm. A statistical analysis performed on these samples showed that there is no significant difference between the different peak populations, indicating that, while the DLS (which is not as size-sensitive as the NTA) presents wide size distributions, the key population of EV-ExoGAG complex is present and identifiable for both samples that were processed with standard protocols or with the micromixer.

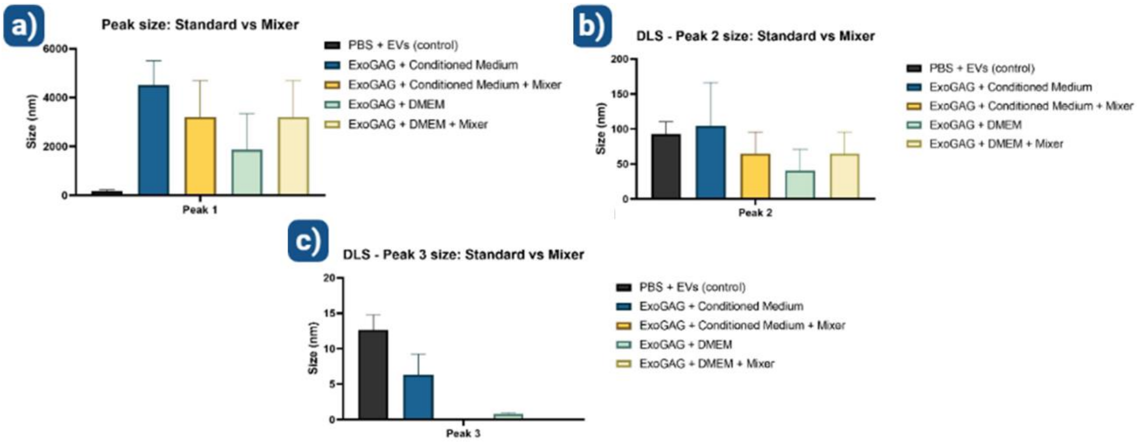

Figure 5.22 – *Peak size comparison between samples in conditioned medium, DMEM, and control sample, with and without a micromixing step. There are three peaks for each sample:* ***a)*** *The first peak is likely associated with large aggregates formed by the EV-ExoGAG with other particles or ExoGAG adhering to other biological particles found in the culture medium;* ***b)*** *The second peak is likely associated with single EV-ExoGAG complexes;* ***c)*** *the third peak shows possibly proteins and other smaller debris from EVs.*

6 – Final remarks and future perspectives

At the conclusion of this project, it was confirmed that all the microfluidic mixers were developed with proper hydrodynamic features allowing for the mixing of two different solutions. 3D microfluidic devices showed promising outcomes, however proper protocols for their development are still challenging since their fabrication hinders the easiness and fast turn-around that should characterize microfluidic devices.

Results showed that it was possible to generate populations of EVs bound to the ExoGAG reagent, although results also showed a considerable amount of polydispersity in the obtained samples, with and without using a micromixer. The motive for this might be due to two reasons. One reason is that ExoGAG, due to its natural negative electric charges, grants the reagent to have high affinity with many ions and molecules found in the samples, including the PDMS of the devices, which can lead to a significant amount of particles with different sizes in different concentrations in the mixed sample. A better way to filter and the addition of a coating substance on the PDMS layer might reduce this issue and should be evaluated in future work. The second reason is the fact that the micromixer used in the samples that were analyzed in NTA and DLS was the Serpentine 2 which showed worse AMI and RMI results, i.e., less optimal mixing when compared to other mixers. However, Serpentine 2 was used because SHM, which presented better mixing efficiency, had serious issues with aggregate deposition while running the experiments since ExoGAG reacts more with microsystems that have better hydrodynamic properties.

Finally, further investigations must be done to analyze the exterior content and markers of EVs to infer possible alterations to the micromixing protocol and obtain enhanced EV capture. With an optimized protocol, the possibility to perform tests with liquid biopsy samples from breast cancer patients should then be explored.

Bibliography

1. European cancer information system.ECIS. Breast cancer burden in EU-27 2020 new cases (incidence) and deaths (mortality) estimates new cases deaths 1 in 11. *Jt. Res. Cent.* 44–45 (2020).
2. Gomes, I. A. & Nunes, C. Analysis of the breast cancer mortality rate in Portugal over a decade: Spatiotemporal clustering analysis | Análise da Taxa de Mortalidade por Cancro da Mama em Portugal ao Longo de uma Década: Análise de Clustering Espácio-Temporal. *Acta Med. Port.* **33**, 305–310 (2020).
3. Veronesi, U., Boyle, P., Goldhirsch, A., Orecchia, R. & Viale, G. Breast cancer. *Lancet* **365**, 1727–1741 (2005).
4. Peairs, K. S., Choi, Y., Stewart, R. W. & Sateia, H. F. Screening for breast cancer. *Semin. Oncol.* **44**, 60–72 (2017).
5. Dafni, U., Tsourti, Z. & Alatsathianos, I. Breast cancer statistics in the european union: Incidence and survival across european countries. *Breast Care* **14**, 344–353 (2019).
6. Riggio, A. I., Varley, K. E. & Welm, A. L. The lingering mysteries of metastatic recurrence in breast cancer. *Br. J. Cancer* **124**, 13–26 (2021).
7. Zubair, M., Wang, S. & Ali, N. Advanced Approaches to Breast Cancer Classification and Diagnosis. *Front. Pharmacol.* **11**, 1–24 (2021).
8. Kufel-Grabowska, J. Male breast cancer. *Onkol. Pol.* **14**, 83–85 (2011).
9. Bistoni, G. & Farhadi, J. Anatomy and Physiology of the Breast. *Plast. Reconstr. Surg. Approaches Tech.* 477–485 (2015) doi:10.1002/9781118655412.ch37.
10. Mills, D. *et al.* The physiology of the normal human breast: an exploratory study. *J. Physiol. Biochem.* **67**, 621–627 (2011).
11. Jafari, S. H. *et al.* Breast cancer diagnosis: Imaging techniques and biochemical markers. *J. Cell. Physiol.* **233**, 5200–5213 (2018).
12. Rivera-Franco, M. M. & Leon-Rodriguez, E. Delays in Breast Cancer Detection and Treatment in Developing Countries. *Breast Cancer Basic Clin. Res.* **12**, 117822341775267 (2018).
13. Lameijer, J. R. C. *et al.* Trends in delayed breast cancer diagnosis after recall at screening mammography. *Eur. J. Radiol.* **136**, 109517 (2021).
14. Madia, F., Worth, A., Whelan, M. & Corvi, R. Carcinogenicity assessment: Addressing the challenges of cancer and chemicals in the environment. *Environ. Int.* **128**, 417–429 (2019).
15. Campos, J. H. *et al.* Extracellular Vesicles: Role in Inflammatory Responses and Potential Uses in Vaccination in Cancer and Infectious Diseases. *J. Immunol. Res.* **2015**, (2015).
16. Tai, Y. L. *et al.* Basics and applications of tumor-derived extracellular vesicles. *J. Biomed. Sci.* **26**, 1–17 (2019).
17. Andres, J. *et al.* Role of extracellular vesicles in cell-cell communication and

inflammation following exposure to pulmonary toxicants. *Cytokine Growth Factor Rev.* **51**, 12–18 (2020).

18. Panagopoulou, M. S., Wark, A. W., Birch, D. J. S. & Gregory, C. D. Phenotypic analysis of extracellular vesicles: a review on the applications of fluorescence. *J. Extracell. Vesicles* **9**, (2020).

19. Katsuda, T., Kosaka, N. & Ochiya, T. The roles of extracellular vesicles in cancer biology: Toward the development of novel cancer biomarkers. *Proteomics* **14**, 412–425 (2014).

20. Roberts-Dalton, H. D. *et al.* Fluorescence labelling of extracellular vesicles using a novel thiol-based strategy for quantitative analysis of cellular delivery and intracellular traffic. *Nanoscale* **9**, 13693–13706 (2017).

21. Hanayama, R. Emerging roles of extracellular vesicles in physiology and disease. *J. Biochem.* **169**, 135–138 (2021).

22. NICOLAS, R. H. & GOODWIN, G. H. Overview of Extracellular Vesicles, Their Origin, Composition, Purpose, and Methods for Exosome Isolation and Analysis. *Cells* 41–68 (2019).

23. Veziroglu, E. M. & Mias, G. I. Characterizing Extracellular Vesicles and Their Diverse RNA Contents. *Front. Genet.* **11**, 1–30 (2020).

24. Battistelli, M. & Falcieri, E. Apoptotic bodies: Particular extracellular vesicles involved in intercellular communication. *Biology (Basel).* **9**, (2020).

25. Teng, F. & Fussenegger, M. Shedding Light on Extracellular Vesicle Biogenesis and Bioengineering. **2003505**, 1–17 (2021).

26. Zhang, Y., Liu, Y., Liu, H. & Tang, W. H. Exosomes: Biogenesis, biologic function and clinical potential. *Cell Biosci.* **9**, 1–18 (2019).

27. Abels, E. R. & Breakefield, X. O. Introduction to Extracellular Vesicles: Biogenesis, RNA Cargo Selection, Content, Release, and Uptake. *Cell. Mol. Neurobiol.* **36**, 301–312 (2016).

28. Meldolesi, J. Exosomes and Ectosomes in Intercellular Communication. *Curr. Biol.* **28**, R435–R444 (2018).

29. Ståhl, A., Johansson, K., Mossberg, M., Kahn, R. & Karpman, D. Ståhl2019_Article_ExosomesAndMicrovesiclesInNorm.pdf. 11–30 (2019).

30. Green, T. M., Alpaugh, M. L., Barsky, S. H., Rappa, G. & Lorico, A. Breast cancer-derived extracellular vesicles: Characterization and contribution to the metastatic phenotype. *Biomed Res. Int.* **2015**, (2015).

31. Wang, H. X. & Gires, O. Tumor-derived extracellular vesicles in breast cancer: From bench to bedside. *Cancer Lett.* **460**, 54–64 (2019).

32. Zhou, E. *et al.* Circulating extracellular vesicles are effective biomarkers for predicting response to cancer therapy. *EBioMedicine* **67**, 103365 (2021).

33. Peng, J., Wang, W., Hua, S. & Liu, L. Roles of Extracellular Vesicles in Metastatic Breast Cancer. *Breast Cancer Basic Clin. Res.* **12**, (2018).

34. Bongiovanni, L., Andriessen, A., Wauben, M. H. M., Hoen, E. N. M. N. ’t & de Bruin, A. Extracellular Vesicles: Novel Opportunities to Understand and Detect

Neoplastic Diseases. *Vet. Pathol.* **58**, 453–471 (2021).

35. Sidhom, K., Obi, P. O. & Saleem, A. A review of exosomal isolation methods: Is size exclusion chromatography the best option? *Int. J. Mol. Sci.* **21**, 1–19 (2020).

36. Gupta, S. *et al.* An improvised one-step sucrose cushion ultracentrifugation method for exosome isolation from culture supernatants of mesenchymal stem cells. *Stem Cell Res. Ther.* **9**, 1–11 (2018).

37. Rider, M. A., Hurwitz, S. N. & Meckes, D. G. ExtraPEG: A polyethylene glycol-based method for enrichment of extracellular vesicles. *Sci. Rep.* **6**, 1–14 (2016).

38. Karttunen, J. *et al.* Precipitation-based extracellular vesicle isolation from rat plasma co-precipitate vesicle-free microRNAs. *J. Extracell. Vesicles* **8**, (2019).

39. Jara-Acevedo, R., Campos-Silva, C., Del Yáñez-Mó María, M. & Vales-Gómez, M. Exosome detection and characterization based on flow cytometry. 1–8.

40. Bachurski, D. *et al.* Extracellular vesicle measurements with nanoparticle tracking analysis–An accuracy and repeatability comparison between NanoSight NS300 and ZetaView. *J. Extracell. Vesicles* **8**, (2019).

41. Carnino, J. M., Lee, H. & Jin, Y. Isolation and characterization of extracellular vesicles from Broncho-Alveolar lavage fluid: A review and comparison of different methods. *Respir. Res.* **20**, 1–11 (2019).

42. Rikkert, L. G. *et al.* Cancer-id: Toward identification of cancer by tumor-derived extracellular vesicles in blood. *Front. Oncol.* **10**, 1–19 (2020).

43. Talebjedi, B., Tasnim, N., Hoorfar, M., Mastromonaco, G. F. & De Almeida Monteiro Melo Ferraz, M. Exploiting Microfluidics for Extracellular Vesicle Isolation and Characterization: Potential Use for Standardized Embryo Quality Assessment. *Front. Vet. Sci.* **7**, 1–18 (2021).

44. Kang, H., Kim, J. & Park, J. Methods to isolate extracellular vesicles for diagnosis. *Micro Nano Syst. Lett.* (2017) doi:10.1186/s40486-017-0049-7.

45. Reátegui, E. *et al.* Engineered nanointerfaces for microfluidic isolation and molecular profiling of tumor-specific extracellular vesicles. *Nat. Commun.* **9**, (2018).

46. Theel, E. K. & Schwaminger, S. P. Microfluidic Approaches for Affinity-Based Exosome Separation. *Int. J. Mol. Sci.* **23**, (2022).

47. Rodrigues, R. O., Pinho, D., Faustino, V. & Lima, R. A simple microfluidic device for the deformability assessment of blood cells in a continuous flow. *Biomed. Microdevices* **17**, 1–9 (2015).

48. Publication, A. Ini (19). (2022).

49. Herrero, C. *et al.* Extracellular Vesicles-Based Biomarkers Represent a Promising Liquid Biopsy in Endometrial Cancer. (2019).

50. Herrero, C., Abal, M. & Muinelo-romay, L. Circulating Extracellular Vesicles in Gynecological Tumors : Realities and Challenges. **10**, 1–10 (2020).

51. Lone, S. N. *et al.* Liquid biopsy: a step closer to transform diagnosis, prognosis and future of cancer treatments. *Mol. Cancer* **21**, 1–22 (2022).

52. Keup, C. *et al.* Integrative statistical analyses of multiple liquid biopsy analytes in metastatic breast cancer. *Genome Med.* **13**, 1–14 (2021).

53. Wang, T., Wang, Z., Niu, R. & Wang, L. Crucial role of Anxa2 in cancer progression: highlights on its novel regulatory mechanism. *Cancer Biol. Med.* **16**, 671–687 (2019).

54. Ghanam, J., Chetty, V. K., Barthel, L., Reinhardt, D. & Hoyer, P. F. DNA in extracellular vesicles : from evolution to its current application in health and disease. *Cell Biosci.* 1–13 (2022) doi:10.1186/s13578-022-00771-0.

55. Massaro, C. *et al.* Extracellular Vesicle-Based Nucleic Acid Delivery : Current Advances and Future Perspectives in Cancer Therapeutic Strategies.

56. Niculescu, A. G., Chircov, C., Bîrcă, A. C. & Grumezescu, A. M. Fabrication and applications of microfluidic devices: A review. *Int. J. Mol. Sci.* **22**, 1–26 (2021).

57. Tiwari, S. K., Bhat, S. & Mahato, K. K. Design and Fabrication of Low-cost Microfluidic Channel for Biomedical Application. *Sci. Rep.* **10**, 1–14 (2020).

58. Sancho-Albero, M. *et al.* Isolation of exosomes from whole blood by a new microfluidic device: proof of concept application in the diagnosis and monitoring of pancreatic cancer. *J. Nanobiotechnology* **18**, 1–15 (2020).

59. Guo, S. C., Tao, S. C. & Dawn, H. Microfluidics-based on-a-chip systems for isolating and analysing extracellular vesicles. *J. Extracell. Vesicles* **7**, (2018).

60. Scott, S. M. & Ali, Z. Fabrication methods for microfluidic devices: An overview. *Micromachines* **12**, (2021).

61. Wang, J., Ma, P., Kim, D. H., Liu, B. F. & Demirci, U. Towards microfluidic-based exosome isolation and detection for tumor therapy. *Nano Today* **37**, 101066 (2021).

62. Xiong, L., Chen, P. & Zhou, Q. Adhesion promotion between PDMS and glass by oxygen plasma pre-treatment. *J. Adhes. Sci. Technol.* **28**, 1046–1054 (2014).

63. Gale, B. K. *et al.* A review of current methods in microfluidic device fabrication and future commercialization prospects. *Inventions* **3**, (2018).

64. Costa, F., Falzetti, L., Baldini, N. & Avnet, S. The microfluidic trainer: Design, fabrication and validation of a tool for testing and improving manual skills. *Micromachines* **11**, (2020).

65. Osman, R. A., Esa, S. R. & Poopalan, P. Design and fabrication of microfluidic devices: Mosfet & capacitor. *Proc. IEEE/CPMT Int. Electron. Manuf. Technol. Symp.* 321–327 (2006) doi:10.1109/IEMT.2006.4456474.

66. CADFolks. *AutoCAD 2021 Beginners Guide*. (2021).

67. Lake, M. *et al.* Microfluidic device design, fabrication, and testing protocols. *Protoc. Exch.* 1–26 (2015) doi:10.1038/protex.2015.069.

68. Foundry, S. M. Designing Your Own Device: Basic Design Rules. *Foundry, Stanford Microfluid.* 2–3 (2004).

69. Skliutas, E. *et al. Polymerization mechanisms initiated by spatio-temporally confined light*. *Nanophotonics* vol. 10 (2021).

70. Ayoib, A. *et al.* Low cost design and fabrication of PDMS microfluidics micromixers for DNA extraction. *Proc. 2017 IEEE Reg. Symp. Micro Nanoelectron. RSM 2017* 227–230 (2017) doi:10.1109/RSM.2017.8069158.

71. Raj M, K. & Chakraborty, S. PDMS microfluidics: A mini review. *J. Appl. Polym. Sci.* **137**, 1–14 (2020).

72. Kim, H. S., Son, B. H., Kim, Y. C. & Ahn, Y. H. Direct laser writing lithography using a negative-tone electron-beam resist. *Opt. Mater. Express* **10**, 2813 (2020).

73. Wang, R., Wei, J. & Fan, Y. Chalcogenide phase-change thin films used as grayscale photolithography materials. *Opt. Express* **22**, 4973 (2014).

74. Handrea-Dragan, M. & Botiz, I. Multifunctional structured platforms: From patterning of polymer-based films to their subsequent filling with various nanomaterials. *Polymers (Basel).* **13**, 1–49 (2021).

75. Gilles, S. Chemical Modification of Silicon Surfaces for the Application in Soft Lithography. *Berichte-Forschungszentrum Julich* 1–91 (2007).

76. Delon, L. C. *et al.* Hele Shaw microfluidic device: A new tool for systematic investigation into the effect of the fluid shear stress for organs-on-chips. *MethodsX* **7**, 100980 (2020).

77. Cabral, P. D. *et al.* Clean-room lithographical processes for the fabrication of graphene biosensors. *Materials (Basel).* **13**, 1–23 (2020).

78. Thermo Fisher Scientific. Safety Data Sheet . ةم سلا تانايب ةرشن Safety Data Sheet. *Mater. Saf. Data Sheet* **4(2)**, 8–10 (2012).

79. Islam, M. U. Difference between Silicon Wafer <100> & <111> (Feb 05, 2010). *Whitepaper* 1–5 (2010).

80. Pk, P. K. Crystallography Overview for MEMS. 1–23.

81. Pal, P., Sato, K. & Chandra, S. Fabrication techniques of convex corners in a (100)-silicon wafer using bulk micromachining: A review. *J. Micromechanics Microengineering* **17**, (2007).

82. Choung, R. S. *et al.* Determination of B-cell epitopes in patients with celiac disease: Peptide microarrays. *PLoS One* **11**, (2016).

83. Carvalho, J. *et al.* Single-use microfluidic device for purification and concentration of environmental DNA from river water. *Talanta* **226**, (2021).

84. Agudelo, D., Kreplak, L. & Tajmir-Riahi, H. A. Microscopic and spectroscopic analysis of chitosan-DNA conjugates. *Carbohydr. Polym.* **137**, 207–213 (2016).

85. Lake, J. R., Heyde, K. C. & Ruder, W. C. Low-cost feedback-controlled syringe pressure pumps for microfluidics applications. *PLoS One* **12**, 1–12 (2017).

86. Cao, W., Easley, C. J., Ferrance, J. P. & Landers, J. P. Chitosan as a polymer for pH-induced DNA capture in a totally aqueous system. *Anal. Chem.* **78**, 7222–7228 (2006).

87. Aissaoui, N., Bergaoui, L., Landoulsi, J. & Vi, P. Silane Layers on Silicon Surfaces : Mechanism of Interaction , Stability , and Influence on Protein Adsorption. 656–665 (2012).

88. Tu, J. *et al.* PDMS-based microfluidic devices using commoditized PCBs as masters with no specialized equipment required. *RSC Adv.* **7**, 31603–31609 (2017).

89. Lima, R. A. & Catarino, S. *Micro/Nano Devices for Blood Analysis*. *Micro/Nano Devices for Blood Analysis* (2020). doi:10.3390/books978-3-03921-825-7.

90. Raza, W., Hossain, S. & Kim, K. Y. A review of passive micromixers with a comparative analysis. *Micromachines* **11**, (2020).

91. Cai, G., Xue, L., Zhang, H. & Lin, J. A review on micromixers. *Micromachines* **8**, (2017).

92. Yuan, S., Jiang, B., Peng, T., Li, Q. & Zhou, M. An investigation of flow patterns and mixing characteristics in a cross-shaped micromixer within the laminar regime. *Micromachines* **12**, 1–20 (2021).

93. Liao, Y., Mechulam, Y. & Lassalle-Kaiser, B. A millisecond passive micromixer with low flow rate, low sample consumption and easy fabrication. *Sci. Rep.* **11**, 1–14 (2021).

94. Shanko, E. S., van de Burgt, Y., Anderson, P. D. & den Toonder, J. M. J. Microfluidic magnetic mixing at low reynolds numbers and in stagnant fluids. *Micromachines* **10**, (2019).

95. López, R. R. *et al.* Numerical and experimental validation of mixing efficiency in periodic disturbance mixers. *Micromachines* **12**, 1–13 (2021).

96. Parvez, M. S. Design of Microfluidic Injection System using Bernoulli ' s Principle. 0–1 (2019) doi:10.13140/RG.2.2.21030.96320.

97. Prabhakar, P. *et al.* 3D-Printed Microfluidics and Potential Biomedical Applications. *Front. Nanotechnol.* **3**, 1–16 (2021).

98. Yuan, S., Jiang, B., Peng, T., Zhou, M. & Drummer, D. Investigation of efficient mixing enhancement in planar micromixers with short mixing length. *Chem. Eng. Process. - Process Intensif.* **171**, 108747 (2022).

99. Sivashankar, S. *et al.* A 'twisted' microfluidic mixer suitable for a wide range of flow rate applications. *Biomicrofluidics* **10**, 1–13 (2016).

100. Hejazian, M., Balaur, E. & Abbey, B. Sub-millisecond integrated mix-and-inject microfluidic sample delivery devices. (2021) doi:10.20944/preprints202102.0199.v1.

101. Tsai, C. H. D. & Lin, X. Y. Experimental study on microfluidic mixing with different zigzag angles. *Micromachines* **10**, (2019).

102. Shen, F., Ai, M., Ma, J., Li, Z. & Xue, S. An easy method for pressure measurement in microchannels using trapped air compression in a one-end-sealed capillary. *Micromachines* **11**, (2020).

103. Al-Halhouli, A. *et al.* Passive micromixers with interlocking semi-circle and omega-shaped modules: Experiments and simulations. *Micromachines* **6**, 953–968 (2015).

104. Zhang, X., Xia, K. & Ji, A. A portable plug-and-play syringe pump using passive valves for microfluidic applications. *Sensors Actuators, B Chem.* **304**, 127331 (2020).

105. MiloŽič, N., Lubej, M., Novak, U., Žnidaršič-Plazl, P. & Plazl, I. Evaluation of diffusion coefficient determination using a microfluidic device. *Chem. Biochem. Eng. Q.* **28**, 215–223 (2014).

106. Lecture, P. Lecture 3 : advection – diffusion , mixing in micro - channels. (2017).

107. Gambhire, S., Patel, N., Gambhire, G. & Kale, S. A Review on Different Micromixers and its Micromixing within Microchannel. *Int. J. Curr. Eng. Technol.* (2011) doi:10.14741/ijcet/22774106/spl.4.2016.83.

108. Shi, H., Zhao, Y. & Liu, Z. Numerical investigation of the secondary flow effect of lateral structure of micromixing channel on laminar flow. *Sensors Actuators, B Chem.* **321**, (2020).

109. Microfluidic Mixing. *SpringerReference* 1–13 (2011) doi:10.1007/springerreference_67173.

110. Kim, D. S., Lee, S. H., Kwon, T. H. & Ahn, C. H. A serpentine laminating micromixer combining splitting/recombination and advection. *Lab Chip* **5**, 739–747 (2005).

111. Wang, S., Huang, X. & Yang, C. Mixing enhancement for high viscous fluids in a microfluidic chamber. *Lab Chip* **11**, 2081–2087 (2011).

112. Chadly, D. M. *et al.* Full Factorial Microfluidic Designs and Devices for Parallelizing Human Pluripotent Stem Cell Differentiation. *SLAS Technol.* **24**, 41–54 (2019).

113. Shanko, E. S. *et al.* Magnetic bead mixing in a microfluidic chamber induced by an in-plane rotating magnetic field. *Microfluid. Nanofluidics* **26**, 1–12 (2022).

114. Abràmoff, M. D., Magalhães, P. J. & Ram, S. J. Image processing with imageJ. *Biophotonics Int.* **11**, 36–41 (2004).

115. Johnson, H. J., McCormick, M. M., Ibanez, L., Consortium, I. S. & others. The ITK software guide: design and functionality. 410–983 (2015).

116. Hashmi, A. & Xu, J. On the Quantification of Mixing in Microfluidics. *J. Lab. Autom.* **19**, 488–491 (2014).

117. Karthikeyan, K. & Sujatha, L. Study of permissible flow rate and mixing efficiency of the micromixer devices. *Int. J. Chem. React. Eng.* **17**, (2019).

118. Johnson, T. J., Ross, D. & Locascio, L. E. Rapid microfluidic mixing. *Anal. Chem.* **74**, 45–51 (2002).

119. Xia, H. M. *et al.* Aeroelasticity-based fluid agitation for lab-on-chips. *Lab Chip* **13**, 1619–1625 (2013).

120. Lin, Y. C., Chung, Y. C. & Wu, C. Y. Mixing enhancement of the passive microfluidic mixer with J-shaped baffles in the tee channel. *Biomed. Microdevices* **9**, 215–221 (2007).

5 – Suplementary data

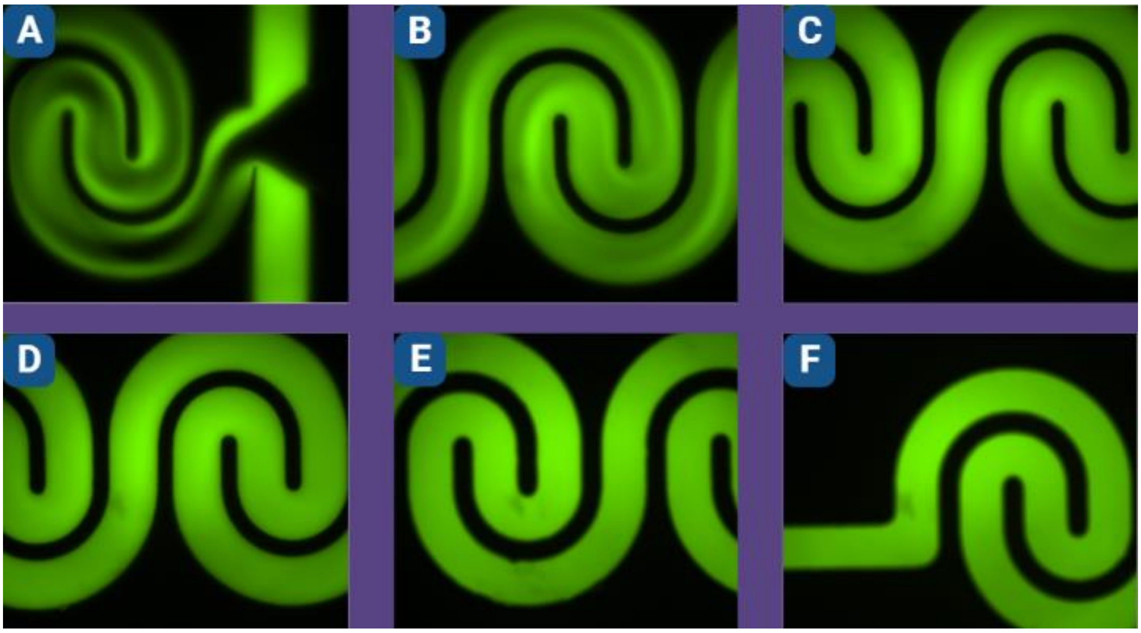

Figure S.1 – *Fluorescence assay in Serpentine 1 micromixer at 100 µL/min. A – Inlet area. B to E – Mixing area. F – Outlet area*

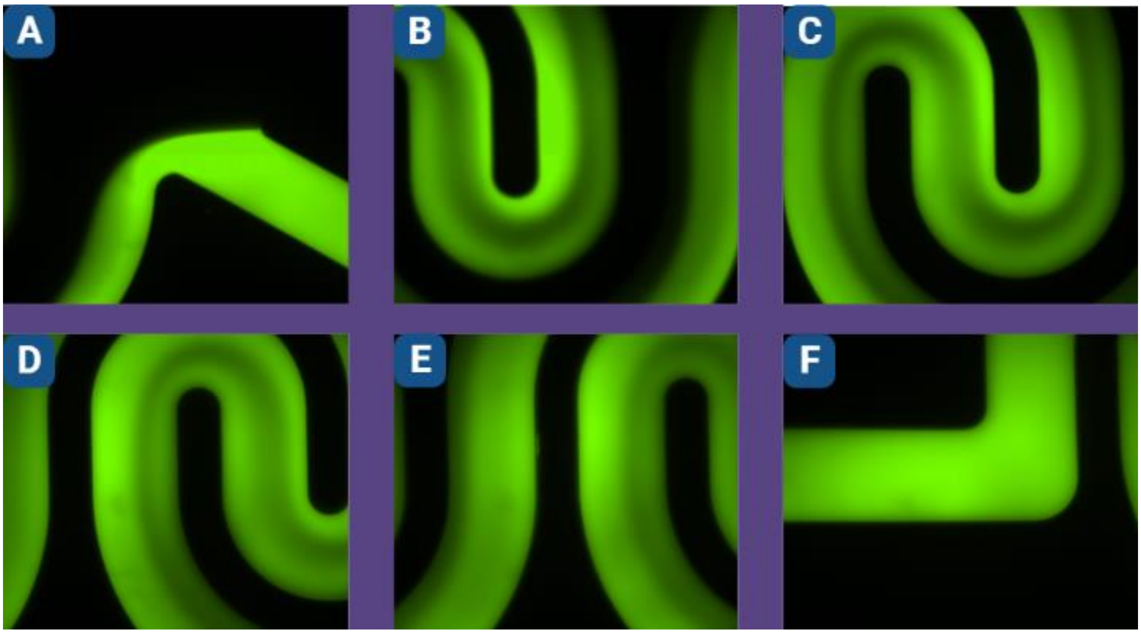

Figure S.2 – *Fluorescence assay in Serpentine 2 micromixer at 100 µL/min. A – Inlet area. B to E – Mixing area. F – Outlet area*

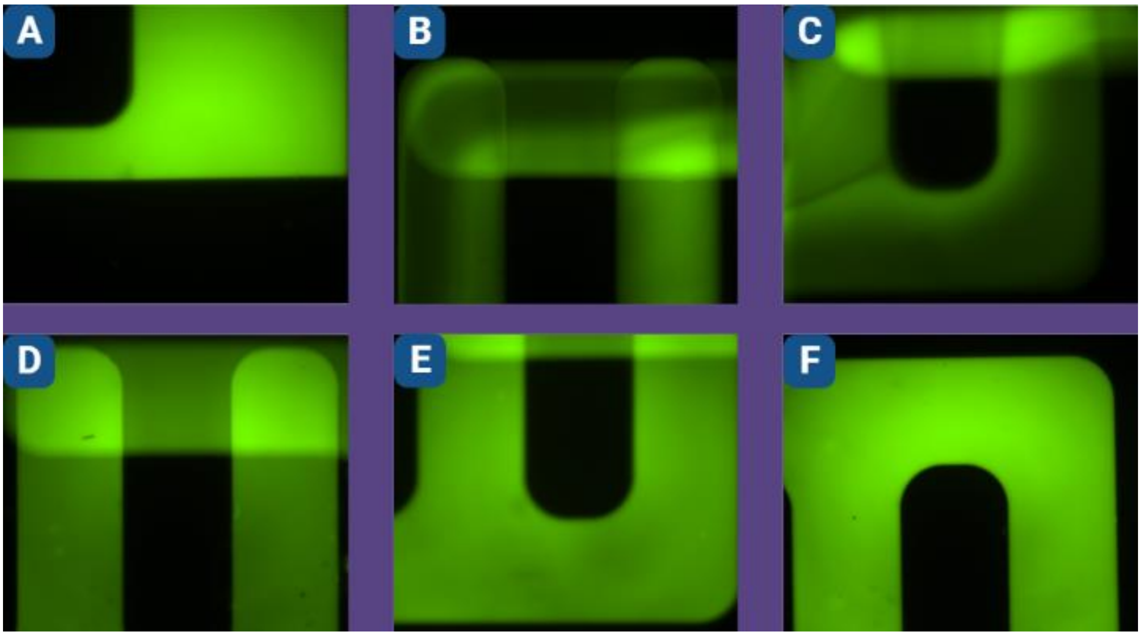

Figure S.3 – *Fluorescence assay in "F" shape micromixer at 100 µL/min. A – Inlet area. B to E – Mixing area. F – Outlet area.*

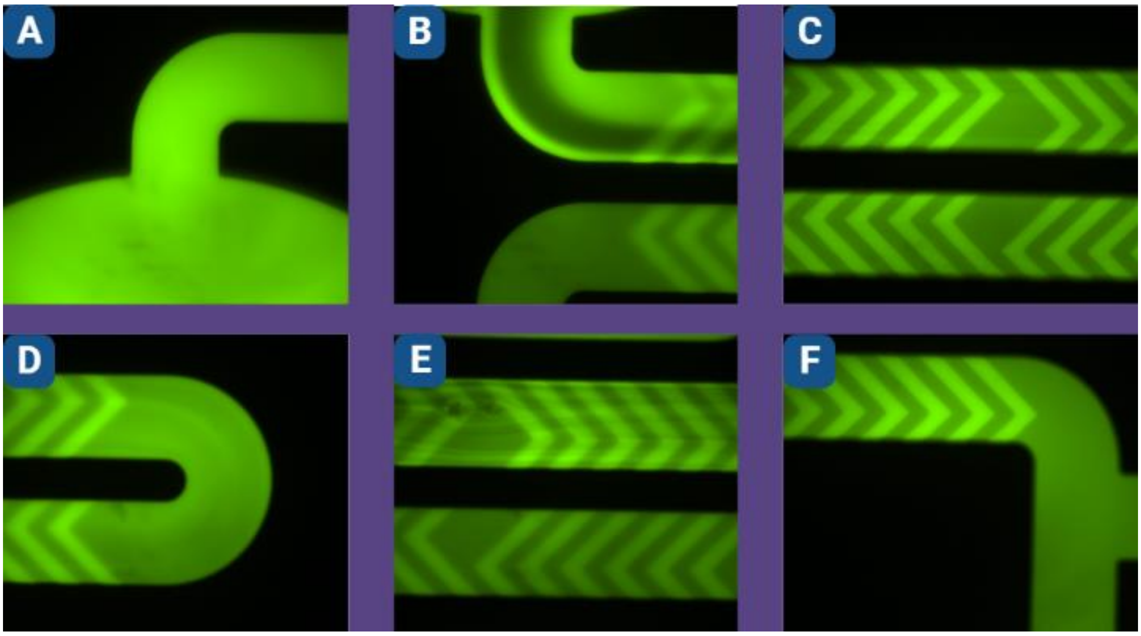

Figure S.4 – *Fluorescence assay in Staggered herringbone micromixer at 100 µL/min. A – Inlet area. B to E – Mixing area. F – Outlet area*

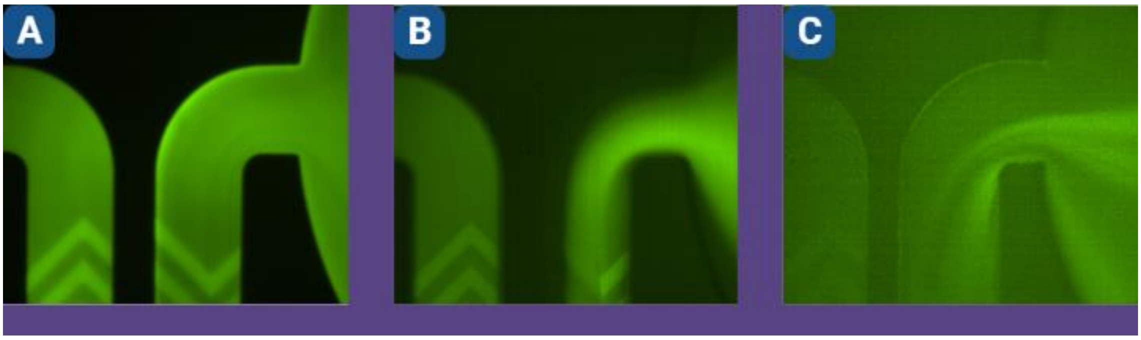

Figure S.5 *– Magnetic fluorescent beads assay using the SHM. three different flow rates were (20, 100, and 1000) to test if the intensity of these particles is observable*

Figure S.6 *– Pumping mechanism setup. The syringe pump is adjusted manually to program de flow rate, the amount of volume pumped, and the diameter of the syringes inserted. Tubing and connectors are used to connect the syringes to the device that is on top of the microscope. A computer with the appropriate software gives us a real-time illustration of what is occurring during the pumping.*